UNIVERSITÀ
DEGLI STUDI
DI PADOVA

Sede Amministrativa: Università degli Studi di Padova
Facolta' di SCIENZE MM.FF.NN

Dipartimento di GEOSCIENZE

SCUOLA DI DOTTORATO DI RICERCA IN: SCIENZE DELLA TERRA
CICLO XXII

An experimental study on saturated granular flows and its application to the physical modelling of debris flows

Direttore della Scuola : Ch.mo Prof. Gilberto Artioli
Supervisore : Ch.mo Prof. Rinaldo Genevois
Cotutore : Dr. Elisabeth T. Bowman

Dottoranda : Nicoletta Sanvitale

30 Luglio 2010

“Kids, you tried your best and failed miserably. The lesson is…never try”

HOMER SIMPSON

Summary

"Flow" in saturated granular materials may describe behaviour that ranges from gently moving sediments in coastal or alluvial situations, through post-liquefaction lateral spreading of sloping ground as triggered by earthquakes and finally, to fast moving mixtures of soil and rock, in the case of mud and debris flows. The present Ph.D. work addresses the study of flows in the context of the high-speed movement of saturated granular materials moving down slope under the influence of gravity. Such flows as occur in nature are termed "debris flows".

This study has been undertaken following two complementary research activities, both using small-scale flumes.

The first activity aimed at determining if the well-graded nature of debris flow materials is key to their tendency to travel fast and far before final deposition. A number of tests using soil with different gradations at a given moisture content, were performed in order to understand the role of particle size in the flow behaviour of granular material.

The second, had the objective of developing a novel method based on the Planar Laser Induced Fluorescence technique and refractive index matching, for the analysis of experimental saturated granular flows in a context of high speed movement and in free surface conditions. Such method allows to investigate the internal behaviour of concentrated granular flows. A number of experiments have been conducted to verify the feasibility of the developed method. The preliminary results of a first series of experiments are presented.

Sommario

I flussi di materiale granulare saturo comprendono un'ampia serie di fenomeni (da sedimenti in moto lento in zone costiere o alluvionali fino a miscele di terra e rocce in moto rapido, come colate di fango e debris flows). Il lavoro presentato in questa tesi di dottorato ha l'obiettivo di studiare i flussi di materiale detritico non-plastico saturo, che si muovono a velocità elevate sotto l'azione dell'accelerazione gravitazionale. In natura questi flussi granulari sono usualmente indicati con il termine inglese "debris flows".

Il lavoro di ricerca si è sviluppato su due principali attività sperimentali, tra loro complementari, ma entrambe basate sull'utilizzo di sperimentazione in canaletta.

La prima delle ricerche condotte ha avuto la finalità di stabilire quanto la composizione ben assortita dei sedimenti che costituiscono un debris flow possa influenzarne la propensione a muoversi ad alta velocità e per lunghe distanze. Negli esperimenti condotti sono state utilizzate miscele costituite da particelle di terreno con diverse distribuzioni granulometriche in modo da

riprodurre, su piccola scala e in condizioni controllate, alcuni dei fenomeni che caratterizzano la loro mobilità.

La seconda attività di ricerca è stata incentrata sullo sviluppo di una tecnica sperimentale innovativa per lo studio dei flussi granulari rapidi saturi che si muovono in condizioni di “superficie libera”. Lo scopo della ricerca e’ stato quello di analizzare il comportamento delle particelle solide all’interno del flusso, ovvero lontano da bordi o pareti trasparenti che potrebbero interagire con il flusso stesso perturbandone il movimento e compromettendo quindi, la dinamica osservata. La metodologia sviluppata si basa sull’applicazione di una tecnica nota come “Planar Laser Induced Fluorescence” e sulla scelta di materiali con opportune proprietà ottiche. Gli esperimenti presentati confermano l’applicabilità della tecnica proposta allo studio di questo tipo particolare di fenomeni. Nella tesi vengono anche presentati i risultati preliminari della prima serie di test realizzati.

Table of contents

Notation

A	cross-section area normal to the direction of flow [m^2]
a	empirical constant used for different applications
B	empirical constant used for different applications
C	shape factor
C_s	volume concentration of the solid in flow
C_H	Hazen empirical coefficient
$C_{K\text{-}C}$	Kozeny-Carman empirical coefficient
C_U	Coefficient of Uniformity
C_z	Coefficient of Curvature
c	cohesive strength [Pa]
D	hydraulic diffusivity [m^2/s]
D_{eff}	effective diameter [m]
E_{em}	photon energy [J]
d	grain size [m]
e	void ratio
g	gravitational acceleration [m/s^2]
h	local thickness of the fluid [m]
h_c	Planck constant [Js]
h_u	upstream debris flow depth [m]
i	hydraulic gradient
H	flow depth [m]
k	Darcy's permeability [m/s]
L	flow length [m]
N_{BAG}	Bagnold Number
N_R	Quasi-Reynolds Number
N_F	Fluidisation Number
N_P	Pore Pressure Number
N_{Rey}	Reynolds Number
N_S	Savage Number
ε	Flow Aspect Ratio

n	power law index
S_f	friction slope
S_o	specific surface area per unit volume of particles [m^2/g]
SF	shape factor
Re	Reynolds Number
s	mean free distance between particles [m]
std	standard deviation
T	surface tension [kN/m]
t_D	debris flow duration [s]
U	cross-section mean velocity [m/s]
U_e	pore water suction [Pa]
u	pore pressure [Pa]
u	mean velocity of flow at height z [m/s]
v	velocity of flow at height z [m/s]
v_f	fluid fraction
v_c	critical velocity [m/s]
v_s	solid fraction
v_{set}	grain settling velocity [m/s]
v_u	upstream debris velocity [m/s]
v_*	maximum value assumed by v_s
x_T	runout distance[m]
α	dynamic friction angle [°]
δ	characteristic grain diameter [m]
ε	Flow Aspect Ratio
$\mathcal{E}$	extinction coefficient
θ_u	entrance slope angle (channel slope) [°]
θ	runout slope angle (fan slope) [°]
φ	internal friction angle [°]
ϕ	quantum yield
$\dot{\gamma}$	shear rate [s^{-1}]
γ_w	unit weight of the water [N/m^3]
γ_P	unit weight of the permeant [N/m^3]
λ	linear grain concentration [m]
λ_e	photon wavelength [nm]

ρ_m	apparent density of fluid incorporated with suspended particles [kg/m^3]
ρ_s	solid density [kg/m^3]
ρ_T	apparent density of debris flow material [kg/m^3]
σ	total normal stress [Pa]
τ	shear stress [Pa]
τ_c	shear due to grain collisions [Pa]
τ_o	yield strength in shear [Pa]
τ_t	turbulent mixing stress of the fluid [Pa]
τ_v	viscous shear stress due to the deformation of the fluid [Pa]
μ	viscosity of the interstitial fluid [Pa·s]

Introduction

"Flow" in saturated granular materials may describe behaviour that ranges from gently moving sediments in coastal or alluvial situations, through post-liquefaction lateral spreading of sloping ground as triggered by earthquakes and finally, to fast moving mixtures of soil and rock, in the case of mud and debris flows. The present Ph.D. work addresses the study of flows in the context of the high-speed movement of saturated granular materials moving down slope under the influence of gravity. Such flows as occur in nature are termed "debris flows" (Hungr et al. 2001)

Debris flows, fast moving mixtures of rock, soil and water, are recognized as one of the most hazardous geophysical flows due to their high mobility and destructive power (Jakob & Hungr 2005).They are particularly complex mechanically and the current state of knowledge is insufficient to accurately describe their behaviour. This complexity is due to debris flow materials having a large range of clast sizes, which tend to segregate during motion, altering the material behaviour in time and in space. In addition, debris flows have a propensity to erode and deposit material, rendering their boundary conditions rather indeterminate. Understanding the dynamics of debris flows has become a critical concern due to a worldwide increase in human settlement of mountainous regions, where the hazards and risks associated with these kinds of phenomena are the greatest.

The mechanics of debris flows can be investigated using different approaches, such as physical modelling, field observation or analytical/numerical modelling. Since the initial and the boundary conditions of natural debris flows are rather indeterminate, a better understanding of the related mechanics can be attained by means of physical modelling, which allows the phenomena to be analysed in controlled experiments with well-defined boundary conditions and known parameters.

The close control over the model details, leads patterns of response to particular input perturbations to be obtained, enabling repeatability and hence, parametric studies to be conducted

This thesis addresses an experimental study of saturated granular flows with a specific attention to the implications related to the physical modelling of debris flows. Two laboratory researches were undertaken using small-scale flumes with the application of standard and novel approaches.

The first research activity aimed at determining if the well-graded nature of debris flow materials is key to their tendency to travel fast and far before final deposition. Field evidence shows that virtually all debris flows contain a wide particle size distribution (PSD), with sizes ranging from boulders or gravel to silt and clay. A number of tests using soil with different gradations, at a given moisture content, were performed in order to understand the role of particle size in the flow behaviour of granular material.

The second part of the Ph.D. research intended to develop a novel method, based on the Planar Laser Induced Fluorescence technique and refractive index matching, for the analysis of experimental saturated granular flows in a context of high speed movement and in free surface conditions. Such method allows to overcome the limitation imposed by standard approaches which permits only to examine the behaviour of the phenomena at the flow margins (usually the top and the sides). In fact, the investigation of the internal behaviour of concentrated two-phase flows is prevented by their high opacity. A number of experiments have been conducted to verify the feasibility of the developed method and the preliminary results of a first series of experiments have been analyzed using an image processing approach based on the Particle Image Velocimetry technique.

The thesis is organized ad follows.
In Chapter 1 an overview of the main characteristics and the properties of debris flow and a brief summary of the work are given.
Chapter 2 describes the methodology and the experimental setup used to perform the experiments related to the first part of the doctoral research activity. Then, the basic concepts of the dynamic model of Takahashi are introduced. Finally, the experimental procedure and the apparatus used in the test are described.
In Chapter 3, the test conditions are described and the results of the tests are presented and discussed. In particular the deposit morphology and the velocities of the flows are analyzed.
The setup of the experimental apparatus for the non-invasive optical investigation of the internal flow behaviour is presented in Chapter 4. An overview of the background concepts behind the

methodology is given, together with the description of the arrangement, of the adopted optical devices and of the physical and optical properties of the materials. Finally, the description and the tuning of the flume apparatus, materials and of the optical devices are presented.

The permeability of the mixtures used in the flume experiments is examined in Chapter 5. A short overview about permeability and indirect methods for its estimate is given. The procedure and the results of the permeability tests performed on the adopted mixtures are reported.

Chapter 6 illustrates the test conditions for the experiments using the non intrusive optical approach. The resulting deposits morphology, the velocities of the front and the properties of the velocity field of the inner part of the flows are presented and discussed.

Conclusions are drawn at the end of the thesis.

Chapter 1

Introduction to debris flows

1.1 Introduction

The flow behaviour of saturated granular materials is of interest in many applications as it arises in both nature and industry. Geophysical examples of granular flows are numerous and extremely complex in their physical behaviour since they can develop as gentle and moderately fast moving flows, such as sediment transport in rivers, lake and ocean shores, or as rapid and catastrophic events such as debris and mud flows.

Debris flows, fast moving mixtures of rock, soil and water, are recognized as the most hazardous of such flows due to their high mobility and destructive power (Jakob and Hungr 2005). Understanding the dynamics of debris flows has become a critical concern due to a worldwide increase in human settlement of mountainous regions, where the hazards and risks associated with these kinds of phenomena are the greatest.

In this chapter, an overview of the main characteristics and of the properties of the phenomenon is given in Section 1.2. This is followed in Section 1.3 by an introduction to the physical concepts proposed for the interpretation of debris flows mechanics and to the dimensional analyses suggested by Iverson (1997). Then, some of the physical modelling approaches applied to the study of specific aspects of their complex mechanics are presented. Finally, the motivations and the research work present in this thesis are summarized.

Figure 1-1 Aerial photo of typical debris flows in the alpine area of Cortina D'ampezzo, Italy (courtesy of R. Genevois)

1.2 General description and classification

Debris flows are defined as “very rapid to extremely rapid flows of saturated non-plastic debris in a steep channel” (Hungr 2005). Often they are described as “masses of poorly sorted [well graded] sediment, agitated and saturated with water, [that] surge down slopes in response to gravitational attraction” (Iverson, 1997). Differently from other related phenomena such as rock avalanches and density currents or water floods, both solid and fluid forces contribute to their motion. The fluid-solid interaction can vary from flow to flow and within the flow, but always influence strongly the debris flow dynamics, conferring upon them a unique and complex behaviour amongst observed geophysical flows. Debris flows can contain grains that range from clay to boulder in size and which are typically characterized by sediment concentrations in excess of 50% by volume (Iverson, 1997). The sediments tend to segregate, altering the material behaviour in time and space and, due to the propensity of the flow to erode and deposit material, the boundary conditions tend to be rather indeterminate. In some cases, erosion can change significantly the volume of the event during movement along its path. Consequently, debris flows volumes span a range of 100 m^3 to more than 10^6 m^3. The mean velocity during an event is of the order of several meters per second but can be as large as 10m/s.

A debris flow event may occur in a series of surges, ranging in number from one to several hundred and separated by watery inter-surge flow (e.g. Pierson, 1980). Several authors have shown, by means of visual observations, that debris flows are not homogeneous (Okuda, 1980, Costa and William, 1984; Pierson, 1980,1986). Both the concentration of the solids (and water content) and that of large clasts, are found to vary with position within the body of a surge, whose main features, as described by Pierson (1986), are shown in Figure 1-2.

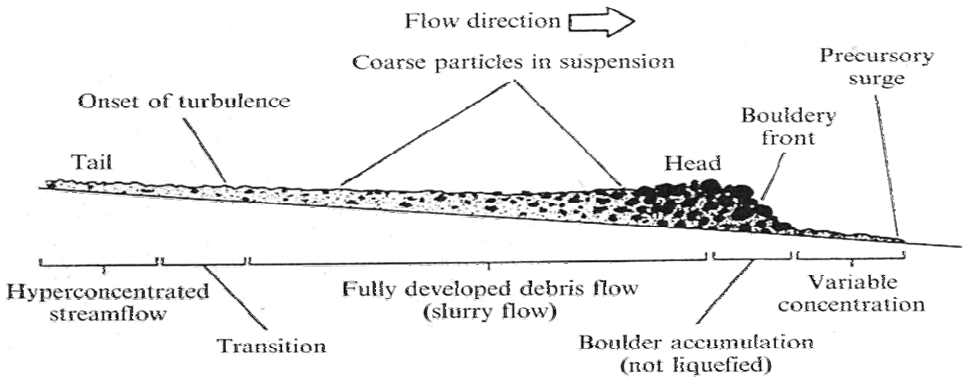

Figure 1-2 Schematic representation of a heterogeneous debris flow surge.(Pierson, 1986)

Prior to the flow front, the surge displays a “precursory surge" characterized by small flow heights and a solid concentration that increases towards the arrival of the main granular front. The head of the flow is represented by a high concentrated coarse front where the largest clasts accumulate due to a sorting mechanism, by which the larger particles gather at the upper flow surface. These particles accelerate toward flow margins as the velocities at the free surface are greater than the average. Here, the particles are not in suspension and the mixture may not be in a condition of full saturation. Behind the surge front, in the body of the flow, the material is liquefied and the coarse particles are in suspension. Eventually, the solid concentration within the surge decreases and it turns into a hyper-concentrated stream that represents the tail of the flow surge.

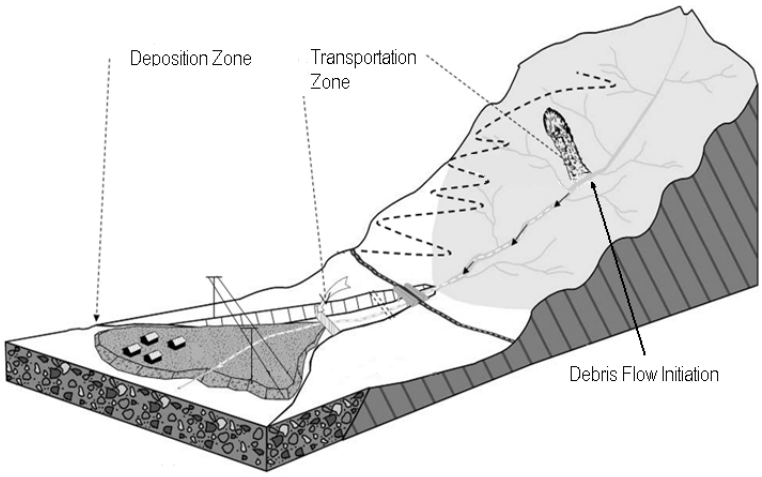

Figure 1-3 Sketch of a debris flow catchment from initiation to deposition zone

The path of a debris flow is divided into an initiation zone, a transportation zone and an area of terminal deposition, as sketched in Figure 1-3 and shown in Figure 1-4. Most often, the initiation zone, where the onset of failure occurs, is a slope failure in the headwall or side slope of a gully or stream channel. Debris flows can also occur in non-incised hillslopes. They are typically triggered on slopes with abundant unconsolidated sediments, steep gradients and scarce plant cover. In general, the area of debris flow initiation has a slope ranging between 20° and 45°, where sufficient potential energy exists to start a failure of granular soil and where the soil cover is thick and continuous enough to be vulnerable to sliding. Slopes steeper than 45° usually have a soil cover too thin to be prone to slide (Hungr, 2005). Once initiated, the rapid initial landslide can travel down slope without confinement or enter into established gullies or stream channels. Events that initiate in a gully typically remain within it. Down slope movement occurs through a transportation zone, which is typically steeper than 10°. A zone of term inal deposition occurs on an established ‘debris flow fan’ in response to a combination of slope reduction and decreased confinement.

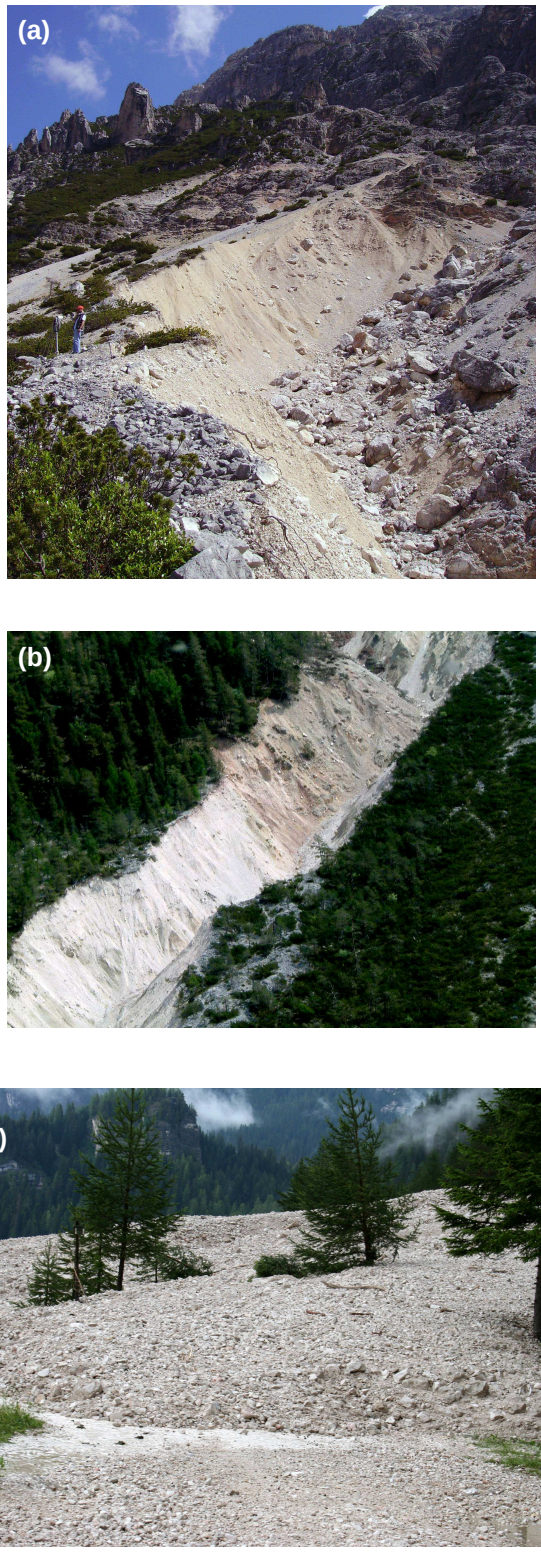

Figure 1-4 Photos of (a) initiation, (b) transportation, (c) deposition zone of debris flows in Cortina d'Ampezzo (Italy)

According to the dominant physical mechanism involved in the flow process, several classifications have been proposed for debris flow (Davies, 1988, Coussout & Meunier 1996, Takahashi, 2007). Based on the classification by Coussot & Meunier (1996), which categorizes the different flow behaviour as a function of the solid fraction and the ratio of silt-and-clay to total solid fraction, Schatzmann (2005) suggests to distinguish different flow types as shown in Figure 1-5.

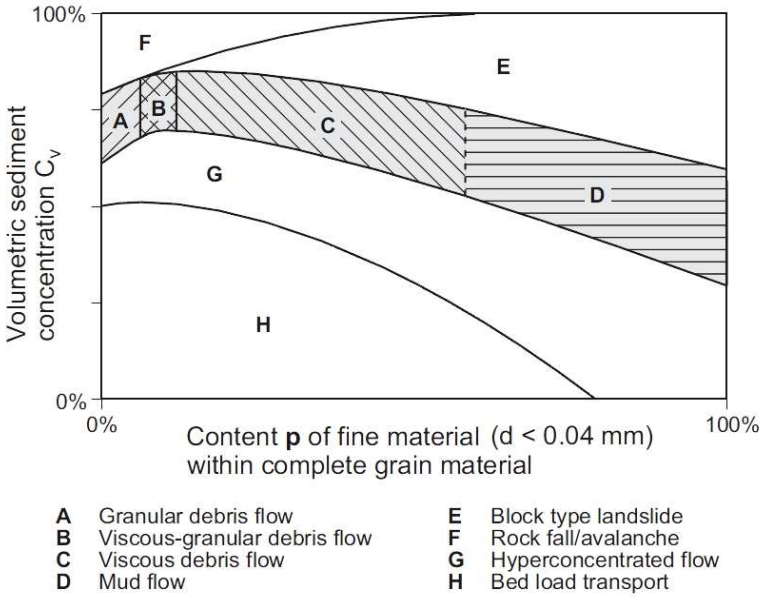

Figure 1-5 Adapted classification (A-D) of debris flows and other mass movements (E-H) following Coussot & Meunier (1996). The classification is proposed by Schatzmann (2005)

According to Schatzmann (2005) four different debris flow types can be determined: granular debris flows, viscous-granular debris flow, viscous debris flow and mudflow.

A granular debris flow comprises a small amount of fine material and a large amount of coarse particles. The solid phase is constituted of the coarser material, while the fluid phase is composed of water and very fine grains (Iverson, 1997; Takahashi 1991). Interactions between the coarser particles, due to their collisions and intergranular friction, are the dominant features within the flow process.

A viscous debris flow is characterised by a large volumetric solid fraction and a content of fine material generally larger than 10%. The grain material is poorly sorted so that the fine particles can fill the voids between the coarser particles. The collisions between the coarse particles are reduced by the surrounding mixture of fines and water that makes the whole debris flow act as a homogenous single phase.

Mudflows are characterized by a large amount of fine material but a smaller fraction of coarse particles in comparison to viscous debris flows. Depending on the sediment concentration of the mixture and on the amount of the coarser fraction, interactions between the coarser particles can occur. However, compared to a granular debris flow these interactions are less important.

Viscous-granular debris flows are debris flows exhibiting features common to both the granular and the viscous flows.

Takahashi (2001a) suggests a classification which divides debris flows in two categories. One category includes quasi-static debris flows in which particles move in enduring contact and in which Coulomb friction stresses are dominant. He states that a quasi-static debris flow can occur only when its solids concentration is more than about 0.5. The other category is represented by dynamic debris flows, which can be further distinguished according to three different types, depending on the dominant stresses involved. Debris flows in which the stress is dominated by particle collisions are called “stony debris flow”, those dominated by turbulent mixing stresses are called “turbulent muddy debris flow”, and those dominated by viscous stresses are named “viscous debris flow”. Figure 1.6 shows a ternary diagram illustrating the various types of dynamic debris flows. The parameters τ_c, τ_t and τ_v represent the shear due to grain collisions, the turbulent mixing stress and the shearing stress due to the deformation of the fluid, respectively. The three vertices of the triangle mean that τ_c, τ_t and τ_v occupy respectively a hundred percent of the total inner shearing τ. The three sides are represented by the Bagnold number (see equation 1.5), that is defined as the ratio of the inertial grain stresses τ_c and the viscous shear stresses τ_v, the relative depth h/d (where h=depth of the flow and d=characteristic diameter), and the Reynolds number, which is given by the ratio of τ_t and τ_v, and can be written as:

$$N_{Rey} = \frac{\rho_T \cdot U \cdot h}{\mu} \tag{1.1}$$

where ρ_T is the apparent density of debris flow material, U is the cross-section mean velocity and μ is the viscosity of the interstitial fluid. Takahashi terms the debris flows existing near the relative depth axis (stony, hybrid and muddy types) as inertial since the inertial stresses (τ_c and τ_t) dominate the flow.

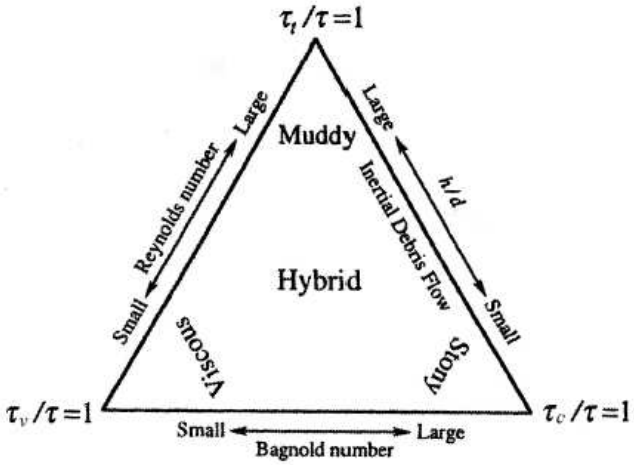

Figure 1-6 The existence domains of various types of dynamic debris flows (Takahashi, 2001a)

1.3 Physical framework for debris flow

The mechanics of concentrated particle-fluid systems, as that of a debris flow, is characterized by momentum and energy transfer caused by inertial grain collisions, grain contact friction, viscous shear, inertial (turbulent) fluid velocity fluctuations and solid-fluid interactions (Iverson 1997). Rheological models, describing debris flow as a single-phase material which behaves according to a constitutive relationship between the operating shear stress and the rate of strain, are often used to describe the flow behaviour.

The viscoplastic flow model, known as Bingham model, developed almost simultaneously by Johnson (1965) and Yano & Daido (1965) has been widely adopted to explain debris flows. This model describes a debris flow as a single-phase material that remains rigid till applied stresses exceed a threshold value (the yield strength). Such a continuum behaves as a Newtonian fluid when the stresses are larger than the yield strength. When the driving shear stress drops below the yield strength, the whole flow stops en masse. The Bingham constitutive equation, in one-dimension (Johnson, 1965), is:

$$\tau_{zx} - \tau_o = \mu \frac{du}{dz}; \qquad \tau_{zx} > \tau_o \tag{1.2}$$

$$\frac{du}{dz} = 0; \qquad \tau_{zx} \le \tau_o \tag{1.3}$$

where τ_{zx} is the driving shear stress, τ_o is the yield strength in shear, du/dz is the velocity gradient normal to the bed and μ is the Bingham viscosity (Whipple et al. 1997).

The yield strength may be generalized by adding a frictional strength component that depends on the normal stress acting on planes of shearing, in which case the viscoplastic model may be referred to as the Coulomb-viscous model (Johnson, 1965, 1970, 1984)

$$\tau = c + (\sigma - p)\tan\varphi + \mu\left(\frac{du}{dz}\right) \tag{1.4}$$

where c is the cohesive strength, φ the internal friction angle and σ is the effective normal stress.

This model can explain several key features of debris-flow processes, such as the presence of a relatively undeformed material (rigid plug) observed during the motion of channalized debris flow, lateral levees, and large floating clasts. However, it is applicable only to muddy, matrix-rich debris flows that leave matrix-supported deposits (Whipple, 1997).

The viscoplastic model does not account for the interactions between particles and between the particles and the fluid, which play a relevant role in generating shear resistance, transferring momentum, and producing diverse grading patterns and clast fabric in debris flow deposits (Iverson and Denlinger, 1987; Iverson, 1997)

To account for grain-fluid interactions Takahashi (1978, 1981, 1991) proposed an alternative model for debris flows by applying Bagnold's concepts (1954) regarding the mechanics of grain collisions. Takahashi described debris flows as inertial grain flows of uniformly dispersed particles in which momentum transfer and energy dissipation occur via grain collisions.

Bagnold (1954) conducted shear experiments with dispersions of neutrally buoyant wax spherical particles in a glycerine-water-alcohol mixture. He defined the following dimensionless N_{BAG} number (Bagnold number), which expresses the ratio between inertial stresses (stresses induced by collisions of the spheres) and viscous stresses (stress induced by the viscosity of the liquid)

$$N_{BAG} = \frac{\lambda^2 \cdot \rho_s \cdot d^2 \dot{\gamma}^2}{\lambda^{1.5} \cdot \mu \cdot \dot{\gamma}} = \frac{\lambda^{0.5} \cdot \rho_s \cdot d^2}{\mu} \cdot \dot{\gamma} \tag{1.5}$$

Where d is the diameter of the particles, μ is the Newtonian viscosity of the liquid, ρ_S is the density of the solid spheres and $\dot{\gamma}$ is the shear rate. The parameter λ=d/s, defined as the ratio of the particle diameter to the mean free distance between the particles (s), represents the linear concentration. Bagnold observed a linear relationship between shear rate and shear stress for low shear velocities and called this the macro-viscous flow regime, defined for N_{BAG} < 40.

Measurements of normal stress showed the same proportionality to the shear rate, and Bagnold estimated the effective dynamic friction coefficient, calculated as the ratio between normal stress σ and shear stress τ to be 0.75:

$$\tau = B \cdot \lambda^{1.5} \cdot \mu \cdot \dot{\gamma} \tag{1.6}$$

$$\tau/\sigma = \tan\alpha \tag{1.7}$$

where B is an empirical constant equal to 2.25 and α is the dynamic friction angle

For higher shear velocities, the shear stress and the normal stress were found to be proportional to the square of the shear rate γ and were independent of the fluid viscosity. This is known as the grain-inertia regime, defined for $N_{BAG} > 450$. The effective dynamic friction coefficient was estimated to be 0.32:

$$\tau = a \cdot \sin\alpha \cdot \rho_s \cdot \lambda^2 \cdot d^2 \cdot \dot{\gamma}^2 \tag{1.8}$$

$$\tau/\sigma = \tan\alpha \tag{1.9}$$

where a is an empirical constant equal to 0.042 and α is the dynamic friction angle.

Finally, in the transition regime the dependency of the shear and the normal stress from the share rate progressively changes from linear to quadratic. This is defined for values of N_{BAG} between 40 and 450.

Bagnold hypothesized that the pressure and the shear stress in the inertial region were produced by interparticle collisions. Bagnold termed the normal pressure as “dispersive” pressure, because it scatters the particles, allowing them to be sheared. In the macro-viscous region, grains contributed only to the increase the viscosity of the fluid, whereas in the inertial regime the effects of the fluid viscosity became negligible.

Takahashi (1991) applied Bagnold’s constitutive equations in the inertial regime to a stony-type debris flow (i.e. a debris flow in which the stress is dominated by particle collisions). Based on the momentum equation for both solids and liquids, and neglecting the turbulence and the viscosity of the interstitial fluid, the shear stress τ of the whole mixture can be expressed as:

$$\tau = \xi\left(\frac{du}{dz}\right)^2 \tag{1.10}$$

Where ξ is a function of grain size, solid concentration, particle density and dynamic angle of internal friction. The term (du/dz) represents the shear rate. A fluid represented by the following equation $\tau = (du/dz)^n$ with n>1 is called a dilatant fluid. Consequently Takahashi's model is also known as "dilatant model". Such a model provides a basis for estimating the stress developing in grain-inertial flows, but it does not properly account for the role of interstitial fluid which influences grain interactions during a debris flow's motion (Iverson and Denlinger, 1987; Iverson, 1997).

During the last decades many attempts have been made to formulate a model able to take into account all the different momentum-transport processes involved in a debris flow (Iverson and Denlinger, 1987; Chen, 1988a,b; Julien and Lan, 1991; Hutter et al., 1996; Iverson, 1997; Jan and Shen, 1997; Julien and O'Brien, 1997; Takahashi, 1997; Coussot and Ancey, 1999)

Since debris flows are generally considered as mixtures of solids and fluids, two-phase models have been recently developed (e.g., Denlinger and Iverson, 2001; Pitman et al., 2003; Pudasaini et al., 2005). Such models are also known as "mixture theories".

The pilot version of mixture theory, proposed by Iverson (1997) and Iverson & Denlinger (2001), describes the fluid (with fine particles carried in suspension) as a Newtonian viscous fluid while the granular components as Coulomb frictional materials behave according to the following equation:

$$\tau = \sigma' \tan\varphi + c \tag{1.11}$$

where σ' is the effective normal stress; φ is the angle of internal friction and c is the cohesion parameter.

The coupled solid and fluid obey Terzaghi's effective-stress principle

$$\sigma' = \sigma - u \tag{1.12}$$

where u is the pore pressure and σ is the total normal stress. They follow also Darcy's law for drag due to relative motion of the solid and fluid phases. In Iverson's (1997) model, the pore-fluid pressure is the key variable, which specifies the behaviour of the mixture. The behaviour of the mixture reduces to a Coulomb solid when pore pressure is absent and to a viscous fluid when the pore pressure is enough for complete liquefaction. The evolution of the pore pressure is defined by a forced diffusion equation, which reduces to the standard soil consolidation equation for quasi-static mixtures.

1.4 Dimensional analysis of debris flow

In order to assess the relative importance of the different energy dissipation mechanisms acting within a debris flow and to distinguish between different flow regimes, Iverson (1997) and Iverson and Delinger (2001) carried out a dimensional analysis in which they proposed a series of dimensionless numbers relevant to specific mechanical processes. They also suggested ranges of values to determine the dominant regime for the flow under investigation.

Such dimensional analysis assumed idealized kinematics (uniform simple shear flows) of a uniform grain-water mixture, composed by identical solid spheres under the action of the gravitational forces. Despite its simplicity, this schematic model provides a basis for assessing scaling parameters which influence the different debris flow stresses.

Considering δ, the characteristic grain diameter as the characteristic length, $\rho_s \delta^3$ as the characteristic mass and $1/\dot{\gamma}$ as the characteristic time, the proposed dimensionless parameters can be written as follows (definitions of other symbols are given in the Notation section):

The Savage Number is defined as the ratio between the inertial shear stresses associated with grain collisions and the stresses due to grain contacts. It characterises the flow regime as collision or contact dominated. Savage and Hutter (1989) suggested that N_s>0.1 represents the transition to a grain inertial regime, where particle collisions dominate the flow dynamics

$$N_S = \frac{\rho_s}{(\rho_s - \rho_f)} \frac{\delta^2 \dot{\gamma}^2}{gH} \tag{1.13}$$

The Bagnold Number is defined as the ratio of grain collisions stresses to the viscous fluid stresses, and explicitly excludes the shear stress from Coulomb friction. It is therefore more influential when flow is dominated by brief collisions rather than prolonged contact; i.e. N_s>0.1. Grain collisions are found to be dominant when N_B>450, while N_B<40 describes a “macroviscous” regime, where shear and normal stress are found to be proportional to shear rate.

$$N_B = \left[\frac{v_s^{1/3}}{v_*^{1/3} - v_s^{1/3}} \right] \frac{\rho_s \delta^2 \dot{\gamma}}{\mu} \tag{1.14}$$

The Quasi-Reynolds Number is analogous to the traditional Reynolds Number, in which $\sqrt{gL}$ acts as characteristic velocity. Large (field) flows are characterised by $N_R > 10^6$ (Iverson and Delinger, 2001), while small (laboratory) flows have much lower values. A consequence of the momentum equation proposed by Iverson and Denlinger (2001) is that viscous effects are more dominant in smaller flows.

$$N_R = \frac{\rho H \sqrt{gL}}{\mu v_f} \tag{1.15}$$

The Fluidisation Number is the ratio between the velocity scale for fluidisation of the mass and the velocity scale of particles falling within the flow. A value of $N_F<1$ suggests the solid and fluid phases experience similar velocities and accelerations, allowing the mass to be treated as a coherent mixture. Typically, for debris flows, $N_F<<1$.

$$N_f = \frac{k(\rho_s - \rho_f)\sqrt{g/L}}{\mu} \frac{v_s}{v_f} \tag{1.16}$$

The Pore Pressure Number represents the ratio of the time for down-slope motion to the timescale for pore pressure diffusion, normal to the flow direction. Field scale debris flows have $N_P<<1$, indicating that, if high pore pressures develop within the flow, they persist much longer than the timescale for the down slope motion (Iverson and Denlinger 2001).

$$N_P = \frac{D\sqrt{L/g}}{H^2} \tag{1.17}$$

The flow aspect ratio is the ratio of flow thickness to the flow length. It is a measure of the flow mobility. According to Iverson and Denlinger (2001), there should be no scale dependence between model and field-scale flows.

$$\varepsilon = \frac{H}{L} \tag{1.18}$$

Some typical values of the non dimensional numbers for some well documented grain-fluid flows (reported by Iverson and Delinger, 2001) are presented in Figure 1-7.

	Symbol (Units)	Flow Location and Type: USGS Flume Debris Flows[b]	Yake Dake Debris Flows[c]	Mount St. Helens Pyroclastic Flows[d]
Physical parameters				
Friction angles	φ_{int}, φ_{bed} (deg)	28–42	25–50	25–50
Solid volume fraction	v_s (none)	0.6	0.6	0.4
Fluid volume fraction	v_f (none)	0.4	0.4	0.6
Solid density	ρ_s (kg/m^3)	2700	2600	2600
Fluid density	ρ_f (kg/m^3)	1200[f]	1200[f]	2[g]
Fluid viscosity	μ (Pa-s)	0.1[f]	0.1[f]	2×10^{-5} [g]
Typical grain diameter	δ (m)	0.01	0.2	0.01
Mixture density	ρ (kg/m^3)	2000	2000	1000
Hydraulic permeability	k (m^2)	10^{-11}	10^{-8}	10^{-11}
Hydraulic diffusivity	D (m^2/s)	10^{-4}	0.001	0.01
Flow shear rate	$\dot{\gamma}$ (1/s)	50	3	10
Flow thickness	H (m)	0.2	2	1
Flow length	L (m)	100	1000	2000
Dimensionless parameters				
Flow aspect ratio	ε	0.002	0.002	0.0005
Savage number	N_S	0.2	0.03	0.001
Bagnold number	N_B	600	1×10^4	3×10^5
Quasi-Reynolds number	N_R	3×10^5	1×10^7	1×10^{10}
Fluidization number	N_f	7×10^{-8}	2×10^{-5}	6×10^{-5}
Pore pressure number	N_p	0.008	0.002	0.1

[a]To estimate Bagnold numbers, maximum volume fractions of solid grains were assumed equal to 0.7.
[b]*Iverson* [1997a].
[c]*Takahashi* [1991].
[d]*Rowley et al.* [1981], *Wilson and Head* [1981], and *Hoblitt* [1986].
[e]*Hsu* [1975, 1978].
[f]Muddy water.
[g]Dusty air.

Figure 1-7 Typical values of physical and dimensionless number for well-documented granular-fluid flows (Iverson and Denlinger, 2001)

Dimensional analysis is a useful tool to discriminate between different flowing regimes. However, it must be noted that such analysis presents some limitations. First, it results from an idealized kinematics, which neglects some important aspects, like the variation in granular temperature and solid concentration and the energy conversion and dissipation at the flow boundaries. Mostly important, the analysis neglects the fact that debris flows develop as unsteady, non-uniform surges, comprising grains with a large range of sizes.

1.5 Physical Modelling of debris flows

The mechanics of debris flows can be investigated using different approaches, such as physical modelling, field observation or analytical/numerical modelling. All these methodologies have advantages and shortcomings.

Direct observations of debris-flow parameters in the field improve the knowledge of their triggering mechanisms and of the subsequent behaviour of the flow. In addition, accurate field data are

essential for the validation and the calibration of numerical simulations. Unfortunately, in situ observations are extremely difficult to make due to the unpredictability of the timing and location of such catastrophic events and the difficult access to the involved sites. Real-time field observations and measurements are therefore relatively rare (Okuda et al.,1980, Pierson, 1980,1986, Johnson, 1984, Suwa, 1989). Automated debris flow monitoring sites have been recently installed in order to partially overcome this problem (Arattano et al., 1997, Berti et al., 1999, Arattano & Marchi, 2000, McArdell et al., 2007, McCoy, 2010).

Since the initial and boundary conditions of natural debris flows may be indeterminate, a better understanding of the related mechanics can be attained if data from monitoring are used in combination with physical tests or/and numerical analyses. Physical modelling allows the phenomena to be analysed in controlled experiments with well-defined boundary conditions and known parameters. The close control over the model details leads patterns of response to particular input perturbations to be obtained, enabling repeatability and hence, parametric studies to be conducted (Davies at al, 2010). On the other hand, numerical modelling makes possible the simulation of the phenomena at the prototype scale with boundary conditions that are unattainable in a physical model. Therefore, through such combined approaches the understanding of the complex behaviour of debris flow can be enhanced.

Both full-scale and small-scale physical models have been widely used to investigate specific aspects of debris flow mechanics. A major limitation of physical models is the lack of certainty in the application of the scale model findings to the field-scale debris flow behaviour. Iverson (1997) and Iverson and Denlinger (2001) state that scaling is a crucial issue in small-scale experimental flows, which are unlikely to mimic the key behaviours at geophysical scale. This assumption has been supported by analyzing the dependency of the scaling parameters N_R and N_P (equations 1.15 and 1.17) with the flow size (measured by the characteristic thickness H). As flow size increases, values of the scaling parameter N_R increase as well, indicating that viscous shear resistance, relative to inertia stresses of the flow, become less important. In contrast, values of the scaling parameter N_P decrease, indicating that dissipation of non-equilibrium pore fluid pressures occurs very rapidly with respect to the duration of the flow motion. The opposite trends of N_R and N_P suggest that debris flows at field-scale exhibit negligible viscous effects and significant pore pressure effects, whereas the opposite is likely to occur in flows at the small scale of laboratory experiments. Such issues instigated Iverson and co-workers to perform debris-flow experiments at the largest possible scale, using a flume 95 m long, 2 m wide, and 1.2 m deep (USGS flume), able to provide a flow scale equivalent to a small-sized natural debris flow (Major and Iverson, 1999; Iverson, 2010). The large concrete flume has an upstream 88m reach with a constant slope of 31°, while the last 7m gradually flattens to a runout area that slopes at 3°. From 1994 to 2004, 28 large-scale experiments were conducted. Two different particle size distributions were used; a sand-

gravel material (66% gravel, 33% sand, and 1% mud) and a sand-gravel-mud (56% gravel, 37% sand, and 7% mud). Before the experiments 10m^3 of debris flow material were prepared behind a steel gate at the head of the flume and saturated with water. Basal fluid pressure and basal total normal pressure were measured at 67m below the release gate and at several locations on the runout area. The results of these tests show that the segregation of the material occurs during the down slope motion, with the coarser particles being concentrated at the front. Furthermore, the basal fluid pressure is almost zero at the leading front while, in the interiors of the flow, it gradually increases as much as the total normal stress, indicating that the material is liquefied. These characteristics agree well with field observation (Okuda, 1981; McArdell, 2007).

Figure 1-8 U.S. Geological Survey large-scale debris flow flume (Logan and Iverson, 2007)

The measurements at the runout area show that the excess fluid pressure can last for a long time and dissipates significantly only during the post depositional consolidation. Therefore, the debris flow deposit is not formed by en masse deposition, but results from the grain contact friction and bed friction concentrated at the flow margins, where the fluid pressure is nearly absent. When the driving stress cannot overcome the friction at the flow margins, the liquefied debris flow material

stops as if it is dammed by the coarse front. These results demonstrate that the development of dilated, high friction, coarse grain flow fronts, pushed from behind by a liquefied body is a key feature of debris flow dynamics. The persistence of high pore pressure in flow body, promotes the high mobility of debris flow. Moreover, grain size segregation is not just a distinctive morphological feature, but it plays a fundamental role in debris flow dynamics.

Despite the aforementioned issues about the reliability of the scaling for debris flow, useful physical model research on debris flows has been accomplished at small laboratory scale. Even if it is difficult to match dimensionally all the different aspects of large-scale flows, it is meaningful to try to reproduce specific aspects in isolation, reducing the overall complexity of the phenomena and focussing on the most relevant aspects for the specific mechanism under investigation.

Studies in small scale flumes have been carried out to analyze, for instance, the effect of granular and water contents on the runout, the influence of bed topography, saturation and density on overall behaviour and the role of interparticle fraction on debris flow dynamics (Chau et al, 2000; Rombi et al., 2006; Itoh et al, 2000)

Centrifuge model testing represents a different relevant tool available for the physical modelling of debris flow (Bowman et al., 2006; Horii et al., 2002). Recently geotechnical centrifuge tests have been carried out to elucidate, in particular, the mechanics of erosion and entrainment (Bowman et al, 2010). Bowman et al. (2010) hypothesized that the stress applied by a debris flow has a direct influence on the effective strength of the soil beneath it and therefore on its tendency to erode. That is, the drained strength of the bed is a function of the effective stress applied to it, while its undrained behaviour is a function of the path length and the soil permeability. Laboratory-scale flows at 1g are not generally adequate for simulating the drained and undrained mechanisms of bed erosion, due to the effects of the involved stress level, substrate thickness and permeability. Geotechnical centrifuge modelling gives the opportunity to test a small-scale debris flow of 1/N scale, where N is the scale factor, under an acceleration field N times the Earth's gravity, i.e. Ng. This allows to examine the failure of the bed and its entrainment, at stresses that approximate the field values and, by a careful selection of the material, to replicate the correct diffusion-inertial times. Bowman et al. (2010) compared the non-dimensional numbers calculated for the tests in centrifuge, with those obtained from two field cases, as well as those from typical laboratory-scale flows and the USGS large-scale flume. The results show a closer match of dimensionless numbers than for small scale tests conducted at 1g, indicating that centrifuge test can match particular aspects of behaviour of field-flows, which are difficult to replicate at small scale at 1g.

A different type of experiment relies on the observations of granular flow behaviour over an extended period of time, making the analyses of the flow in steady-state conditions possible. Usually this goal is achieved by means of conveyor-belt flumes (Hirano & Iwamoto, 1981; Davies,

1990; Kaitna et al, 2006) or rotating drums (Hotta & Ohda, 2000, Kaitna & Rickenmann, 2005; Hsu et al, 2008).

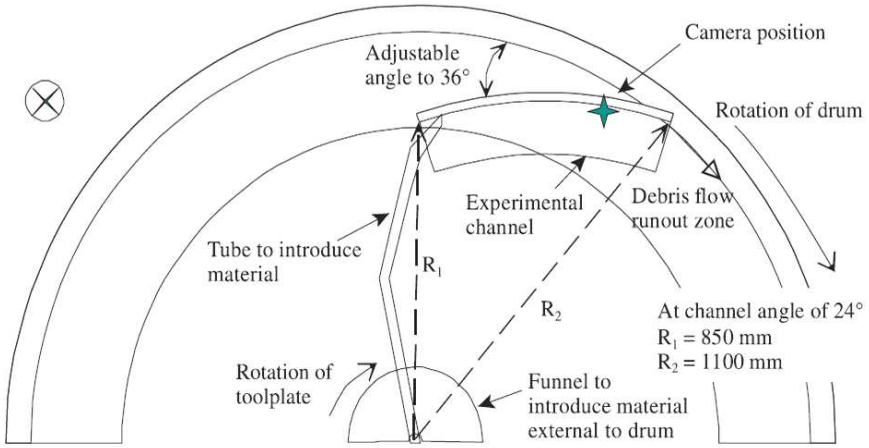

Figure 1-9 Schematic view of the debris flow channel within the drum centrifuge at ETH Zurich (only half of the drum shown). The image is from Bowman et al. (2010).

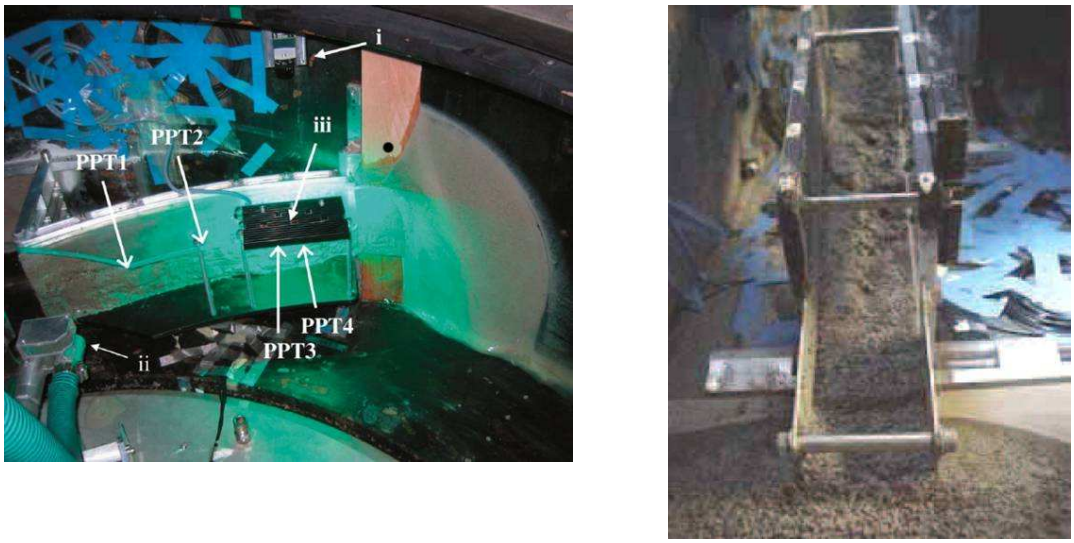

.Figure 1-10 Photos of debris flow channel and runout zone after a test in conducted at the ETH Zurich drum centrifuge (Bowman et al., 2010; Davies et al.,2010)

The former devices are flumes in which the bed moves upchannel at a constant velocity between stationary walls. A surge is generated by introducing water and grains on to the moving belt at the upstream end of the flume. Then, the belt speed, bed slope and water supply are set in order to keep the average position of the surge stationary with respect to the walls. Although the obtained

wave of unchanging shape, moving steadily downstream in a channel, does not fully resemble a debris flow surge, it represent an acceptable simplification for a preliminary investigation into some aspects, such as velocity profiles and zones of different flow types. The rotating drum is based on the same concept as the conveyor-belt flume, i.e. to establish steady flow conditions at different velocities and to measure relevant flow parameters.

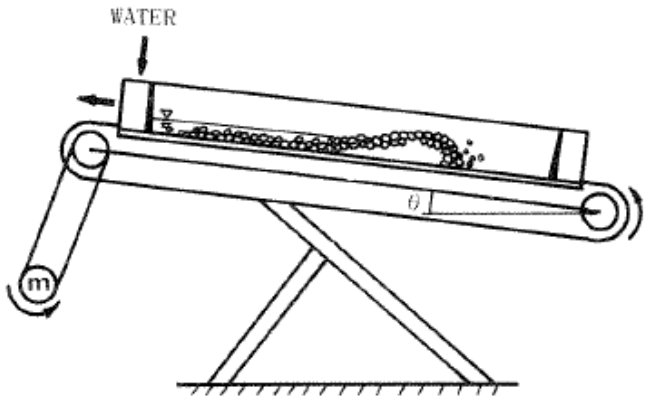

Figure 1-11 Schematic diagram of the conveyor-belt flume used by Hirano (1981)

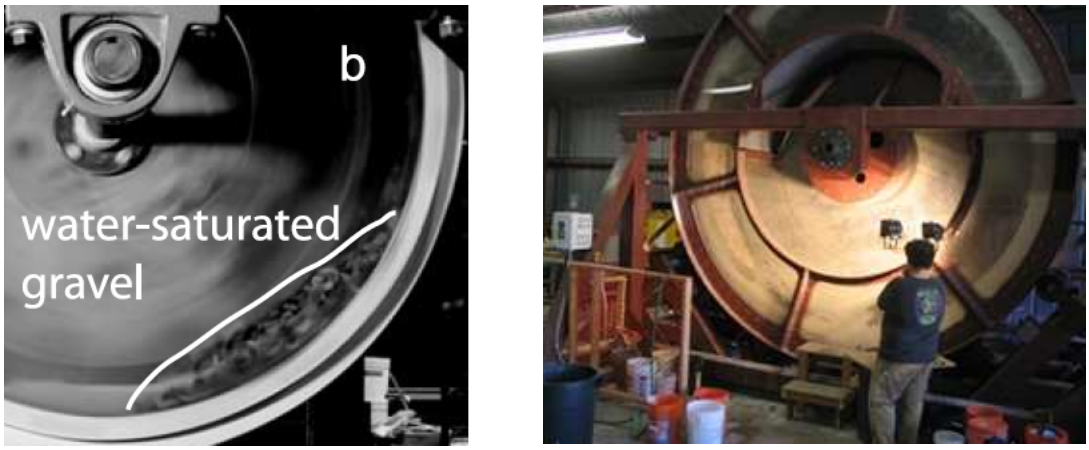

Figure 1-12 Granular flows in rotating drums at University of California (Berkeley). Picture of a granular flow in a-small-scale drum (inner diameter=0.56m, width=0.15m) on the left. Photo of a large-scale drum ((inner diameter=4m, width=0.8m) on the right (Hsu et al., 2008)

1.6 Objective: physical modelling of debris flows with standard and optical approaches

The aim of this doctoral research programme is to investigate through a physical modelling approach, the flow and the deposition of solid-fluid mixture with a view to understanding the mechanics of debris flows. For this purpose, two different approaches have been adopted. The first is based on a series of experimental tests carried out using a small-scale flume and natural material (i.e. soil and water). The second relies on the application of a non intrusive optical technique to the investigation of granular flows in small-scale flume experiments. In this case an artificial material, Duran borosilcate glass and a hydrocarbon oil, has been used for the mixture. In the following sections the motivations and a short overview of the accomplished work will be given.

1.6.1 The role of particle size in the flow behaviour of saturated granular materials

Source debris flow materials are the result of natural erosion processes due to mechanical and/or hydraulic agents and hence they are related to the particular geomorphology and geoclimatic situation of the area. The characteristics of the solid particles, such as grain shape and size, texture and density, strongly affect the rheological behaviour of debris flows. However, irrespective of the particular features of the sediments, field evidences show that virtually all debris flows contain a wide particle size distribution (PSD), with sizes ranging from boulders or gravel to silt and clay. This aspect is clearly shown in Figure 1-13 and Figure 1-14, which present the material gradation curves of some debris flows located in Italy, Switzerland, and Japan. Although many grain size distributions do not take into account the presence of large cobbles and boulders, which are hard to sample, debris flows material is in general are comprised mostly of gravel and sand with a percentage of fines, i.e. silt and clay particles, that is less than 10% of the total mass (Iverson, 1997). The typical mean particle size, D_{50}, ranges between 2mm and 200mm and typical reported uniformity coefficient values, $C_U = D_{60}/D_{10}$, are of the order of 100-1000 (e.g. Hurlimann 2003; Roesli 1990; Takahashi 1991). A number of experimental studies have been instigated to examine the motion and arrest of flowing saturated granular materials, with a view to understand debris flows (Itoh, 2000; Larcher, 2007; Mainali 1994). However, few previous experimental studies have explicitly considered the influence of the particle size distribution (PSD) on their behaviour (Takahashi 1991). Typically, experimental flows are characterized by a mean particle size which is necessarily smaller than that found in the field and use a relatively uniform PSD ($C_U<5$). Unsurprisingly, important aspects of their behaviour, such as the effects of flow segregation, are unable to be replicated in such tests.

Experimental research has therefore been undertaken as part of this PhD to determine if the well-graded nature of debris flow materials is key to their tendency to travel fast and far before final deposition. A number of tests using soil with different gradation, i.e. with different C_U, C_Z and D_{50} values, were performed at a given moisture content. The details of the adopted methodology will be described in Chapter 2, while the results will be presented in Chapter 3.

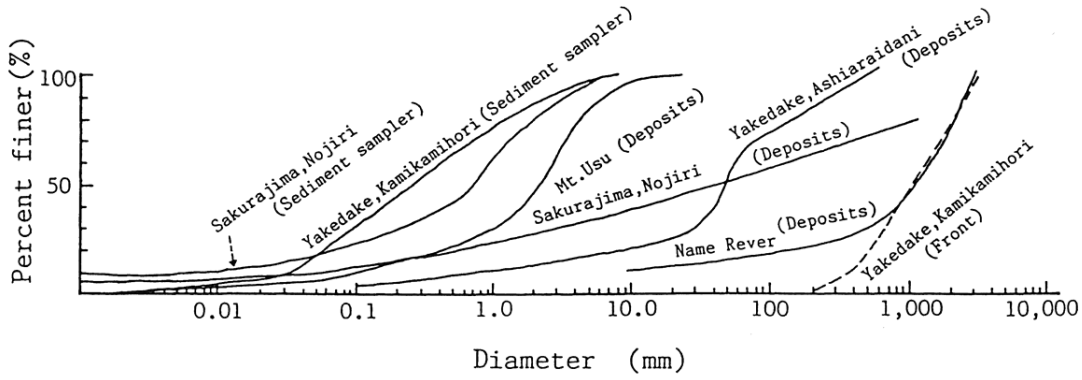

Figure 1-13 Particle size distributions in various debris flows in Japan (Takahashi 1991)

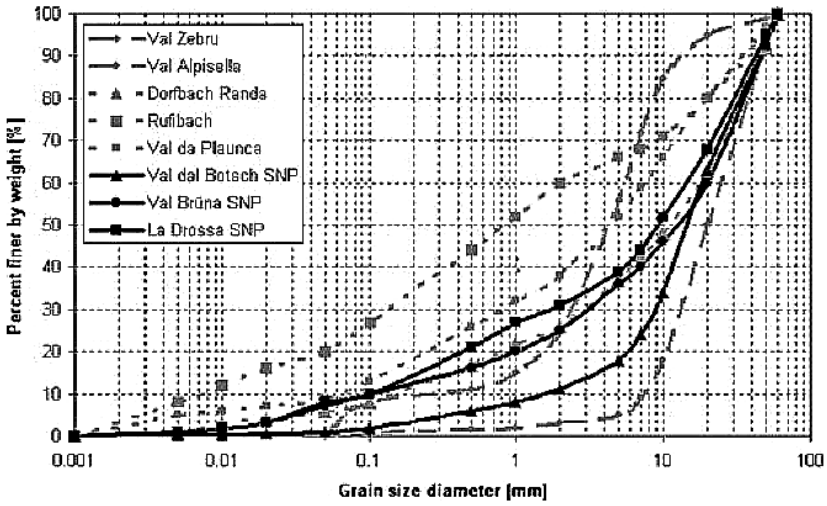

Figure 1-14 Particle size distribution for different debris flows in Alpine areas and the Swiss National Park (data is taken from Stolz 2008).

1.6.2 Optical investigation through a flowing saturated granular material

In debris flow physical modelling experiments it is possible only to examine the behaviour of the phenomena under investigation at the flow margins (usually the top and the sides) since the ability to probe the internal behaviour of concentrated two-phase flows is prevented by their high opacity. Experimental evidence shows that the dynamics of the inner part of the flow can be different from the motion close to the sidewall (Armanini et al. 2005). In fact, the two dimensional nature of the sidewall measurements probably reflect only partially the three-dimensional conditions near the sidewall and they cannot exhibit the three-dimensional features of the flow inside the bulk.

In order to overcome these limitations and extend the current understanding of flow dynamics, non-intrusive measurement techniques that can visualize the arrangement of the particles and extract velocimetry data from the interior of the mixture are required. One well-known method used to achieve optical accessibility to the interior of particle–liquid media consists of matching the refractive index of transparent solids and fluid. Optical matching renders the entire system transparent, allowing direct optical probing of internal points. Combining refractive index matching and planar laser–induced fluorescence (PLIF) techniques enables the visualization of deformation within the flowing saturated granular material and makes the use of deformation measurement techniques, as Particle Image Velocimetry (White et al., 2003), possible.

Refractive index matching methods have been widely used to obtain optical access to liquid flow phenomena (Budwig, 1994) and their application to porous media using PLIF has been undertaken by (Fontenot and Vigil 2002; Montemagno and Gray 1995; Stohr et al. 2003; Tsai and Gollub, 2004; Orpe and Kudrolli, 2007).

This thesis examines the feasibility of applying this technique to a context resembling that of a laboratory debris flow test that is a highly concentrated particle-fluid system in a free-surface condition and in the context of high speed-movement. In Chapter 4, the test procedure, and the physical and optical properties of the selected solid and liquid are described. In the same chapter the method used to enable comparable behaviour of the mixture to that of real granular soil and water is also reported, together with the description of the experimental set up and its tuning. Finally the results and the images obtained in a preliminary set of tests are presented and discussed in Chapter 6.

Chapter 2

Experimental research using a standard small scale flume apparatus

2.1 Introduction

Although debris flows are high speed gravity-driven mixtures of soil, rocks and water (Hungr, 2001), characterized by a volumetric sediment concentration higher than 50%, they have been studied in fluid mechanics more often than in granular mechanics. Consequently, the influence of important granular properties, such as soil particle gradation, on the behaviour of debris flows has not been sufficiently investigated. Field evidence shows that virtually all debris flows contain a wide particle size distribution (PSD), which contains grains that range from clay to boulder size. An experimental programme has been undertaken as part of this PhD research to determine if the well-graded nature of debris flow materials is important to their high mobility. The adopted experimental setup and methodology are reported in this chapter. In particularly, in Section 2.2 the basic concepts of the dynamic model proposed by Takahashi (1979) and Hungr (1984) for the estimation of the runout length are introduced. This model is subsequently applied to the results in Chapter 3. In Section 2.3 a brief overview of the previous research conducted using the same apparatus is given together with the main findings. Finally, the experimental procedure is described in Section 2.4. The flume apparatus is illustrated in Section 2.4.1, the material and its characterisation are described in Section 2.4.2, the details of the test procedure are explained in Section 2.4.3, and the measurement methods are reported in Section 2.4.4

2.2 Background

In the field, engineers are concerned mainly with two aspects of granular flow, namely, how far such flows can travel and what forces are generated on obstacles along its path (Hungr et al., 1984; Wendeler at al., 2002). Well-graded debris flows constitute the most hazardous of these flows (Skermer, 2005), and the prediction of runout distance is the fundamental element to delineate the endangered areas located along alluvial fans and the siting of mitigation structures.

Debris flows exist where mountainous terrain and high runoff co-exist and tend to travel down a series of confined channels or reaches, eroding and entraining or depositing material as they proceed. Whether they erode or deposit depends on the channel geometry, the flow velocity, the flow constituents and the bed constituents. The runout zone may be considered as the final deposition area. For well-established debris flow channels, a relatively shallow deposition fan at the base of steeper terrain may mark this point. This is often where also human habitation commences and where the interest of engineers begins.

Research has shown that the final runout distance of a debris flow on level ground or a gently sloping fan for a particular geoclimatic situation (Hungr et al., 1984; Takahashi, 1980) is relatively well correlated to the velocity of the flow head at the point at which it exits a confined reach. Hungr and Takahashi proposed a dynamic model based on the work of Takahashi and Yoshida (1979) to estimate of the runout length on the deposition area. The model assumes a constant discharge from the upstream channel and a trapezoidal shape for the debris flow surge, as shown in Figure 2-1

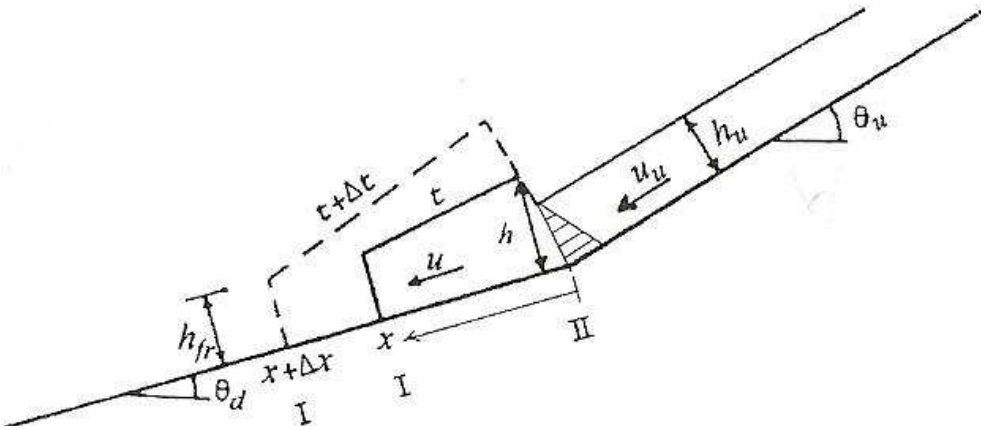

Figure 2-1 Process of the stoppage of forefront of a debris flow (Takahashi 2007)

According to the momentum conservation, a steadily debris flow moving from a steep channel into a surface where the slope abruptly levels out, decelerates and stops at a runout distance x_T given as follows:

$$X_T = \frac{V_e^2}{G} \tag{2.1}$$

$$V_e = v_u \cos\left(\theta_u - \theta\right)\left[1 + \frac{g h_u \cos\theta_u}{2 v_u^2}\right] \tag{2.2}$$

$$G = g\left(S_f \cos\theta - \sin\theta\right) \tag{2.3}$$

where:

x_T runout distance,
v_u upstream debris velocity,
θ_u entrance slope angle (channel slope),
θ runout slope angle (fan slope),
g acceleration due to gravity,
S_f friction slope,
h_u upstream debris flow depth

Equation (2.2) describes the kinematics of the driving component of the debris flow mass, as a function of the mean angle of the upstream reach and the deposition fan, the entry velocity and depth. Equation (2.3) describes the resistance to the flow with the friction slope S_f, accounting only for sliding friction, which is assumed to be constant along the runout path.

As well as the gravity force that acts on all landslides that begin their motion from a standstill position, Equation (2.1) shows that momentum is a major driver of debris flows within the zone of interest to engineers. Hungr et al. (1984) applied Equation (2.1) to five debris flows in western Canada and found good agreement between the estimated runouts and the corresponding observed data, assuming S_f=tan10°.They obtained the flow parameters v and h from design discharge, by means of empirical equations suggested for uniform flows of debris in channel.
As noted by Rickenmann (2005) several variations on the form of this equation exist, while coefficients of correlation depend on the specific region or catchments in the field. Better predictions of the runout lengths were obtained for Japanese debris flows at the Kamikamihori

valley using measured flow parameters (Okuda and Suwa, 1984) and for 12 Swiss debris flows of 1987 using instead of S_f =tan10°, a friction slope of S_f =1.12tanθ and S_f =1.08tanθ, respectively.

The dynamic model proposed by Takahashi (1980) and Hungr et al. (1984) has been applied also to experimental results obtained from small scale flume tests (Takahashi, 2007; Chau et al., 2000), where the resistance to the flow, assuming a dilatant fluid model for stony debris flows, is given by the following expression:

$$G = \frac{(\rho_s - \rho_m) g C_s \cos\theta_d \tan\alpha_i}{(\rho_s - \rho_m) C_s + \rho_m} - g \sin\theta_d \qquad (2.4)$$

where

ρ_m apparent density of fluid incorporated with suspended particles,

ρ_s density of the particles,

C_s volume concentration of the solid in flow (assumed constant),

α_i dynamic friction angle of the particles

Figure 2-2 shows the comparison between the runout distances calculated by means of the dynamic model (solid line) with those observed in flume experiments (black circles; Takahashi, 1980) and in the field (with circles; Hungr, 1984). The model equations appear to capture essential elements of the debris flow behaviour for both types of data (field and laboratory).
It should be noted that a debris flow may be arrested at any point (either within a confined channel or in an unconfined zone) also due to the friction at flow margins (Major and Iverson 1997). A debris flow will therefore travel furthest over a particular reach if either its entry velocity is high or the margin friction is low.

In the experiments presented in the next chapter, we will consider the final reach of a debris flow channel before an unconfined deposition zone.

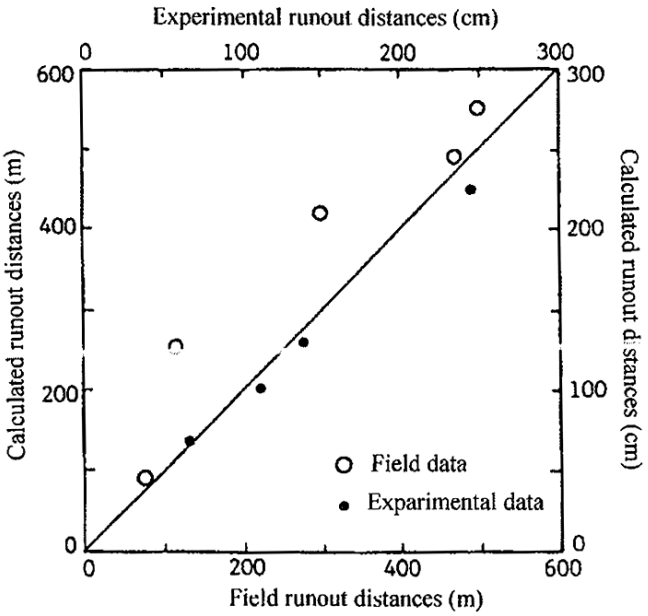

Figure 2-2 Comparison of runout length calculated and observed (Takahashi 2007)

2.3 Past Use of the laboratory apparatus

The small scale flume used for the experimental work presented here has been already adopted for previous studies. Mahoney (2006) used the apparatus to investigate the role of the relative density and the moisture content of an erodible test bed on the erosion and entrainment of debris flow. A number of tests were conducted using a well-graded gravelly sand both for the bed and for the debris flow mass, varying the water content and the void ratio of the test bed material. The main outcome was that by increasing the water content of the bed (i.e. saturation ratio), the debris flow runout increases. Furthermore, the increase of the relative density of the test bed at the same water content led to a larger erosion and entrainment into the debris flow.

Later, Carroll et al (2009) used the same small scale flume with the aim of identifying the most influential parameter, among coefficient of uniformity C_U, fluid viscosity μ, and mean grain size D_{50}, which can be used to achieve dynamic similarity described by the dimensionless numbers introduced by Iverson (1997). Specific debris flow features, such as flow segregation, were achieved at fluid phase viscosities of 1.0 mPa.s and 3.3 mPa.s. However, when the viscosity was increased by nearly two orders of magnitude i.e. to 170 mPa.s, this behaviour was not exhibited. The viscosity was also found to have an influence on the runout behaviour of the mixtures, with runout length decreasing with increasing viscosity. The effect of changing the coefficient of

uniformity C_U within the range of 4.4-6.2 for a particular particle size distribution was also investigated. It was found that irrespective of viscosity, an increased C_U caused an increase in runout length. The trends emerging from this study instigated the experimental research presented here.

2.4 Experimental procedure

2.4.1 Small scale flume

The laboratory experimentation was undertaken in a small-scale flume. A sketch of the experimental apparatus is given in Figure 2-3. The flume measures 3.7m in length by 1m in height and has a metal hopper supporting the debris flow material before its release. The section of the channel containing the straight portion of slope is 1m long by 18cm wide and can be varied from test to test.

The channel floor is artificially roughened by glued fine sand and the outward facing wall is made from Perspex, through which a high-speed digital camera can view the downslope flow behaviour. The camera is a SVSI model (MV-A002-M) with maximum frame rate 500 frames per second (fps) at a resolution of 1,280 x 1,024 pixels. A grid of calibration markers with points spaced 30mm is dotted on the Perspex face to assist in imaging post-processing measurements. The base of the marine plywood runout area, which is sealed but otherwise not roughened, is 0.65 m wide and 2.20 m long and marked with a 50mm grid so that the final runout can be easily depicted and compared between tests.

The material to be tested is, before testing, placed in the tank, located 1.08m above the runout area. The pneumatically-operated hopper trapdoor is linked by a micro-switch to the high speed camera to ensure a coordinated time-delay between the release of the material and the recording of the flow. Two floodlights are used to illuminate the flume in order to achieve the luminosity necessary for the high camera frame rate during the tests. The correct positioning of the floodlights is important to ensure there is no glare in the Perspex window, degrading the image quality produced from the camera. Figure 2-4 shows the set up during the experiments.

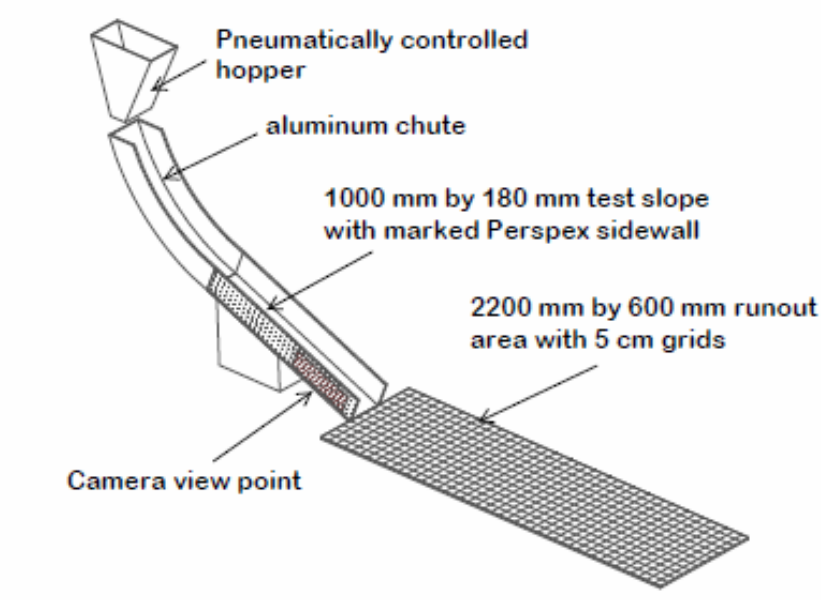

Figure 2-3 Apparatus employed in the tests

Figure 2-4 Set up of the flume during the experiments

2.4.2 Material

Soil used in the test was sourced from the lower Waimakariri River bed, the largest of the North Canterbury rivers in the South Island of New Zealand (see Figure 2-5). It is derived from weathered greywacke bedrock which is eroded by fluvial processes into a rounded to sub-rounded shape. Myles and Parkin (2009) measured the shapes of the particles composing the soil in terms of the sphericity and the roundness of the grains. The sphericity defines the degree to which a particle approximates the shape of a sphere, while the roundness is related to the curvature of the edges and the corners. The Waimakariri material was characterised at four different particle sizes using comparison charts. Samples of 100 particles retained at 9.53mm, 2.56mm, 600μm and 150μm sieves were analysed using the Rittenhouse chart (Rittenhouse, 1943, cited Vallejo, 1995) for estimating the sphericity (See Figure 2-6 Rittenhouse chart for estimation of Roundness (Rittenhouse, 1943 cited Vallejo, 1995) on the right; Krumbein Chart for Estimation of Sphericity (Krumbein, 1941, cited Vallejo, 1995) on the right (see Figure 2-6). The Krumbein chart (Krumbein, 1941, cited Vallejo, 1995) was used for the estimation of roundness (see Figure 2-6). Myles and Parkin found relatively consistent sphericity values across the different particles sizes. In contrast however, the roundness varied significantly with the sizes, exhibiting much higher roundness for the larger particles than for the smaller (see Figure 2-7). The largest can be classified as rounded sub-rounded, as expected in an alluvial material, while the smallest is found to be angular. Some shape characteristics of the used soil are shown in Figure 2-9, Figure 2-10 and Figure 2-11.

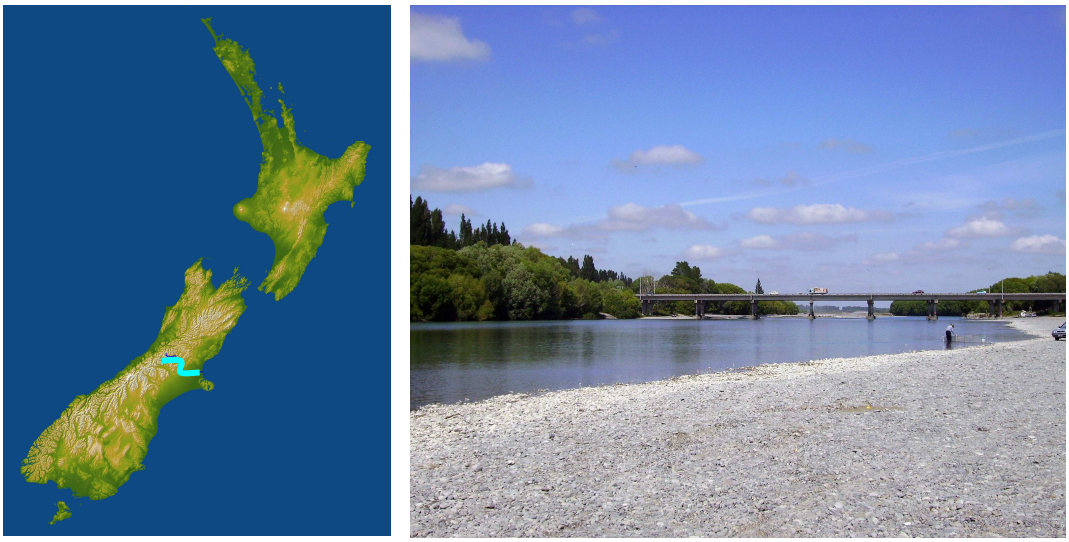

Figure 2-5 Location of the Waimakariri river in New Zealand (left) and photo of the source material collection site (right)

Before the test, artificial particle size distributions were created where C_U and D_{50} were systematically varied (see Chapter 3 for details). Upper and lower bounds on the grading of the selected materials were set according to the size of flume apparatus and the quantity of fines that a mixture can comprise without being affected by significant viscous effects. The largest particle size before the jamming of the solid grains occurs is approximately 1/6th of flow width (Neddermann, 1992). Hence, for a flow of 180mm this leads to a maximum particle size around 30mm. Because the material collected from Waimakariri River contains a wide range of particles size, from 10 cm coarse gravel to fine silt, the particles larger than 38mm were removed by sieving. The quantity of fines in the particle size distribution was set as follows. According to the sediment concentration and the percentage of fine material (i.e. silt and clay), a debris flow can generally be classified as granular or viscous (Coussot and Mernier, 1996).

Since these experiments address tgranular debris flows, the fraction of fine material was limited to 10%. The material smaller than 75μm was indirectly measured by means of a hydrometer test and it was found to be silt without any presence of clay, Figure 2-8.

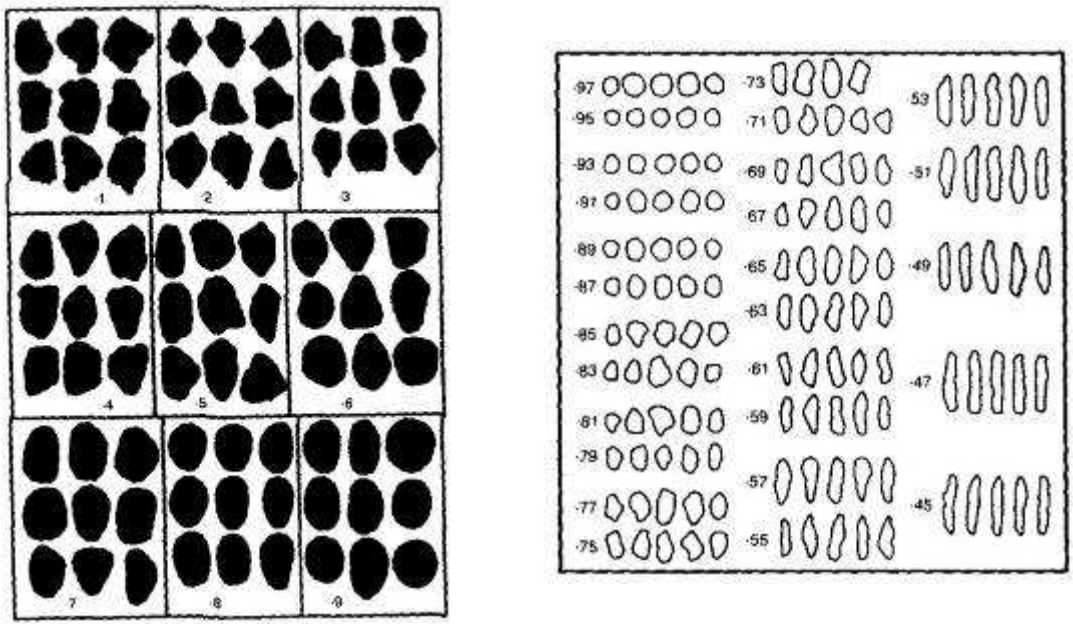

Figure 2-6 Rittenhouse chart for estimation of Roundness (Rittenhouse, 1943 cited Vallejo, 1995) on the right; Krumbein Chart for Estimation of Sphericity (Krumbein, 1941, cited Vallejo, 1995) on the right

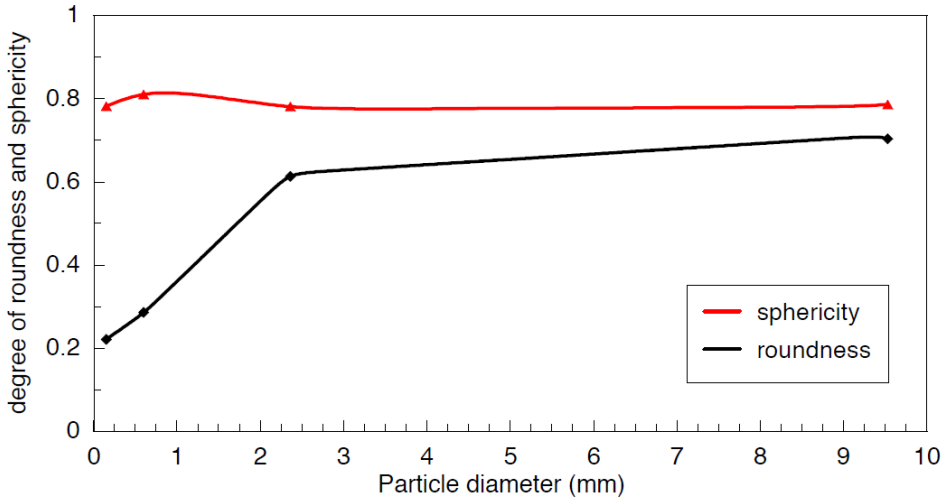

Figure 2-7 Roundness and sphericity of Waimakariri material (from Myles and Perkins, 2009)

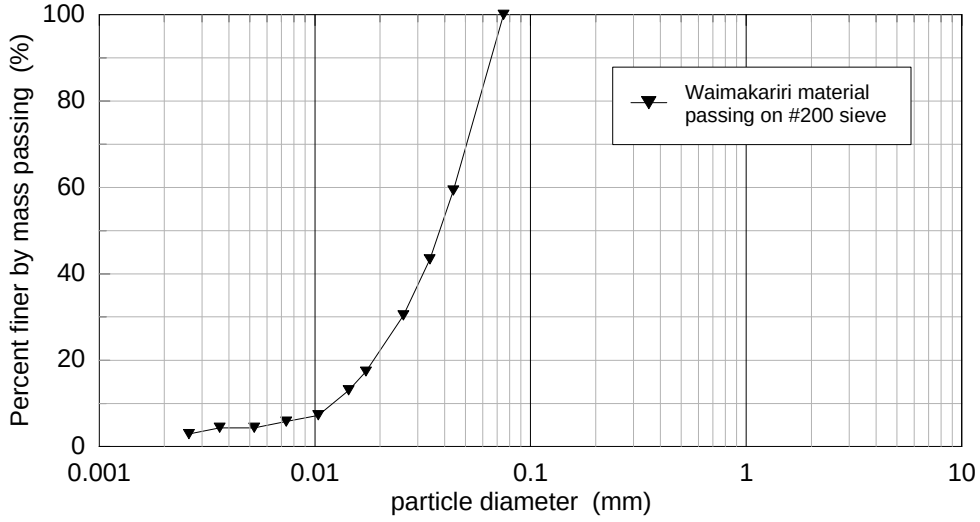

Figure 2-8 Distribution of soil particles for the fraction passing material finer 75 μm

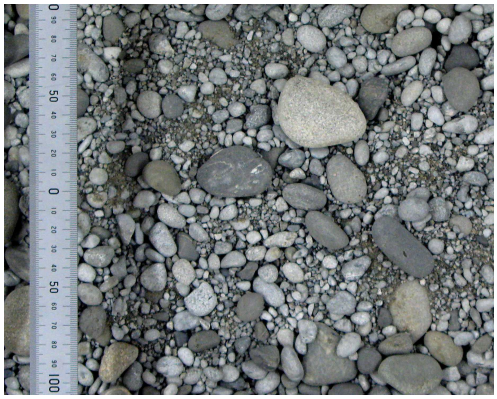

Figure 2-9 Particles from Waimakarari River

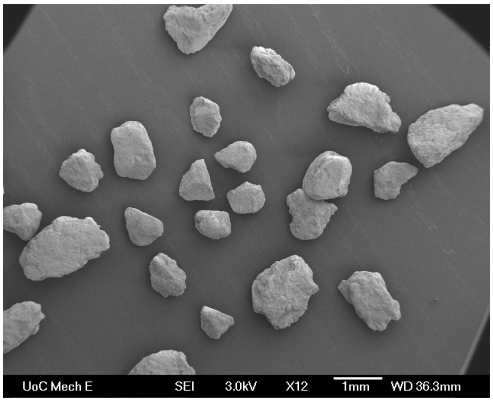

Figure 2-10 SEM image of 150 μm particles at 30X magnification

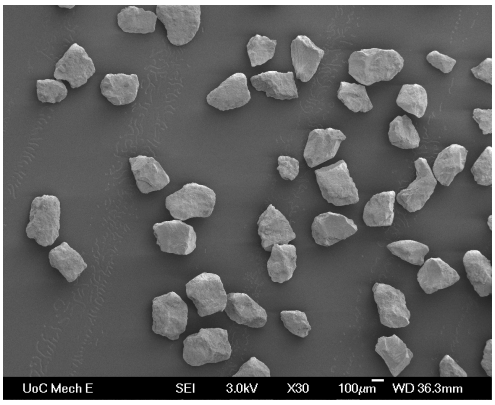

Figure 2-11 SEM image of 600 μm particles at 12X magnification

2.4.3 Test procedure

The mixtures employed in the tests were prepared by mixing 8 kg of particles with 2.24 litres of water at about 20 °C, to achieve a volumetric sediment concentration of 0.57 and a moisture content of 28%. The water was added slowly and the mixture manually stirred to ensure a full mixing and fluidisation of the material. Then, the mixture was placed in the tank at the head of the flume, where manual stirring of the material was continued to ensure that the least possible segregation and consolidation took place before its release. This well-mixed state of the mixture inside the tank, though it is not similar to that of a natural debris flow at the initial stage of its development, allows the material to mimic the behaviour of debris flows at the distal reach of the channels before the deposition in an unconfined fan.

The slope angle of the flume was kept constant at 24° for all the tests. The pneumatically operated trapdoor was linked by a micro-switch to the camera to ensure a delay in recording of 0.25s. The high-speed camera recording was at a frame rate of 800fps with an image resolution of 1280x512 pixels. The camera was set to capture images of the flow at the terminal section of the straight portion of the flume, immediately before the exit to the runout area.

2.4.4 Deposit mapping, sampling and analysis of the camera images

After each test, measurements of the runout and of the width of the deposit at 10%, 50%, and 80% of the runout length were taken by means of a ruler tape. In addition, using a Vernier calliper, the depth of the deposit at a number of points on the runout fan were measured. Samples were collected from the deposit material at two locations: the frontal lobe (lobate sample) and the centre of the deposit (centre sample). In some of the tests, deposition of the material occurred also in the flume. In these cases, one more sample was collected from that position. Finally, the specimens were dried and then sieved to determine the particle size distribution of the deposit at each position. This, enabled comparison with the original PSD of the mixture to determine the degree of segregation within the flow. Furthermore, a contour of the deposition area was drawn from the photos taken at the end of the tests from the top of the runout area.

The analysis of the high speed camera footages enabled the determination of the dynamic flow characteristics within the flume including the flow velocity and the flow height just before (i.e approximately 15 to 25 cm from the exit point to the deposition area). For each test, the flow-front position was tracked frame by frame. The velocity of the front was estimated, recording the times at which it reached reference dots painted at 3 cm intervals on the Perspex window.

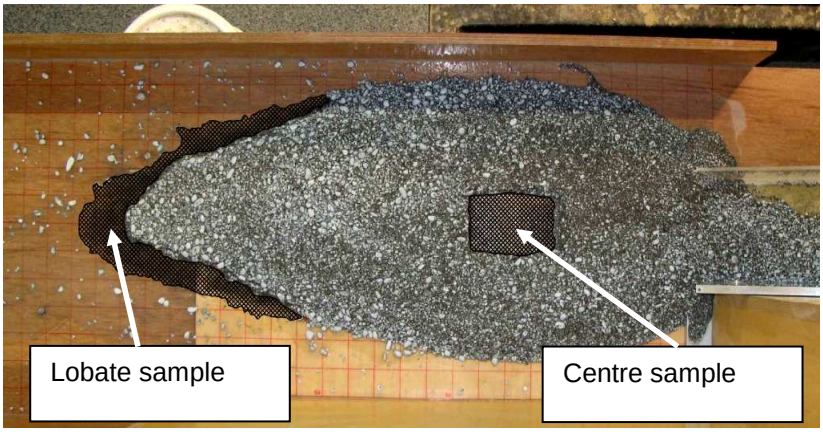

Figure 2-12 Sampling locations

Chapter 3

The role of particle size in the flow behaviour of saturated granular materials

3.1 Introduction

This chapter describes an experimental research on flowing granular materials using a small scale flume apparatus. The objective of the tests is the study of the role of particle size in the mechanics behind these phenomena and its implications on the physical modelling of debris flow. The test procedure and the adopted experimental apparatus are described in the chapter 2. This chapter is organized as follows. In Section 3.2 the test condition are described, in Section 3.3 the results of the tests are presented and discussed. In particular the deposit morphology of the tests is examined in Section 3.3.1 , while in Section 3.3.2 the velocities of the flow are analyzed. Finally in Section 3.4 a summary of the main findings are presented.

3.2 Test conditions

Debris flows are mixtures of granular sediments and fluid, with both components influencing the resulting flow and deposition behaviour. Soils are made of mineral grains. The grain size distribution of a soil, usually characterized by mean particle size D_{50} and coefficient of uniformity C_U, determines the governing particle-level forces, inter-particle packing and the ensuing macroscale behaviour. In soil mechanics, the gradation of a soil is usually described by means of the uniformity coefficient C_U and the coefficient of curvature C_z:

$$C_U = \frac{D_{60}}{D_{10}} \tag{3.1}$$

$$C_Z = \frac{D_{30}^2}{D_{60} \bullet D_{10}} \tag{3.2}$$

Where D_{10}, D_{30} and D_{60} are the diameters for which the 10%, 30% and 60% of the mass of the sample is finer. C_U is related to the shape of the particle size distribution curve. Large C_U means that the size distribution is well-graded. Vice versa, C_U= 1 corresponds to a uniform distribution, all grains being of the same size (see Figure 3-1). Smooth curved soils have coefficients of curvature C_z between 1 and 3, whereas irregular curves have higher or lower values. Soils that are missing a type of soil are called gap-graded (for gap-graded soils, C_Z is usually less than 1 or larger than 3). A soil, to be described as well-graded, must meet certain criteria. According to the Unified Soil Classification System, the coefficient of uniformity, C_U, must be greater than 4 for gravel, and greater than 6 for sand. At the same time, the coefficient of curvature, C_Z, must be between 1 and 3.

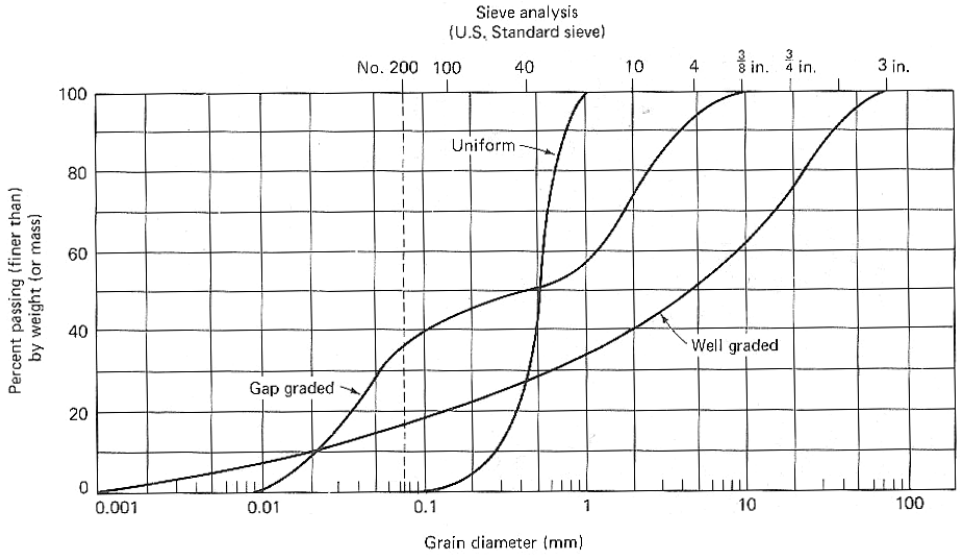

Figure 3-1 Types of grain-size distributions curves

A number of tests using soil with different gradations, i.e. with different C_U, C_Z and D_{50} values, were performed. Table 3-1 reports the experimental conditions of the tests including test gradation name, particle sizes, solid concentration and number of test repeats for each particle size distribution. The particle size distributions were artificially created by mixing fluvial sand and gravel. The characteristics of the material, the details of the test procedure and the experimental apparatus are described in Chapter 2. Figure 3-2 shows a comparative group of well-graded particles size

distributions (PSDs) used to examine the influence of a change in mean particle size D_{50} for C_U=10. The investigated gradation curves encompass soils from medium sand to gravelly sand. Figure 3-3 shows comparative materials to examine the dependency from the C_U at values of D_{50} of 0.52mm, 1.76mm and 3.78mm. At each D_{50}, a number of grain distributions, ranging from uniform to well-graded materials, were analysed.

Table 3-1 Summary of the test conditions

Particle Size Distribution	C_U	C_Z	D_{90} (mm)	D_{50} (mm)	D_{10} (mm)	Number of tests	volumetric sediment concentration
PSD9	21	1.1	11.88	1.76	0.135	4	0.57
PSD10	10	1.1	14.50	3.78	0.538	3	0.57
PSD11	10	1.1	7.13	1.76	0.257	3	0.57
PSD12	10	1.1	3.77	0.953	0.136	3	0.57
PSD13	6.4	0.7	7.13	1.76	0.401	3	0.57
PSD14	10	1.1	2.13	0.520	0.075	3	0.57
PSD15	4.8	1.0	1.63	0.519	0.139	2	0.57
PSD16	3.3	0.9	4.35	1.76	0.660	2	0.57
PSD17	3.3.	1.1	1.34	0.520	0.193	2	0.57
PSD18	6.4	1.1	12.11	3.78	0.767	2	0.57
PSD19	14.6	1.0	16.25	3.78	0.387	3	0.57
PSD20	3.3	1.0	8.76	3.78	1.400	2	0.57

D_{10} and D_{50}, effective and mean grain size; D_{90}, particle size for which 90% of the particles are finer; C_z, coefficient of curvature; C_U, coefficient of uniformity

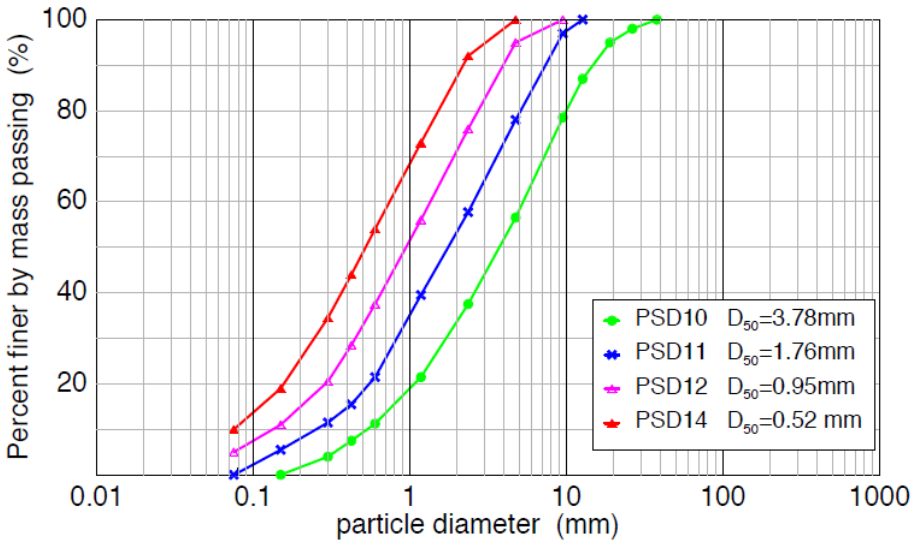

Figure 3-2 Particle size distributions for tests with same C_U=10

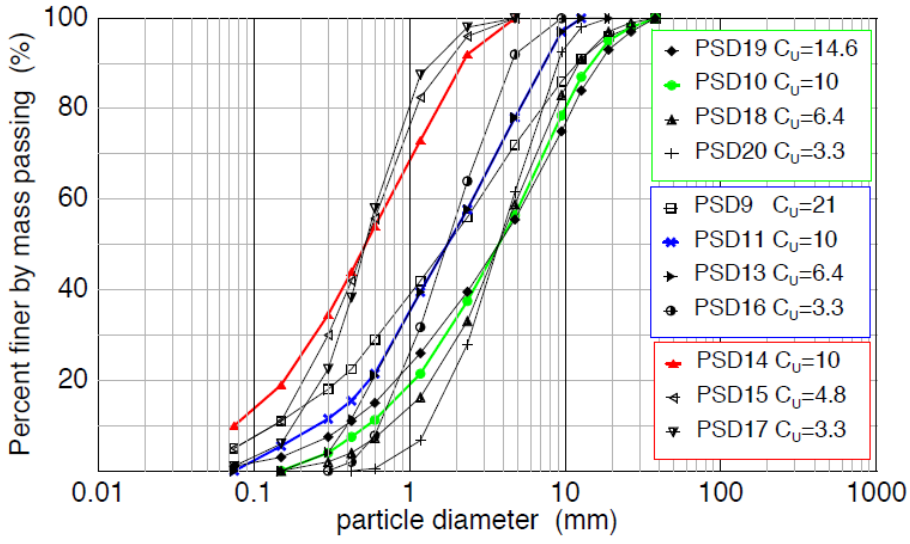

Figure 3-3 Particle size distributions for tests with different C_U at particular values of D_{50}

3.3 Results

3.3.1 Deposit morphology

Figure 3-4 shows the resulting shape of the runout fans on the deposition area, for tests with different C_U at given values of D_{50}. The largest runout lengths are found for PSDs with the highest values of C_U – i.e. for well-graded materials. These tests display also the greatest overall segregation during flow and deposition (Figure 3-5; Figure 3-6; Figure 3-7; Figure 3-8; Figure 3-9), with coarser particles being shunted to the deposit margin, while the deposits appear the most uniform in terms of plan area distribution. As the soil becomes more uniformly graded, the deposits for the finer PSDs (i.e. with D_{50} of 0.52mm and 1.76mm) become progressively more pear-shaped with an extended deposit area at the proximal end of the deposit. For coarse PSDs the deposit become more circular shaped. In general, a lower runout is observed for tests with lower C_U, for a given mean particle size D_{50}, as shown in Figure 3-10. The reason for this may be that, in a closed solid-fluid system, the segregation of particles and fluid within a flow comprised of well-graded materials may assist in generating low frictional resistance within the flow body (i.e. where fine particles and fluid dominate, permeability is reduced and pore pressures may be greater than hydrostatic (Iverson, 1997) to the extent that liquefaction occurs and effective stress reduces to zero), while not contributing as much to increased friction at the flow margins (where coarse particles dominate with increased permeability and reduced fluid pressures) during runout over a flat surface. It is well-understood that, during deposition, the interior of flows tends to shunt forward and sideways the coarser frontal fraction (Major and Iverson 1999) which forms levees confining the still-liquefied core, post-arrest. On the other hand, in a uniformly-graded flow, no segregation can occur, so the whole body of solids and fluid maintains a uniform steady frictional resistance throughout. During the runout, momentum is lost more rapidly, since the fluid is more evenly distributed, resulting in a shorter stoppage distance as fluid pressures drop and interparticle contact forces are regained.

The D_{50} is also found to have an influence on the runout length. Figure 3-11 shows the effect of varying D_{50} of the flow at fixed values of C_U. The runout length reduces as D_{50} increases for the well-graded PSD (C_U=10 and C_U=6.4), with a more evident effect for high values of C_U. This behaviour is related to the permeability of the mixture. As the grain size increases, the same happens for the permeability. Consequently, the drainage time of the fluid from the mixture decreases. The overall result is an increase in the Coulomb friction within the flow and at the flow margins, resulting in a shorter runout.

Considering the well-graded mixture with C_U=10, a maximum limit of the runout distance appears to occur. This is obtained with a decreasing particle size, so that PSD12 and PSD14, with D_{50} of 0.95mm and 0.52mm, respectively, give similar runout lengths. This may be due to the "grain settling" limit, as suggested by (Iverson 1997). Iverson stated that a grain of diameter δ may be considered as part of the solid phase of a debris flow if the duration t_D of the debris flow is long in comparison to the timescale for the settling of the grain. The timescale for settling can be estimated dividing the half thickness, h/2, of a debris flow by the grain settling velocity v_{set}, estimated from Stokes' law or from a more general equation that accounts for grain inertia (Vanoni,1975). Therefore, the debris flow duration is larger than the timescale for settling, if the following condition holds:

$$h/2t_D\, v_{set} < 1$$

Typical values of t_D for debris flows in the field, range from 10s for small debris flows to 10^4s for the largest, while h/2 ranges from 0.01m for small events, to 10m for the larger ones. Hence $h/2t_D \sim 0.001$m/s implies a velocity v_{set}<0.001m/s for grains to act as a part of fluid. Settling velocities of this magnitude or less in water, require grains finer than sand, i.e. <50μm (Vanoni, 1975). Such particles are not considered by Iverson as being part of the solid phase, but rather, they serve to increase the fluid viscosity. Accordingly, he considers particles smaller than the silt-sand boundary as belonging to the fluid phase in his 2-part stress partitioning model.

The results show that the onset of viscous effects is occurring at a D_{50} of 500μm and a D_{10} of 75μm for tests with PSD14. The duration of these experiments is around 0.7s. The thickness of the flows is approximately 20mm. Following the consideration by Iverson, the critical grain size, calculated using the Stokes' law, is found to be about 0.125μm, corresponding to around the D_{15} of the PSD. This suggests that, while D_{50} is often used to characterize debris flows (Iverson 1997; Takahashi 1991), other representative diameters may play a more meaningful role in terms of mechanical-hydraulic behaviour. This is also confirmed, for instance, by Hazen (1892), who showed that D_{10} controls the seepage behaviour of uniform soils, so that a slightly larger diameter D_{15} or D_{20} can be considered more appropriate for well-graded materials.

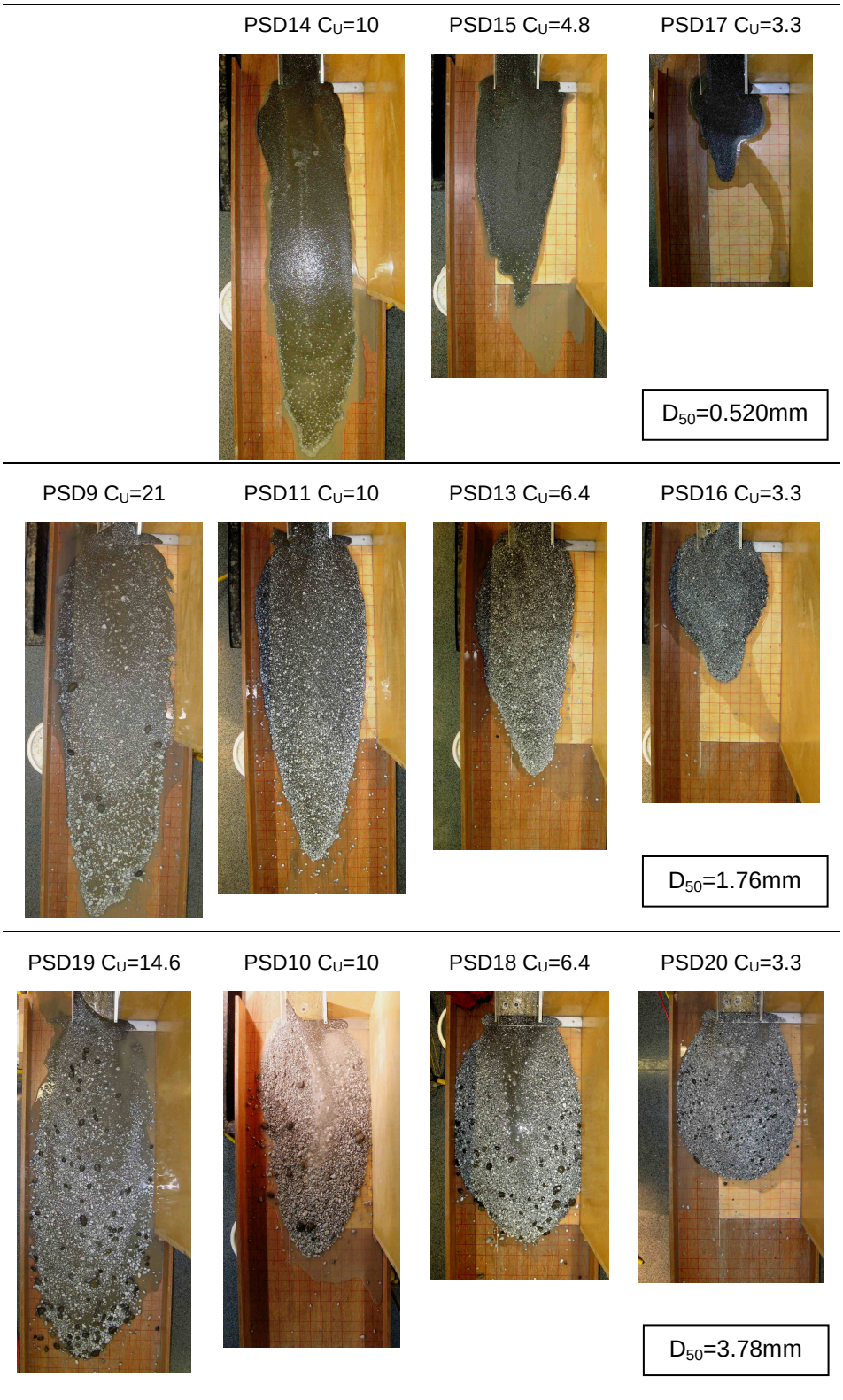

Figure 3-4 Typical deposits for PSDs with different C_U at particular values of D_{50}

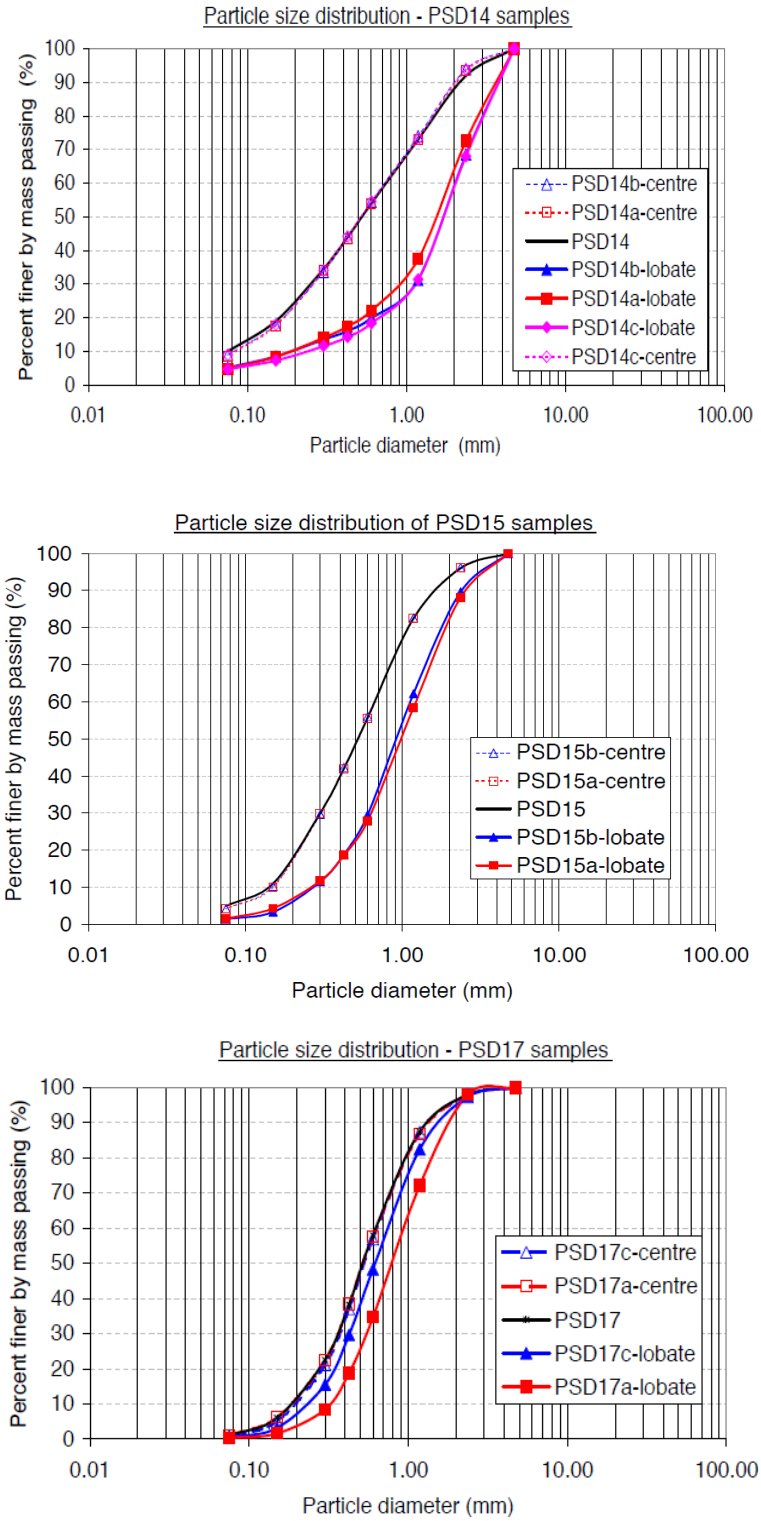

Figure 3-5 Particle size distributions of the samples collected from the deposition area of PSDs14, PSDs15, PSDs17

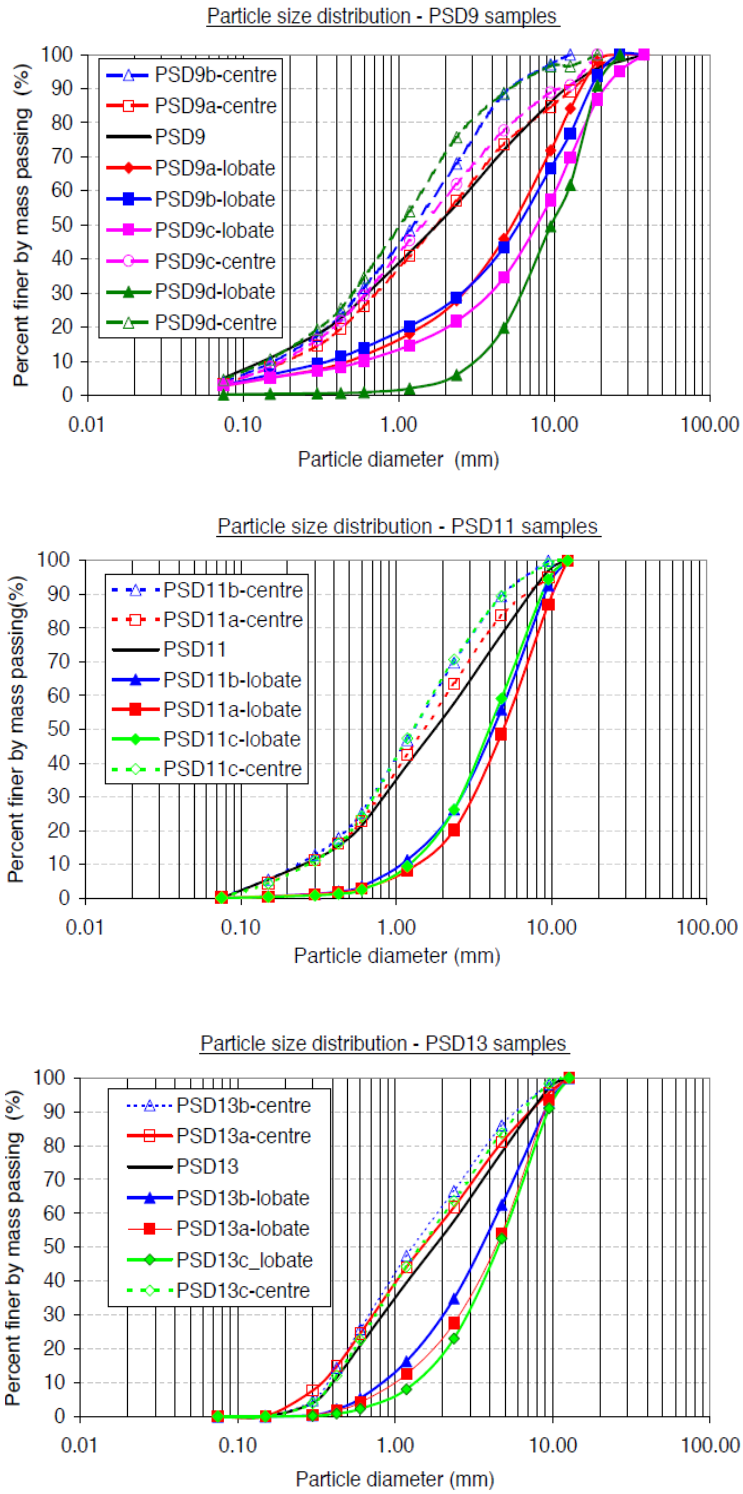

Figure 3-6 Particle size distributions of the samples collected from the deposition area of PSDs9, PSDs11, PSDs13

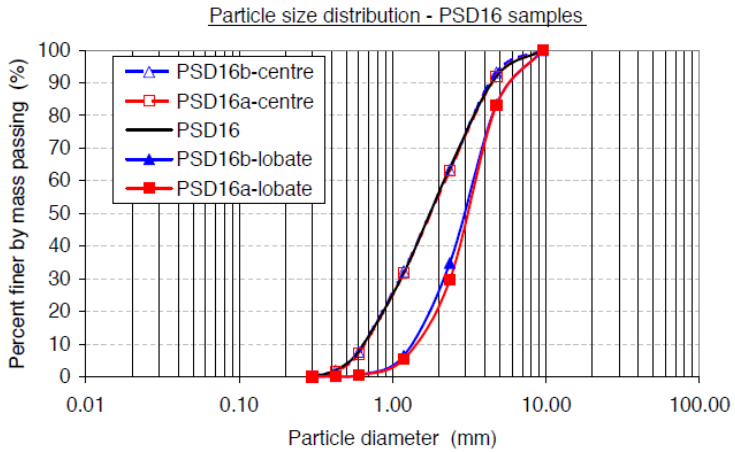

Figure 3-7 Particle size distributions of the samples collected from the deposition area of PSDs16

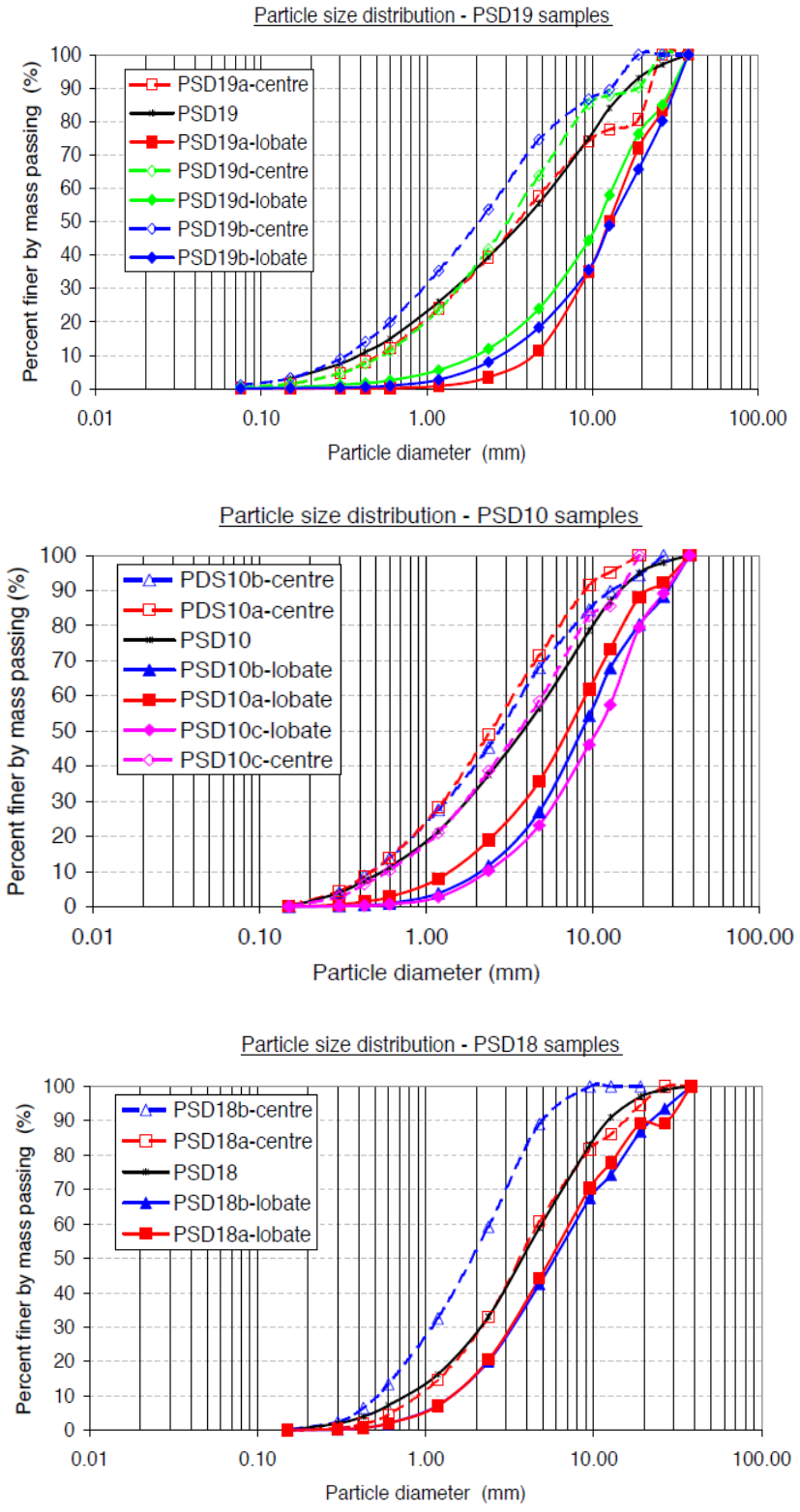

Figure 3-8 Particle size distributions of the samples collected from the deposition area of PSDs19, PSDs10, PSDs18

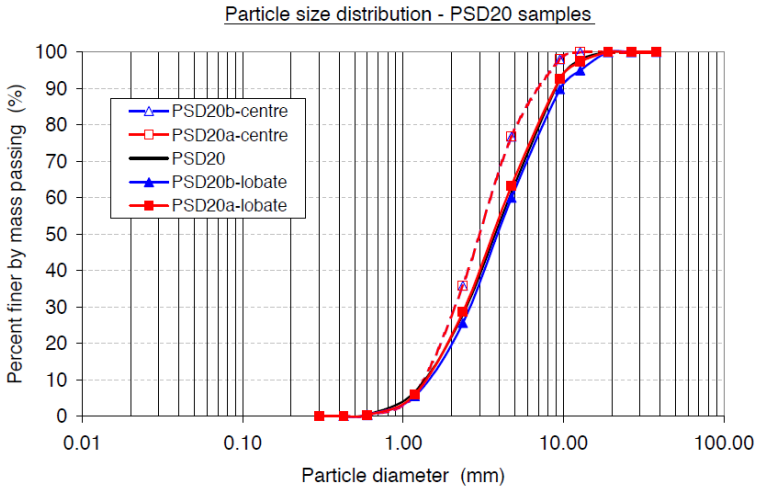

Figure 3-9 Particle size distributions of the samples collected from the deposition area of PSDs20

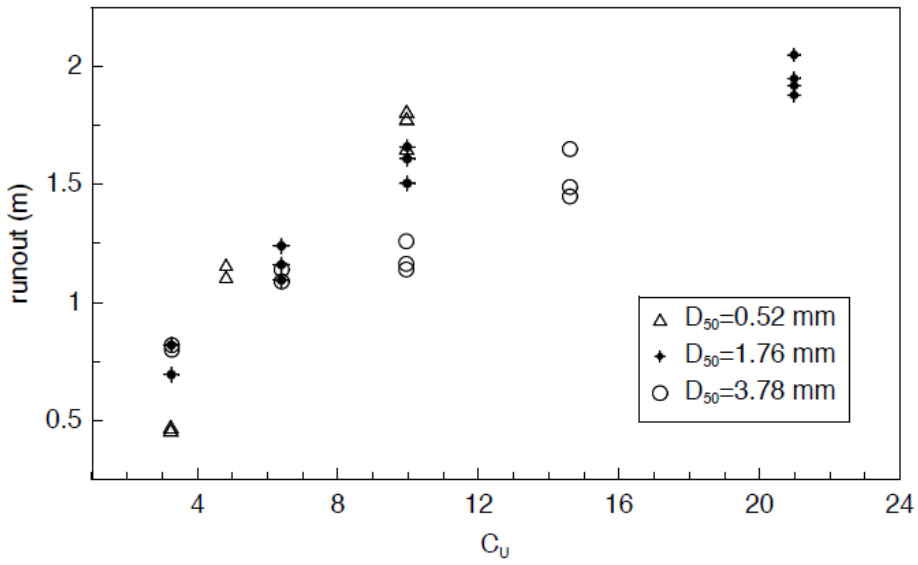

Figure 3-10 Runout against C_U for tests with same D_{50}

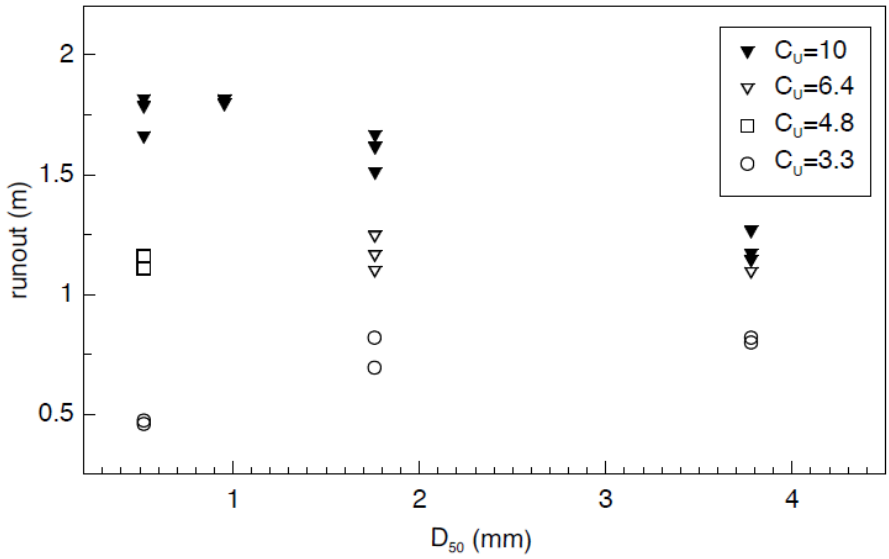

Figure 3-11 Runout against D_{50} for tests with same C_U

Figure 3-11 shows also that for tests where D_{50}> ~1.7mm, D_{50} does not appear to affect the runout for the uniform material (C_U=3.3) since both the PSDs with D_{50}=1.76mm and D_{50}=3.78 exhibit approximately the same runout distance. As mentioned before, in flow with uniform PSD, segregation does not occur (or occurs mildly), resulting in a rather homogeneous distribution of the fluid within the whole body. This may lead to a uniform resistance frictional resistance through the flow during the motion and a fast dissipation of the momentum during the deposition, since there is no part of the body in which the flow is significantly more saturated (and mobile).

In terms of the runout, an anomalous behaviour is exhibited by the finest uniform PSD with D_{50}=0.520. Tests with such PSDs are characterized by a runout significantly shorter than those observed for the other two uniform materials. This may be explained by the development of a relevant level of suction at the unsaturated front of the experimental flow. It reasonable to assume that a flow comprising material with C_U=3.3 can reach a certain degree of segregation, although very low (see Figure 3-5). This leads to an accumulation of the coarsest particles at the front, where the material can be assumed to be unsaturated, whereas the debris mass behind is saturated. The frictional resistance acting at the flow margins is expected to control the mobility of debris flows (Majo&Iversonr, 1999). For this particular PSD, comprised of relatively fine material, the shear strength of the unsaturated soil at the front can be strongly affected by the development of pore water suction U_e (i.e. the negative pore water pressure measured relative to ambient atmospheric pressure). A rough estimate of the suction at the front of the surge can be obtained considering the equilibrium of a hemispherical water meniscus in a circular pore of diameter d, as shown in Figure 3-12:

$$\pi dT = \left(\pi d^2 / 4\right) U_e \tag{3.3}$$

where the left term of the equation represents the force due to surface tension around the rim of the meniscus, while the right term is the force due to the difference in pressure between the pore water and the air. T is the surface tension of the water/air interface (=7.197x10^{-5} kN/m at 25°C). In the case of the soil at the front of the experimental flow, the diameter d represents the pore size that governs the overall permeability of the material. While for uniform soils, the D_{10} particle size is generally adopted (Hazen, 1892), for a well-graded material a more proper diameter, which takes into account the wide gradation of the particle size distribution, should be chosen. Here we calculate an effective diameter D_{eff} as suggested by Carrier (2003) for the assessment of the permeability of a soil by means of the semi empirical formula by Kozeny-Carman:

$$D_{eff} = \frac{100\%}{\sum\left(f_i / D_{ave_i}\right)} \tag{3.4}$$

where f_i is the fraction of particles between two sieve sizes and D_{avei} is the average particle size between two sieve sizes (larger [l] and smaller [s]) calculated as

$$D_{ave_i} = D_{li}^{0.5} \bullet D_{si}^{0.5} \tag{3.5}$$

The average flow thickness in the experimental flows is around 20-30mm so that if we assume no pore pressure at the front, in case of no suction, the net stress at the base is approximately 0.4kPa (assuming for the calculation an unit weight equal to 16kN and an average thickness of 25mm). Substituting in equation (3.3) the D_{eff} (= 0.349mm) for the finest uniform particle size distribution (D_{eff} = 0.349mm), PSD17, the pore water suction (negative stress) at the front is found to be around 0.82kPa.

Therefore, the total net normal stress and hence the shear resistance to the flow, increases significantly due to the relatively high contribution to the effective stress given by the suction – i.e. giving a net effective stress of 0.4 (total) + 0.8 (suction) = 1.2kPa. The frictional resistance to the flow at the base is proportional to this value, assuming Coulomb friction and Terzaghi's principle of effective stress are valid.

For comparison, the pore water suction that develops at the front of the experimental flow surge of the test with the uniform PSD (PSD16 with C_U=3.3 and D_{50}=1.76mm), and which displays a longer runout is calculated to be around 0.21kPa – using D_{eff} =1.34mm This represents a much smaller contribution to the total net normal stress at the base of the flow and it is more than three time less than that developed with D_{50}=0.52mm. In terms of its contribution to effective stress, it leads to an approximate net effective stress of 0.4 (total) + 0.2 (suction) = 0.6kPa. Larger D_{50} will lead to even lower suction stresses, so that eventually suction can be ignored completely. Hence the basal flow resistance for PSD17 will be twice that developed for PSD16 and three times that of flows with even larger D_{50} (assuming the same flow thickness). This can explain the short runout of these tests with low D_{50} in comparison to the other PSDs with same, uniform, C_U.

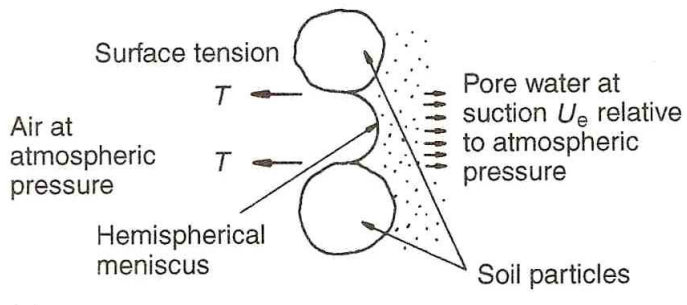

Figure 3-12 Forces acting on the water meniscus between soil particles (Powrie, 2004)

3.3.2 Velocity relationships

Figure 3-13 shows a plot of the runout length against the square of the front velocity of the flow for tests of the well-graded mixture with the same C_U=10 but at two different mean particle sizes, D_{50}=1.76mm and D_{50}=3.78mm (Figure 3-13). A linear relationship is found. The influence of D_{50} is clear, so that as the particle size increases, the velocity decreases. The same does the runout. This effect is related to mixture permeability, such that, as the grain size increases, so does the permeability. Hence the drainage time of the fluid from the mixture decreases. The overall result is an increase in Coulomb friction between the particles and at the flow margins, resulting in a lower velocity being attained during downward motion on the slope and a shorter momentum-driven runout. The linear relationship between the runout and the square of the velocity is in agreement with the Takahashi's dynamic model (see Chapter 2). That is:

$$X_T = f\left(v_u^2\right) \tag{3.6}$$

where X_T is the runout distance and v_u the upstream debris velocity.

Figure 3-14 shows a plot of the runout length against the square of the front velocity for tests where C_U is varied at a given D_{50}. It is found that, for the PSD at D_{50}=1.76mm, the velocity and the runout increase together with the C_U. In this case, the relationship appears to depart from linearity. That is, as C_U increases, the square of the velocity increases at a lower rate than the runout. However, the scattering of the velocity values makes it difficult to draw a clear conclusion about this dependency and further investigation is needed.

For the coarsest PSDs, i.e. at D_{50}=3.78mm, the increase of the runout with the square of the front velocity, seems to follow a linear relationship for the well graded distributions (C_U>6.4) with a growth of both the runout and square velocity with C_U. However, a peculiar result is represented by the most uniform of these PSDs, which exhibits a very short runout but a square velocity that is relatively high. Such short runout can be expected due to the high permeability of this mixture that increases the friction between the particles and at the flow margins. However, the value of the front velocity is surprisingly high in comparison not only with those at the same D_{50} but also with the other tests. This result perhaps highlights the difficulties in ascribing a particular velocity value to a flow test, and again, further work may be needed to check this result,

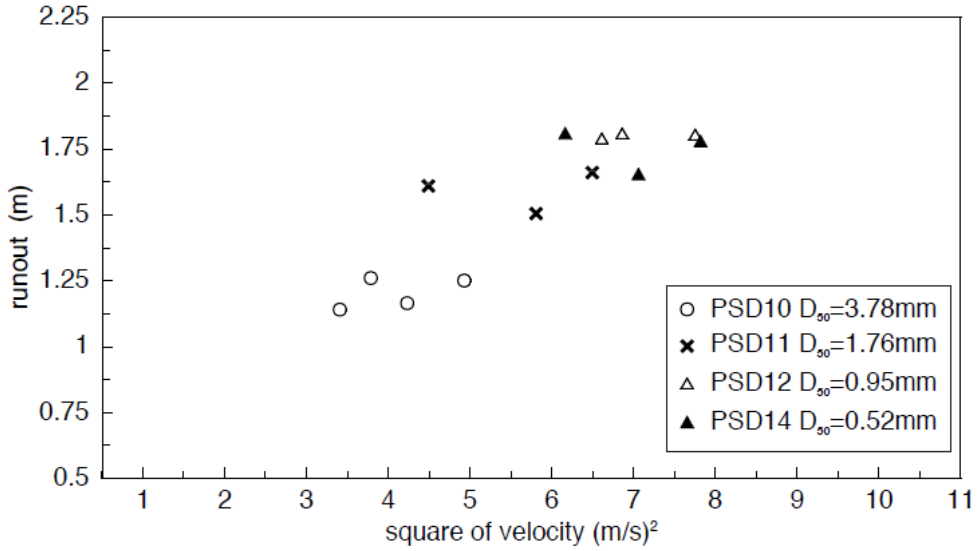

Figure 3-13 Runout against square value of front velocity for well-graded PSDs with C_U=10.

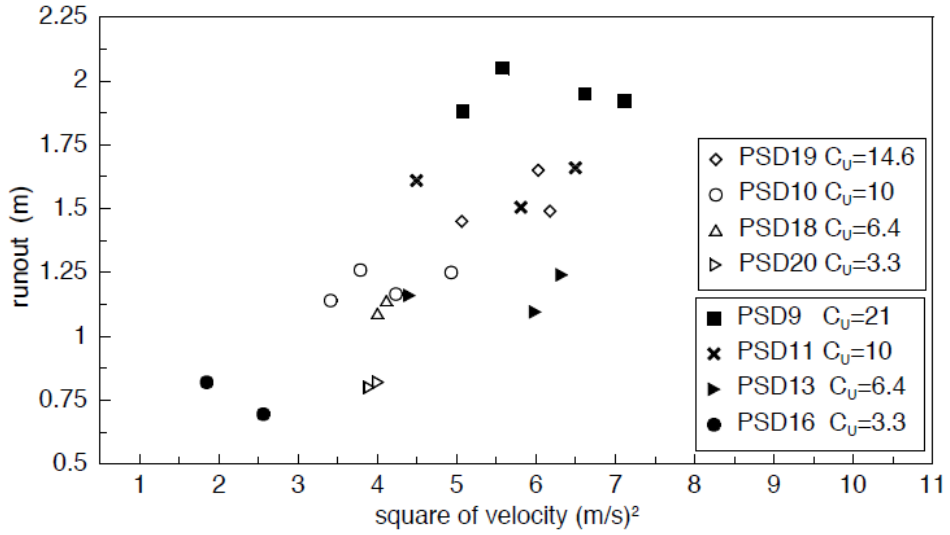

Figure 3-14 Runout against square value of front velocity for PSDs at D_{50}=1.76mm (black dots) and D_{50}=3.78mm (clear dots)

Figure 3-15 shows compares the runout lengths considering all the flume experiments (except those with PSD15, PSD16 and PSD17) calculated using the Takahashi's dynamic model to those observed. Equation (2.1), (2.2) and (2.4) have been used adopting the following values:

θ_u= entrance slope angle=24°

θ= runout slope angle=0°

v_u= front velocity calculated 15 to 25 cm before the exit point to deposition area

h_u= measured debris flow depth at the front

ρ_m = apparent density of fluid=1000 kg/m_3

ρ_s=density of the particles = 2650 kg/m^3

C_s = volume concentration of the solid in flow (assumed constant) = 0.57

α_i = dynamic friction angle for the particles = 31° (for well-graded cohesionless material α_i is around 30° (Hungr, 1981))

The result shows that irrespective of the C_U and D_{50}, the Takahashi model approximately matches the experimental evidence. The scattering of the data may be explained by the simplified assumptions at the base of the model that neglect the complex mechanisms involved in transfer and dissipation of momentum during motion and deposition of granular flows. Probably the scattering is also due to the uncertainties associated with the procedure adopted to measure the velocities (see Section 2.2.4).

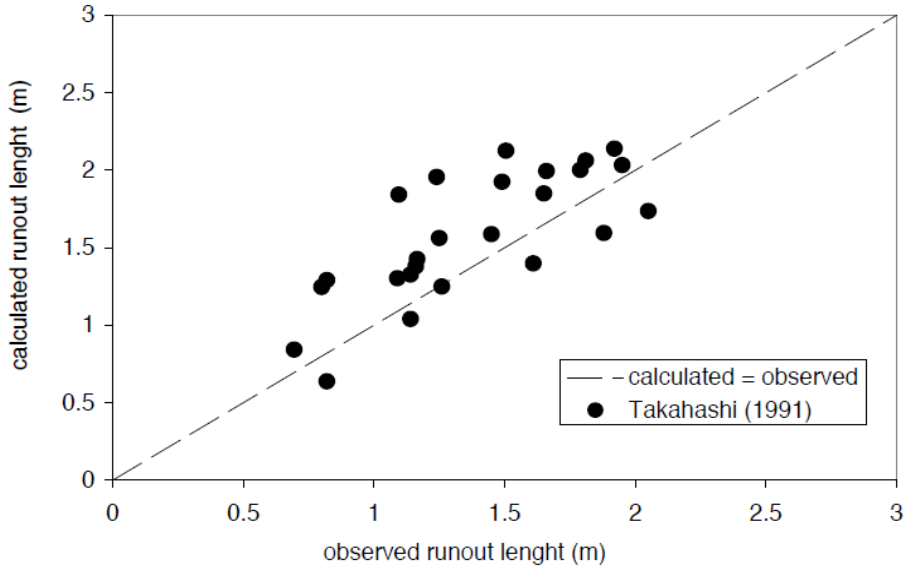

Figure 3-15 Comparison between the observed runout lengths and those calculated with Takahashi model

3.4 Conclusions

The experimental research presented in this chapter shows that the particle size distribution has a significant effect on the mobility of flowing granular materials at a given moisture content and for a given mass of solids. Segregation of particle sizes occurring during the flow motion of well-graded materials, results in a relatively fine-grained flow rear that is maintained in a liquefied state with a coarser-grained flow front and exterior that acts to contain and define the flow margins. Such interplay results in flows with somewhat greater speed and larger average runout for well-graded soils in comparison to uniform graded soils. The mean particle size is also found to have an influence on mobility of well-graded materials, with flows comprising of larger particles producing less mobile flows due to increasing permeability and particle friction. However, D_{50} appears have little influence on the runout of uniform materials.

In addition, for flows comprised of particles smaller than medium-fine sand, viscous effects in well-graded mixtures may lead to a reduction of flow mobility with decreasing particle size, which causes the increase in runout with decrease in particle size to reach a limit. The effect of suction, due to surface tension effects, within the unsaturated front surge in flows comprised of uniform materials may be the reason for their shortened runout at low mean particle size.

The velocities of the flow fronts have been analyzed in order to verify possible dependencies on this variable for the runout and hence on the particle size distribution (i.e. C_U and D_{50}). The results show that the runout lengths generally increase with the square velocity of the front but a well defined relationship is difficult to establish. In same cases dry saltating particles precede the arrival of the main surge. Moreover the images are taken only from the side of the flume. The combination of these factors makes a precise location of the front and of the associated velocity difficult to achieve. Top view images could help to improve these kinds of measurements as confirmed from several preliminary tests accomplished with the high-speed camera placed above the flume.

The results reported here show that careful laboratory testing can inform the mechanisms behind debris flow behaviour observed in the field (e.g. high mobility), however, the materials have to be carefully selected in terms of gradation and particle size in order to reproduce major aspects of their behaviour such as segregation.

Chapter 4

Optical investigations through a flowing saturated granular material

4.1 Introduction

This chapter describes the setup of an experimental apparatus for the non-invasive optical investigation of the internal behaviour of a highly concentrated particle-fluid system in the context of high speed movement.

The method exploits the planar laser-induced fluorescence (PLIF) technique in combination with a system comprised of transparent solids and liquids with matched refractive indices. The PLIF methodology uses a fluorescent substance, in solution with the fluid phase, which is excited by a planar laser sheet. The light absorbed by the substance is re-emitted making the internal structure of the medium become visible. 2D images of the internal behaviour of the flow can be obtained by a high speed camera with its optical axis perpendicular to the laser sheet. The effectiveness of the employed technique relies on a proper combination of solids, liquids and fluorescent substance and on suitable imaging devices and laser light sources.

An overview of the background concepts behind the methodology is given in Section 4.2. Then Section 4.3 describes the general arrangement and the technical specifications of the optical devices used in this work. Section 4.4 presents the physical and optical properties of the adopted solid, fluid and dye, how particle sizes are set and finally, the methodology by which the particles are produced. The description of the flume apparatus used for the tests is given in Section 4.5. The preliminary tests necessary for the tuning of the experimental apparatus, of the materials and of the

optical devices are presented in Section 4.7. The last section describes the test procedure of the experiments whose results will be proposed in Chapter 6.

4.2 Visualisation technique: background

The optical method adopted relies on refractive index-matched transparent materials and the planar-laser induced fluorescence technique. The descriptions of the different aspects involved in these approaches are reported in the following sections.

4.2.1 Requirements for transparency

In optics, transparency is the physical property of allowing light to pass through a material. The opposite property is opacity. When a beam of light encounters a boundary surface separating two different materials, it can interact with it in different ways depending on the nature of the materials and the characteristics of the light (its wavelength, frequency, energy, etc.). The light can interact with an object by some combination of reflection, and transmittance with refraction. Optically transparent materials, such as glass and clean water, allow most of the light to be transmitted (i.e. it enters through the boundary) while a little light is reflected with a change in direction of the light due to a change in the velocity going from one medium into another. Materials, which do not allow the transmission of light, are called opaque. Many substances are selective in their absorption of white light frequencies. They absorb certain portions of the visible spectrum while reflecting others. The frequencies of the spectrum that are not absorbed are either reflected back or transmitted for our physical observation. This is what gives rise to color.

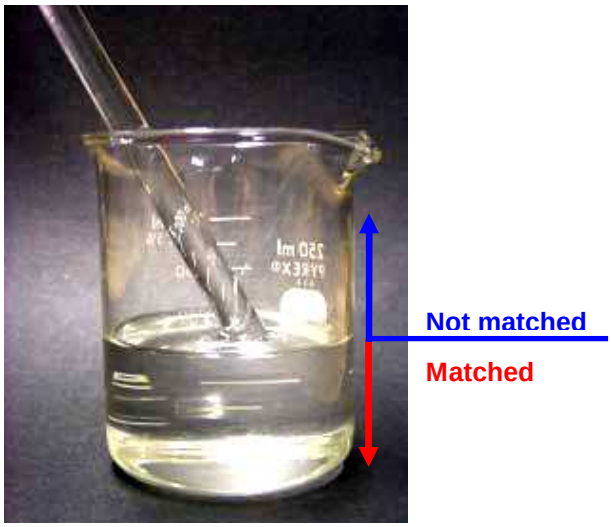

Figure 4-1 Example of refractive-index matching materials (the rod is resting on the bottom of the beaker)

The refractive index of a medium is defined as the ratio of the velocity of light through a vacuum to the velocity of light through the medium. It is also the ratio of the sine of the angle of incidence of a beam of light entering the medium to the sine of the angle of refraction. Optical transparency of solid-liquid systems can be achieved by matching the refractive indices of their constituents. An example is in Figure 4-1, of a glass rod refractively matched with the fluid in which it rests – it therefore appears transparent below the liquid line. This approach should, in theory, render the mixture completely transparent but in practice a number of different factors limits the maximum depth to which it is possible penetrate the mixture. First, entrapped air within the solid-fluid mixture represents one of the major sources of transparency degradation. The air in the form of fine bubbles can act as micro lenses inside the system so that the light that passes through would be mostly refracted and a little reflected making the bubbles translucent or partially transparent. Furthermore, complete transparency is not easy to achieve – it depends on perfect matching of the refractive indices of the fluid and solid phase, which will in turn depend on variations of the refractive index of the liquid with temperature and on the absence of impurities.

4.2.2 Fluorescence

The British scientist Sir George Stokes first described the phenomenon of fluorescence in the middle of the nineteenth century. In 1852, he was responsible for coining the term "fluorescence" when he observed that the mineral fluorspar emitted red light upon illumination with ultraviolet excitation. In fact, when any population of fluorochrome molecules is excited by light of an appropriate wavelength, fluorescent light is emitted. Using a scanning instrument, the light intensity can be measured in detail. Fluorochromes have characteristic light absorption and emission spectra. During excitation, the absorption of light energy boosts an electron in the fluorochrome molecule to a higher energy shell that is an unstable, excited state. During the brief time of the excited state, the excited electron generally decays toward the lowest vibrational energy level within the electronic excited state. The energy lost in this decay is dissipated as heat. When the electron falls from the excited state to the ground state, light of a specific wavelength is emitted. The energy of an emitted photon equals the difference between the energy of the electron in the two states (excited and ground state). That energy difference determines the wavelength ($\lambda_e = h_c/E_{em}$, where h_c is the Planck constant and E_{em} is the energy of a photon of wavelength λ_e) of the emitted light as shown in Figure 4-2. The emission spectrum of the fluorochrome is always shifted toward longer wavelengths (lower energy) compared to the absorption spectrum. This shift makes it possible to separate excitation light from emission light with the use of optical filters. The difference in wavelength between the apex of the absorption and emission spectra of a fluorochrome is called the Stokes shift. Following a pulse excitation of a population of fluorochrome

molecules, fluorescent emissions start instantaneously and decay quickly. For the fluorochromes commonly used the half-life of the excited state and, therefore, of the emissions are typically a few nanoseconds.

The brightness of a fluorochrome (i.e. the intensity of the light that can be emitted) depends on two properties of the fluorochrome:

- The ease with which the fluorochrome absorbs the excitation light (extinction coefficient)
- The efficiency with which it converts the adsorbed light into emitted fluorescent light (quantum efficiency)

So that:

$$Brightness \propto \varepsilon\phi$$

where ϕ, the quantum yield, is the ratio of the number of photons emitted compared to the number of photons absorbed (usually the yield is between 0.1 and 0.9) and the extinction coefficient ε, is the amount of a given wavelength that is absorbed by the fluorochrome.

In addition, the intensity of the emitted fluorescent light is not just a function of the brightness of a fluorochrome but depends also on of the intensity and wavelength of the incident light and the amount of fluorochrome present. The more intense is the light used to illuminate a sample, the more fluorochrome molecules are excited, and therefore the number of emitted photons is increased. When the light wavelength and intensity are held constant, as it happens when using a laser light source, the number of photons emitted is proportional to the number of fluorochrome molecules present. Furthermore, the localized environment surrounding the fluorochrome plays a major role in determining the characteristics of fluorescence emission. Variables such as solvent viscosity, ionic concentration, pH, and hydrophobicity in the environment can have profound effects on both the fluorescence intensity and the lifetime of the excited state.

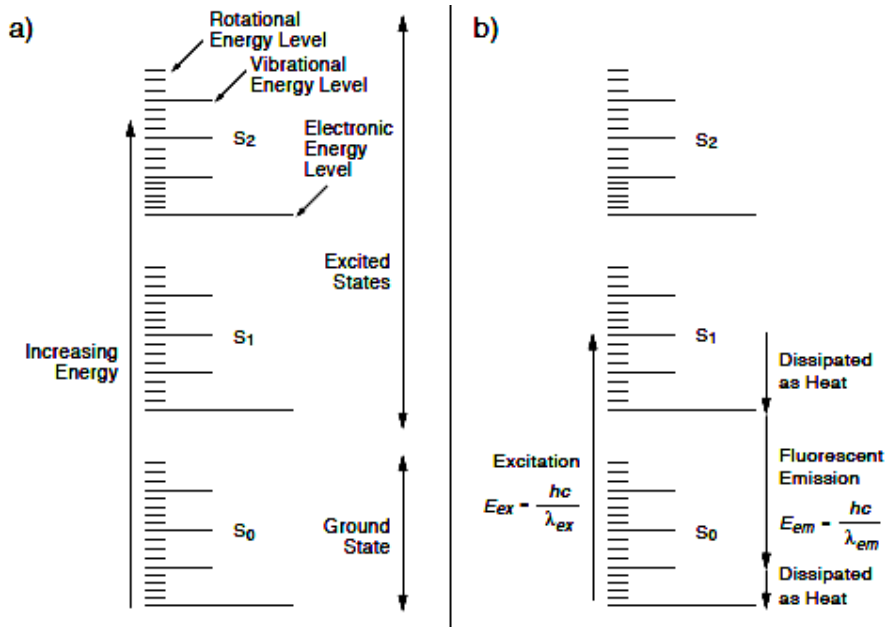

Figure 4-2 (a) Diagram of singlet energy levels of a molecule, including superimposed vibrational and rotational energy levels. (b) Example of excitation and fluorescent emission – E = energy difference between the origin and destination energy levels during excitations and emission of light; h = Planck's constant; c = the speed of the light; λ = the wavelength of the absorbed or emitted light. The energy of the light is inversely proportional to the wavelength of the light ($E = hc/\lambda$) that is, shorter-wavelength light is higher energy than longer-wavelength light. (Amersham Biosciences Technical Note # 57*)*

4.2.3 Planar laser induced fluorescence (PLIF)

Planar laser induced fluorescence (PLIF) is an optical technique developed since the 1980's to characterize gas and liquid phase fluid flow situations. Depending on the application, PLIF can be used for both qualitative (e.g. flow visualization) and quantitative measurements of species concentration, temperature, velocity and pressure. In a PLIF measurement, a laser source is used to form a thin sheet of light, which pass through the flow field under investigation. The probed volume can be a homogenous fluid into which a fluorescent dye is being added or injected or, alternatively, may contain some fluorescent particles used as tracers. The fluorescent species present in the flow are excited by a laser light with its wavelength tuned to their absorption band. After some time, usually over the order of few nanoseconds to microseconds, a fraction of the absorbed photons may subsequently be re-emitted with a modified spectral distribution, which changes for different molecule. The emitted light, known as fluorescence, is collected and typically imaged onto a solid-state array camera. The amount of light detected by a pixel of the camera depends on a number of different variables, such as, the concentration of the interrogated species within the corresponding measurement volume and the local flow field conditions, i.e., temperature,

pressure and mixture composition.

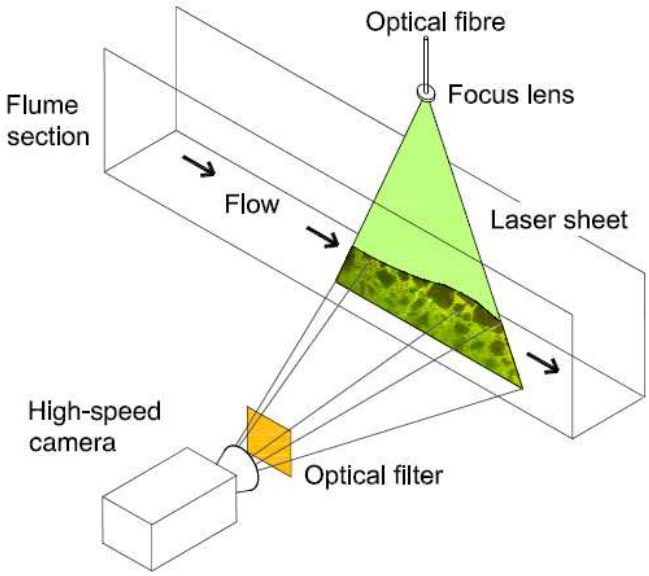

Figure 4-3 Schematic layout of the adopted PLIF configuration

4.3 Adopted technique

The PLIF technique has been used in the present work to investigate the internal velocity distribution of solids and local shear/volumetric strain development inside the flowing mass of a granular material moving down slope within a small scale flume with rectangular section.

The transparent mixture used in this study is made by solid particles of glass and a fluid phase of hydrocarbon oil with closely matched indices of refraction. In order to allow the distinction between the solid particles and the fluid, a fluorescent dye is added to the fluid phase. A laser light excites the dye that marks the fluid. This fluorescence enables both geometry and deformation through the particle-fluid system to be observed, since the particles in an image appear dark against a bright background.

The layout of the setup components, which are detailed in the following subsections, is shown in Figure 4-3. The main components of the system are the flume, the imaging devices (camera and optical long pass filter) and the devices for illumination (laser, optical fibre and lenses). The set up of the test is similar to the previous one described in Chapter 2. There is a hopper at the head of the flume from which the solid-fluid mixture is released. The optical fibre delivers the laser light from the laser to the section of the channel, which is focused upon by the high speed camera. The

sector of the channel in which the flow behaviour is investigated is located immediately before the exit point to the runout area, approximately 25 cm from the end of the flume.

4.3.1 Light source and optics

Our PLIF light source is a 800mW solid state green laser (MGL-H-532, Changchun New Industries) operating at 532 nm with an output of 800mW. The laser beam from the laser head is coupled into an optical fibre (OZ Optics), recollimated at the fibre output, and then sent through a Powell lens generating a vertical sheet of light within the refractive index-matched medium. A sketch of the line generator system is shown in Figure 4-4. The fibre optic patchcord is a multimode fibre 25/125 (i.e. fibre has a core size of 25 µm and a cladding diameter of 125 µm). A Powell lens is used to generate a straight line, since with an aspherical curvature on its apex, the output line from a Powell lens has a uniform output intensity along its entire length (see Figure 4-5). For comparison, cylindrical lenses generate Gaussian beam profiles with hot-spot centre points and fading. The power level of the light passed through the fibre-optic cable is reduced due to losses in the fibre-optic connections and along the fibre itself. The correct coupling of the light from the laser into the fibre is crucial to minimize such power loss. After the alignment of the fibre with the laser beam, the measured loss at the end of the optical cable was around the 15-20% of the initial energy. The thickness of the laser sheet is around 2mm and the fan angle is 60°.

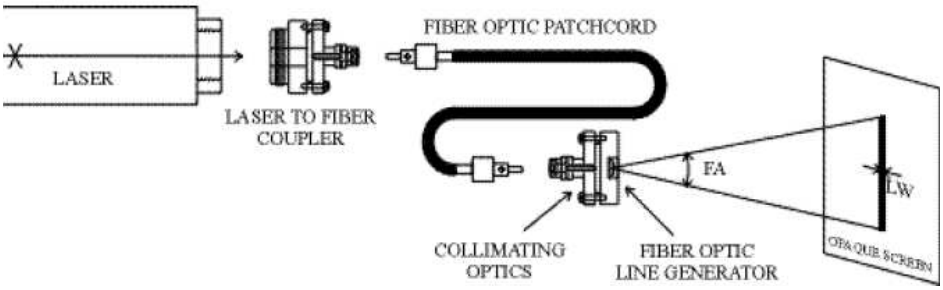

Figure 4-4 Laser line generator system (OZ Optics LTD)

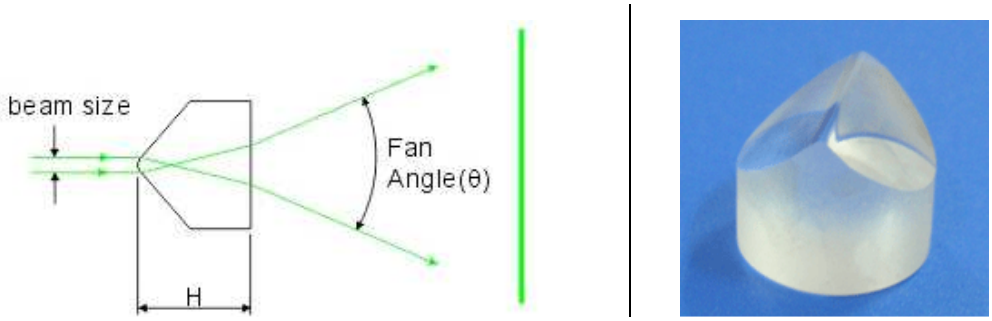

Figure 4-5 Powell lens

4.3.2 Imaging devices

A high-speed camera, SVSI model (MV-A002-M), with maximum frame rate of 500 frame per second (fps) at a resolution of 1280 x 1024 pixels is used to record the images. It employs a monochrome MI-MV13 CMOS digital image sensor from Micron with pixel size of 12 microns square, which can be controlled by a PC. The scan area on the CMOS chip is adapted to the geometry (height) of the flowing material in the flume. A partial scan area of 1280 x 256pixels is used, resulting in a pixel resolution of approximately 0.19mm in x and y directions. For each experiment the camera recorded around 6500 frames (about 6 seconds) starting from the trigger signal. A high-speed lens (Navitar, DO-5095) is used in association with the CMOS sensor. The lens is a C-Mount, 1" format lens designed for 50 mm focal length and is well suited for low light applications. During the tests a long pass filter (Schott OG550), with the cut-point at 550 ± 6 nm, is placed over the camera lens to limit the imaging to these emission wavelengths of the fluorescent dye and to screen unwanted scattered light (the transmittance curve is shown in Figure 4-6).

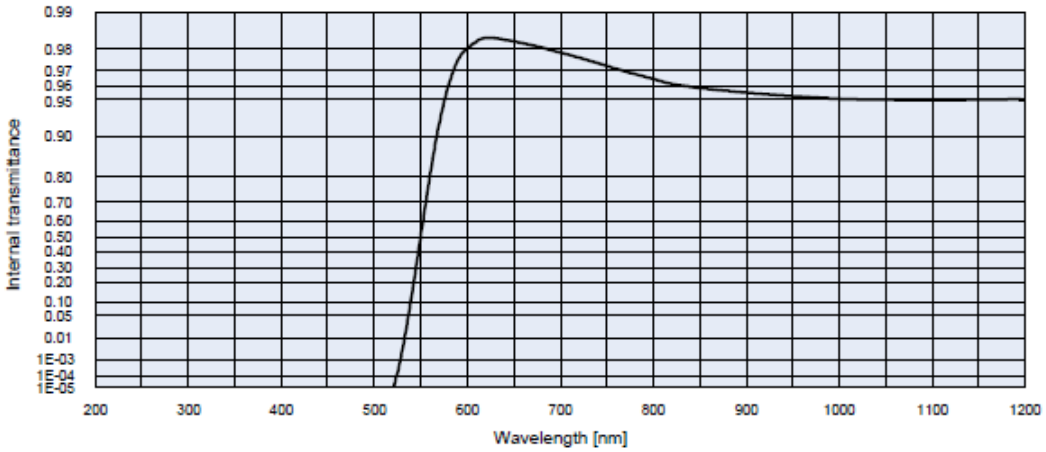

Figure 4-6 Internal transmittance of the employed optical filter at reference thickness d [mm]= 3 (SCHOTT data sheet)

4.4 Materials

4.4.1 Solid, fluid and dye properties

There are several key concerns in choosing appropriate pairings of transparent particles and associated fluids. They must be optically compatible in terms of refractive index, reasonably economic and non-hazardous to work with.

Borosilicate glass Duran (Schott Duran®) is used as transparent material for the solid particles. Borosilicate glass is widely used in chemical and engineering applications as it is chemically resistant, has a low thermal expansion coefficient and can be used at relatively high temperatures. It is available in many forms, such as rods, tubes and plates, and in many sizes. A synthetic hydrocarbon oil (Cargille Immersion Liquid code 5095) is used as the fluid phase. Both the oil and the glass change refractive index with temperature and wavelength. In Figure 4-7, the wavelength dispersion of the refractive indices for Duran, at 21℃, and the oil, at 25℃, is shown. The temperature coefficient of refractive index, which expresses the change in refractive index per ℃, is usually significantly higher for the liquid than for solids (http://www.cargille.com). Therefore changes in the refractive index of solids can be generally neglected for temperature variations of a few degrees. For liquid, it is always negative, so that as temperature increases, refractive index decreases. The temperature coefficient of the adopted oil at the sodium line (i.e. 589.3nm) is dn_D/dt =-0.0004 ℃-1. The index of refraction of the hydro carbon oil has been estimated to closely match that of Duran at the dye emission wavelength and at a temperature around 23-24 ℃. The optical and physical properties of these two materials are presented in Table 4-1. For comparison, also the characteristics of the natural debris flow material (soil and water) are shown in the same table.

Table 4-1 Solid and fluid properties

	Refractive index at 589.3 nm		Density at 25 ℃ (g/cm^3)	Kinematic viscosity at 25 ℃ (cSt)
Immersion oil	1.4715	(at 25 ℃)	0.846	16
Duran glass	1.4718	(at 21 ℃)	2.23	-
Soil	-		2.65	
Water in debris flow	1.3333	(at 20 ℃)	1.00	1-10 (dependent on clay content)

In order to allow a distinction to be made between fluid and solid and the visualization of two-phase displacements, the fluorescent dye Nile Red (Sigma-Aldrich) is used. This dye is a neutral, hydrophobic and solvatochromic dye that in non-aqueous phase is strongly fluorescent. The solvatochromic behaviour of Nile Red is such that both the absorption (excitation) and emission is dependent on the polarity of the non-aqueous solvent (Tajalli et al, 2008).

In polar solvents, the absorption and emission is red-shifted (with a decrease in fluorescence intensity) and in non-polar solvents the absorption and emission is blue-shifted. The spectral behaviour of Nile Red in solution with the hydrocarbon oil has been investigated with the emission wavelength of the laser (514 nm) employed in the experiments, and the results are reported in Figure 4-8. The dye shows a meaningful absorption rate at the laser excitation wavelength that is fundamental to achieving a high intensity of emitted light and hence to capturing images at a high frame rate during the tests. It has to be noted that the fluorescent light emitted by the dye shows a spectrum lying in the band wavelength in which the refractive indices of the oil and Duran are very close to each other. The degree of index matching at both the excitation and emission wavelength must be considered when PLIF is used, since it is impossible to create a perfect matching to both wavelengths. Non matched conditions at the absorption wavelength causes scattering and distortion of the light of the laser sheet. This condition might produce an excessive background light or illumination of the particles outside of the intended measurement plane. Imperfect matching at the emission wavelength, instead, may result in distortion of the particle images

No significant problem with the distortion of the laser plane through the mixture was found, as shown in Figure 4-23, and the effects of excessive brightness due to scattering of the light were eliminated with the use of long pass optical filter on the camera.

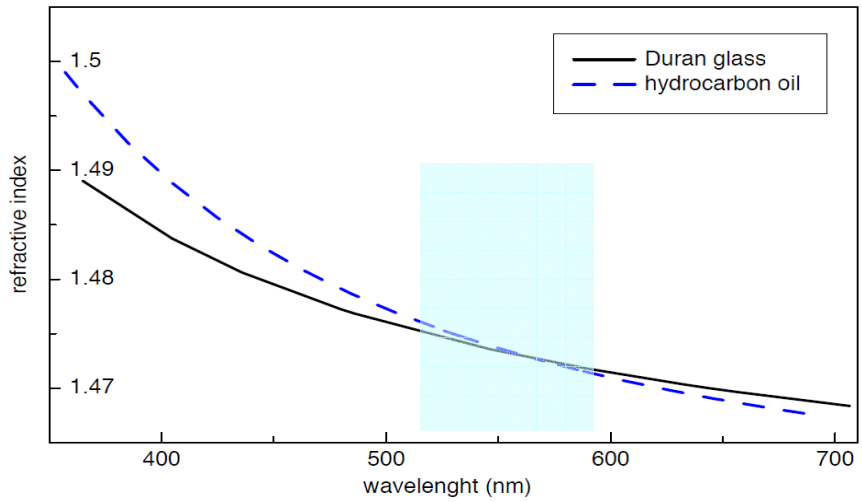

Figure 4-7 Refractive index as function of wavelength for Duran glass (Schott private communication) and hydrocarbon oil 5095 (Cargille data sheet)

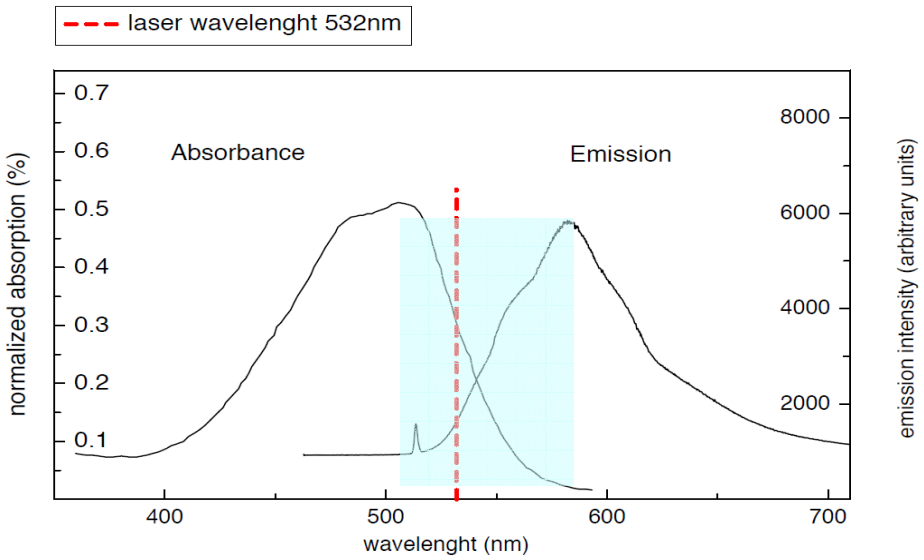

Figure 4-8 Absorption and emission spectra of Nile Red in the hydrocarbon oil. The concentration of the sample is 5mg/l

4.4.2 Scaling of the particles

A further important aspect in the experiments is that the relative densities of the particles and the fluid can be reasonably compared to real debris flows. The same does not hold for the fluid viscosity. It is not possible to exactly match the properties of real granular soil and water in this regard, since the fluid viscosity of hydrocarbons tends to be larger than that of water. The viscosity of the fluid strongly affects the hydraulic behaviour of debris flow during the motion and consolidation of the deposit. Hence, assuming laminar flow, in order to obtain a realistic modelling of consolidation behaviour of debris flows in laboratory tests, the solid particles needed to be up-scaled four times in comparison to the prototype laboratory particle size distribution. The details about this assumption and its verification will be described in Chapter 5. Scaling up the particle size enables an increase in the permeability of the system and even the smaller particles to be visible in the captured images

The particle size distribution investigated in the preliminary dynamic tests, presented in Section 4.6.2, is a well graded material with D_{50}=7.14mm and a coefficient of uniformity, C_U=9.8 obtained by scaling up four times the prototype gradation curve based on PSD11 as investigated in Chapter 3. The reference prototype and up-scaled gradation curves are reported in Figure 4-9.

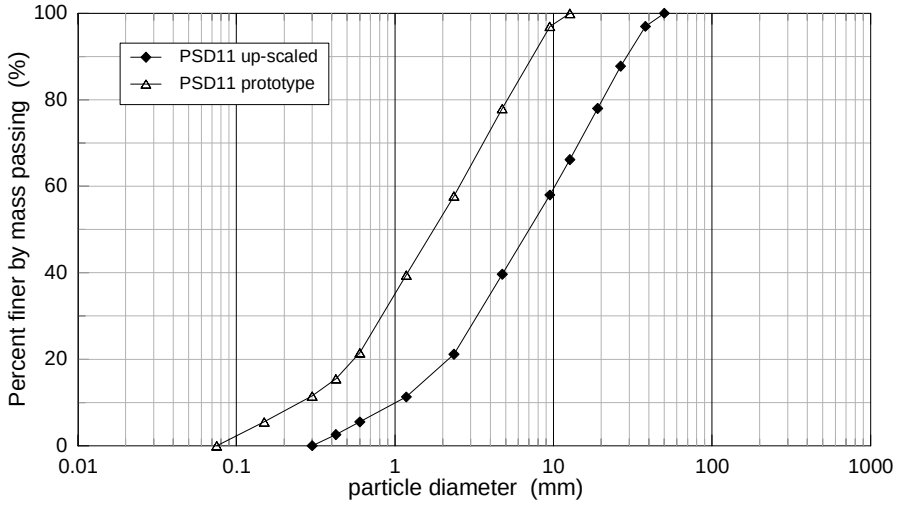

Figure 4-9 Particle size distribution scaled up used for the preliminary test

4.4.3 Preparation of particles

Since randomly shaped glass particles up to 30mm are not commercially available, a specific methodology has been developed to produce them. The borosilicate glass has been purchased from the manufacturer (Schott) in rods with diameters from 4mm to 30mm and tubes with wall thickness ranging from 0.8mm to 2.0mm (Figure 4-10). Tubes have been used to obtain the particles with sizes smaller than 4mm while rods have been used for producing the larger particles of the PSD employed in the tests. In the first instance, the tubes were crushed with a hammer. The pieces of tubes were covered with a cloth to prevent flying splinters and the escape of dust. However, only small amount of glass can be crushed in this way. Therefore, another procedure had to be found. For the smaller particles, a crusher made of two steel square slabs with sides of approximately 25cm, was employed. The tubes were placed between the two slabs and crushed by means of repeated drops of the upper plate on the lower one, until the particles were reduced to the required size. Figure 4-12 shows the adopted device. Since the resulting size distribution was broad, the glass grains had to be sorted by means of drying sieving and subsequently washed with water in order to remove the dust. The larger particles up to 30mm were instead obtained from the rods. Cylindrical pieces of glass were sliced using a bench drilling machine provided with a flat head steel tip (Figure 4-11) and subsequently shaped with a hammer in order to achieve an irregular surface. The particles with size larger than 30mm were made by smashing a 28cmx15x6cm block of Pyrex® glass (Dow-Corning), which is a borosilicate glass with the same optical characteristic of Duran but of a different brand (no longer produced). The different production techniques adopted led to different typical particle shapes: sub-angular and sub-rounded for the cut particles, more angular and elongated for the crushed ones. In Figure 4-13 to Figure 4-15 a number of coarse, fine and very fine particles are shown.

Once the particles were produced and/or at the end of each experiment (when they were mixed with the oil), the solid grains needed to be washed and dried in order to be sieved again and recycled for another test. Preliminarily, the oil was separated from the particles, in order to avoid the formation of particles clusters during the sieving. Even the presence of a small quantity of oil stuck on the particle surface, can make the correct sorting of the particles hard. In addition, removing any possible impurity, especially from the finer particles, is crucial to achieve a good transparency of the solid-fluid mixture during the experiments. The oil can be removed using different solvents (Ethyl Ether, Heptane, Methylene Chloride, Naphtha, Toluene, Turpentine, etc). The procedure used here consisted of repeated rinses of the particles with methylated spirits (ethanol with 2% of methanol). The dirty material was immersed in a container filled with this solvent. The oil was partially soluble in this liquid so that the oil was removed from the surface of

the particles and, having a density higher than that of the methylated spirits, it settled on the bottom of the container where it could be easily removed by means of pipette or syringe. After each rinse the material was washed with water and dried. The procedure generally was required to be repeated four-five times before achieving good results. After that, a visual inspection of the sieved dried particles was performed in order to remove any dirtiness present on the glass by means of tweezers.

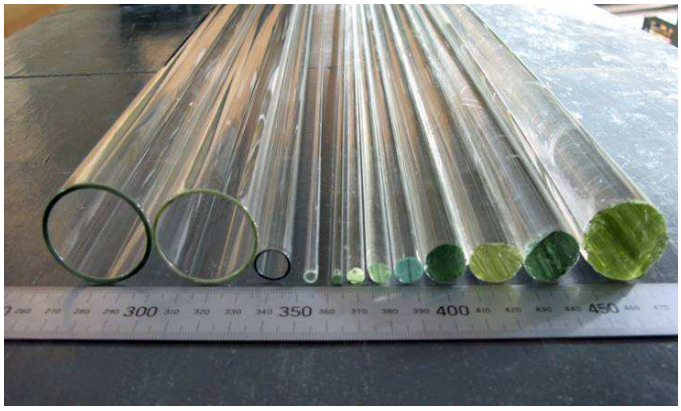

Figure 4-10 Rods and tubes used for the production of the solid grains

Figure 4-11 Bench machine used to produce the larger particles by cutting the glass rods

Figure 4-12 Steel slabs used for crushing the glass tubing

Figure 4-13 Coarse glass particles used as transparent solid

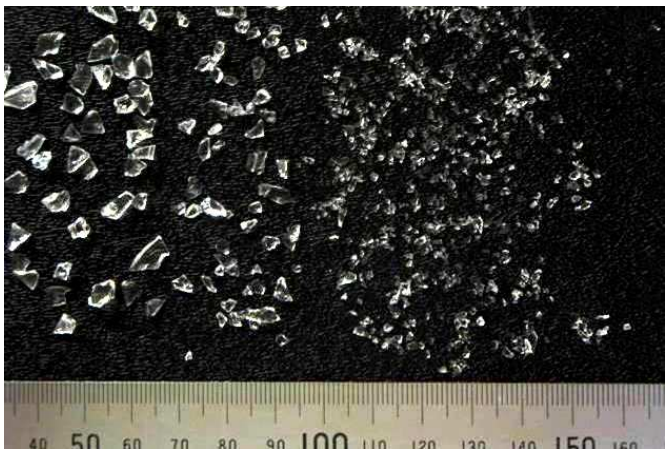

Figure 4-14 Fine glass particles used as transparent solid

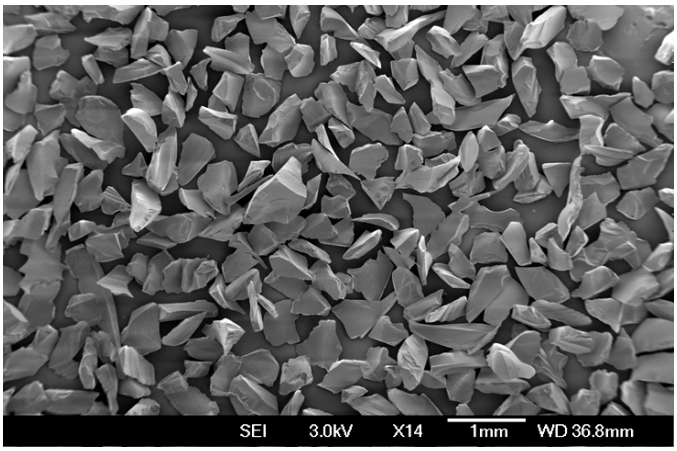

Figure 4-15 SEM image of 300 μm particles at 14X magnification

4.5 Flume apparatus

The test apparatus is a small scale flume with a rectangular section designed and constructed based on the original flume described in the Chapter 2. The experimental apparatus is shown in Figure 4-16. The major differences in comparison to the original flume are the length of the straight part of the channel, which is longer, and the smaller section width.

The flume has an aluminium hopper with a curved chute that guides the flow from the mouth of the hopper to the top of the slope, at which point the flow travels down a 150mm wide by 2000mm long channel before being deposited on a horizontal runout surface. The deposition area, made of marine plywood and varnished but not roughened, is 0.67 m wide and 2.38 m long and marked with a 50mm grid.

The slope angle can be varied from 0° to 40°. The b ottom of the channel is made of stainless steel which is artificially roughened over the last 1m by means of a synthetic material with a slip resistant surface (3M Safety-Walk 370). The outward facing walls are completely transparent and they are made of Perspex, except from the last meter before the exit point (corresponding to the rough bed). On the side facing the camera, the wall of this section is made of borosilicate glass, in order to prevent light to be refracted passing from the experimental material, through the glass outside wall. The opposite wall is made of standard glass. The pneumatically operated hopper trapdoor is linked by a micro switch to the high-speed camera to ensure a coordinated time-delay between the release of the material and the beginning of the recording of the flow.

The position and the height of the tank above the curved chute can be varied along its length that is approximately 1.4m. Several preliminary tests were carried out to analyze the influence of the position of the hopper on the release of the material and consequently on the flow behaviour of the mixture, in particular with respect to the formation of air bubbles during the release process. The tank was placed 0.46 m before the beginning of the straight part of the channel. The height and the inclination of the hopper were set in order to let the trapdoor open completely during the release of the material, trying to avoid any free fall of the mixture and to get as smooth as possible discharge.

Two different configurations were designed and tested to identify the most appropriate placement of the laser sheet during the test. In the first set up, the line generator lens was located above the channel illuminating the flow from the top, as shown in Figure 4-16 and Figure 4-17. The level of detail of the flow images taken during the tests performed with this configuration is not ideal since the mixture appears slightly blurred. This is likely to be due to the presence of particles not

completely immersed in the oil on the free surface of the flow. The interactions between the incident light and the surface of these particles can cause distortion of the planar laser beam. This results in a broadening of the laser sheet and in the illumination of the particles outside of the intended measurement plane focused on by the camera (see Section 4.6.1 for further details).

In order to overcome this issue the flume apparatus was redesigned to apply the laser sheet from beneath the flow through the base of the channel. The steel base of the channel, in correspondence of the last 1 meter before the exit point to the deposition area, was replaced with a standard glass plate as shown in Figure 4-18. The upper glass surface was covered by means of the same synthetic material already used to provide the necessary roughness at the bed of the flume. A slit 30cm in length and 1.5mm was cut in correspondence of the line generator lens to let the light pass through the base glass, illuminating the flow (see Figure 4-18). The final layout of the components is shown in Figure 4-19.

Figure 4-16 Set up of the flume with the laser from the top and particular of the different material on the bed of the channel (steel surface at the first half and synthetic rough material in the last 1m portion)

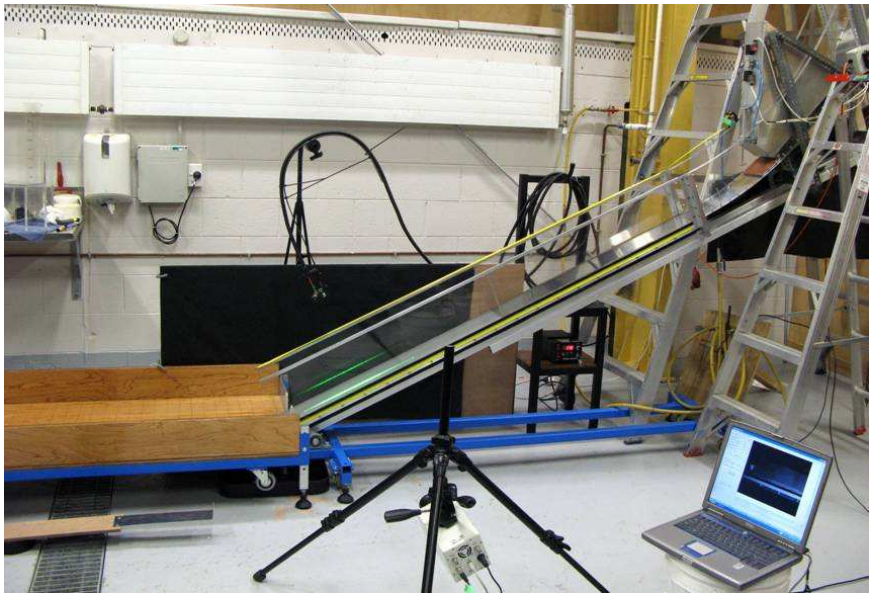

Figure 4-17 Experimental set up with the laser light coming from above the flume

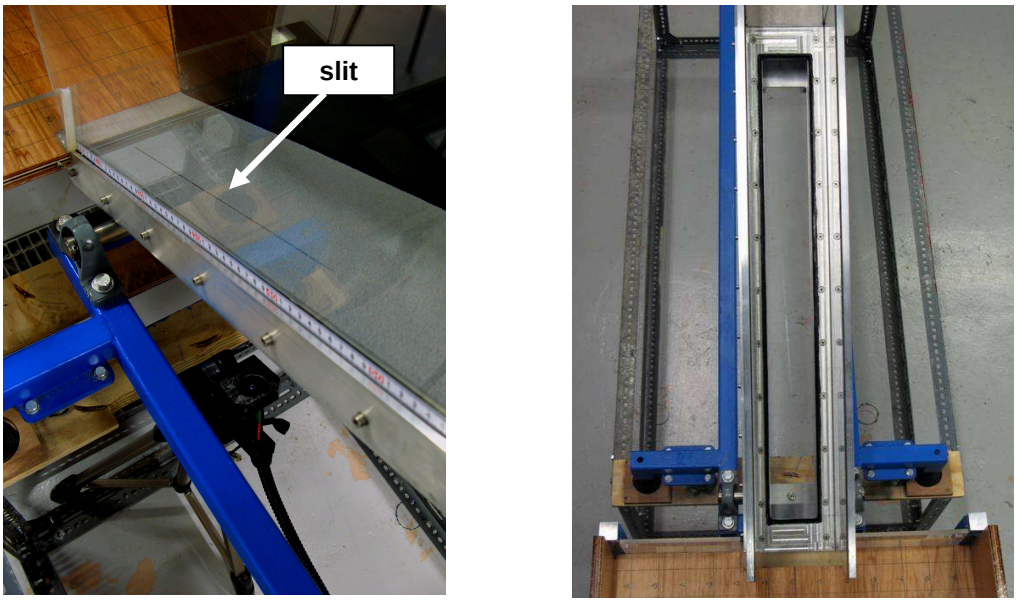

Figure 4-18 (a)) Laser line generator lens beneath the flume and the slit on the rough material at the bottom of the channel (b) glass plate used as bed of the flume

Figure 4-19 Experimental set up with the laser line generator lens beneath the flume

4.6 Preliminary tests and results

Two types of preliminary experiments were performed with the adopted solid-fluid mixture. The first series of tests focused on verifying the achievable level of transparency of the material and the influence of the particle size gradation on the maximum section depth that could be investigated within the medium. During these tests the material was analysed in a static configuration, i.e. at rest in a container.

The second type of experiments addressed the general behaviour of the mixture moving at high velocity and the tuning of the high-speed camera and the overall experimental apparatus. These tests were crucial in order to understand the effectiveness of this technique for studying granular flow in dynamic conditions entailing not only high speed particles, with velocity of a few meters per second, but also the potential presence of air bubbles, particles floating on the free surface and high concentration of the solid grains. These aspects are always present in small-scale flume tests and cannot be completely removed, but may be minimized by a careful and accurate set up of the experimental system.

4.6.1 Static condition

As already mentioned in Section 4.2.1, different factors can substantially reduce the transparency of the solid-fluid mixture. Embedded air bubbles, impurities inside the mixture, imperfections in the solid particles, and variations of the refractive index of the liquid caused by changes in temperature, can limit the depth of optical accessibility (Cui and Adrian, 1997). Several tests were performed to estimate the achieved level of transparency.

The experimental apparatus for investigation of the static condition consisted of a rectangular box made of borosilicate glass, 230 mm long and with the same width as the flume, i.e. 15 cm (see Figure 4-23). Two different mixtures were investigated – a coarse relatively uniform particle size distribution, with grain sizes ranging from 4 mm to 30 mm ($D_{50} \approx 11.5$) and a finer well graded one, with particles sizes from 0.300 mm to 38 mm ($D_{50} \approx 7.2$mm). In both cases the solid concentration was 0.57 (i.e. porosity = 0.43), the concentration of the dye was 2.5 mg/l and the room temperature was around 19 °C. Before testing, the air bubbles entrapped in the mixture during the pouring of the material were removed by gently stirring the mixture. The laser was placed above the box and images of laser-illuminated sections were taken at different depths, in particular at 75 mm (the middle section) and at 45 mm from the glass sidewall as shown in Figure 4-20, Figure 4-21 and Figure 4-22. The captured images were recorded by the high-speed camera with frame rate set at 200 fps. The coarser mixture proved to be highly transparent, while the finer one turned out to be

difficult to penetrate optically when the laser sheet was positioned in the middle section. The presence of smaller particles resulted in a greater degree of scattered light within the system via slight differences in refractive indices at the solid–liquid interface. Better optical resolution was achieved when the laser sheet was placed at 45 mm from the wall – this captures flow at a distance that was felt to be sufficient to avoid the majority of unwanted edge effects. Therefore, the laser plane during the preliminary dynamic tests was set at 45 mm from the borosilicate sidewall in correspondence to the longitudinal section of the flume.

In the experiments described in Chapter 6 the laser sheet was positioned closer to the outside wall, specifically at 35 mm. This distance was chosen to improve further the quality of the recorded images and to make, at least in this development phase, the application of post-processing image analysis easier. In any case, it is worthy to note that the depth of the internal section can go up to 45 mm with a reasonable level of detail in the recorded images.

Moreover, it has been observed that the interaction of the incident laser light with the particles protruding from the free surface of the mixture, i.e. not completed immersed in the oil, could cause distortion and splitting of the laser light sheet outside of the intended measurement plane focused on by the camera as shown in Figure 4-24. As discussed in Section 4.5, adjustments of the flume apparatus were designed to allow the laser sheet illuminate the mixture passing through the base of the channel as explained in the details in the previous section.

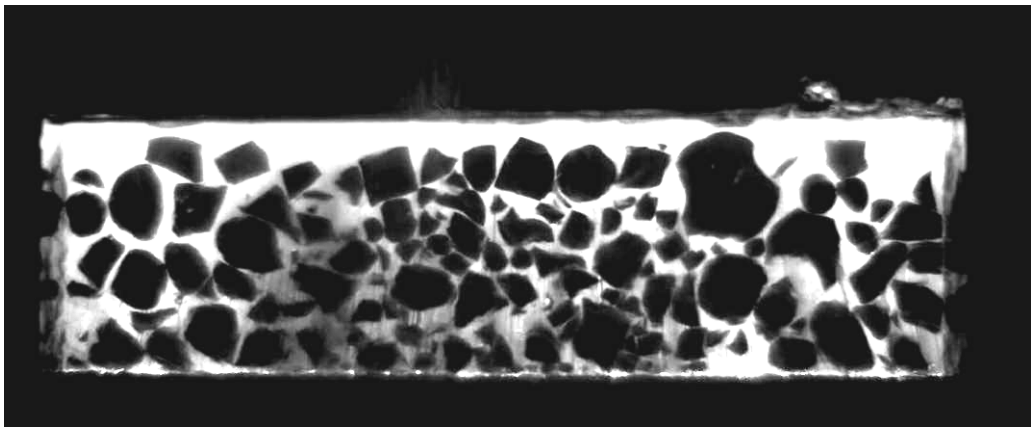

Figure 4-20 High-speed camera image of the coarse mixture captured at the middle section of (75 mm from) the borosilicate box test

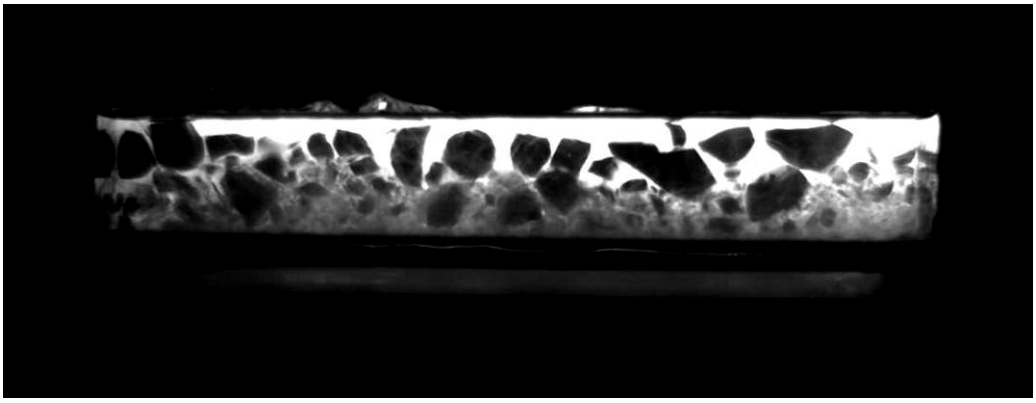

Figure 4-21 High-speed camera image of the finer mixture captured at the middle section of (75 mm from) the borosilicate box test

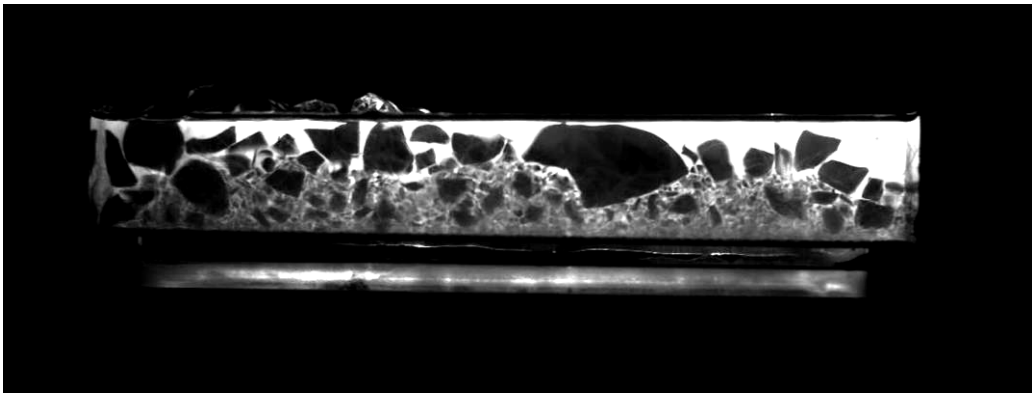

Figure 4-22 High-speed camera image of the finer mixture captured at the section 45 mm from the outside wall of the borosilicate box test

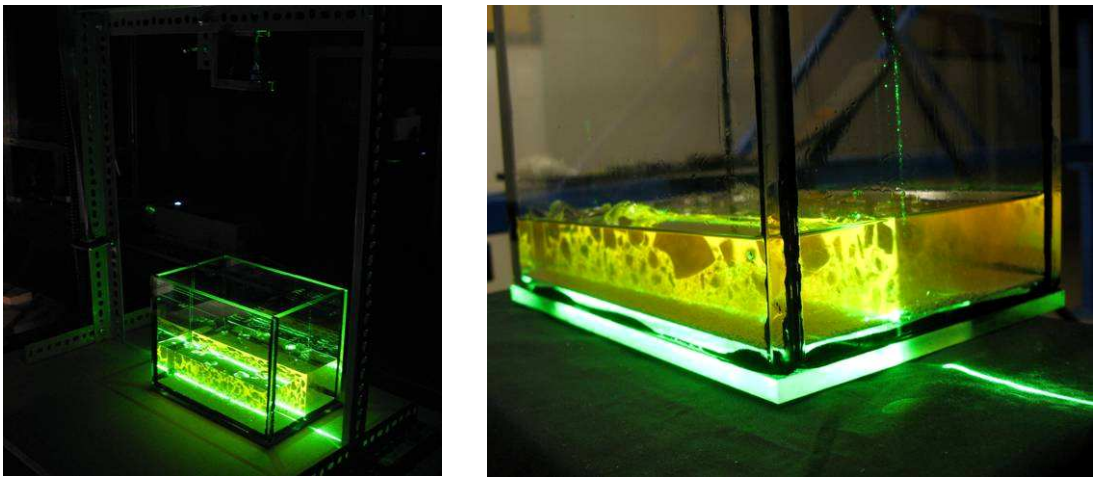

Figure 4-23 Borosilicate glass box used for testing the mixture in static condition

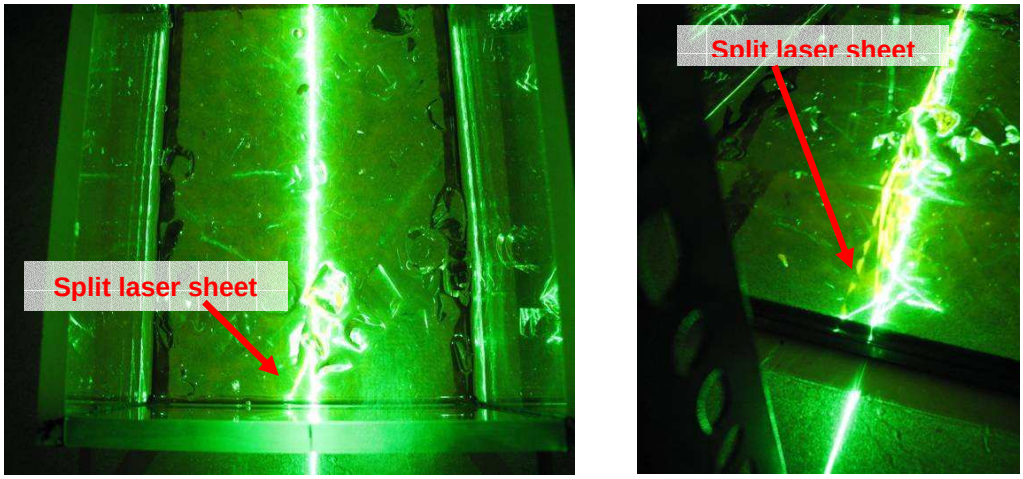

Figure 4-24 Laser splitting due to particles protruding from the free surface

4.6.2 Dynamic condition

Several tests were run with the slope angle varying between 24.5 and 26°, an initial mixture prepared with a solid mass of 8 kg saturated with 2.66 litres of oil (that means an average solid concentration of 0.57) and a dye concentration at 2.5 mg/l. Different aspects of the experiments were considered.

- Camera frame rate

  Different camera frame rates were tested in order to achieve the best recording quality according to the following requirements:

- the frame rate had to be high enough to follow the motion of the particles at sufficient resolution
- the exposure time, which depends on the inverse of the frame rate, had to be sufficient to have acceptably bright images

Three recording rates were analysed, 400, 900 and 1200 fps. At 400 fps the images had a good brightness level but were very blurred. At 900 fps the images were acceptably clear and well defined. Finally, at 1200 fps the level of detail was extremely good, but the resulting images were too dark. However, the brightness could be improved by means of a suitable image processing software (e.g ImageJ, GIMP, etc). Finally, due to the limited amount of available storage in the high-speed camera (3 GB), the frame rate was set at 1100 fps to allow a longer recording time.

− Flow height, velocity of mixture and presence of air bubbles

The average flow height during these preliminary experiments was found to be approximately 2-3 cm. The detected speed of the flow at the control section was found to be around 1.5 to 2 m/s, comparable to that of the similar small scale prototype-laboratory debris flows tests described in Chapter 3 (Bowman and Sanvitale, 2009).

Since one of the goals of the experimental flow tests was the analysis of the internal velocity distribution of solids inside the flowing mass, it was decided to increase slightly the height of the flow changing the initial source mass by 50% (i.e. up to 12kg).

The presence of air bubbles inside the mixture cannot be entirely avoided during the flow. In this regard, as well as stirring the mixture before release from the hopper, the only structural improvement that was tried was to vary the position of hopper at the beginning of the slope flume. Several different positions, inclinations, and height of the hopper were tried in order to make the discharge of the material smooth to minimize the entrainment of the air, at least at the beginning of the flow. In particular, any free fall of material from the hopper was avoided as is shown in Figure 4-25. Probably, a hopper or tank with a sluice gate at the head of the flume could be a better option for the design of the experimental apparatus.

− Flow segregation and deposit morphology

The experimental debris flows typically are thin, rapidly moving, unsteady, and non-uniform. After release, the source mass rapidly elongates and thins as it flows down slope (Iverson and LaHusen 1993). The front of each flow is usually preceded by a series of dry bouncing coarse particles. Due to sorting processes of particles during the motion, the flows typically develop a front containing a concentration of the coarsest particles followed by a gradually thinner, finer-grained body.

In Figure 4-27 digital images of the flow captured with the high speed camera are shown. The flow is proceeding from left to right and the camera is positioned at an angle so that the base of the channel is parallel to the horizontal in the images. Figure 4-27 (a) shows the front arrival. Note that the material is not saturated here and hence there are gaps in the flow, while individual particles are most visible as illuminated blocks. Prior to this, some discrete large particles came tumbling down as is typical at the front of segregating debris flow. Figure 4-27 (b) shows the core of the flow. Black indicates particles in the line of the laser sheet, while some particles protrude from the flow distorting the light and creating secondary particle shadows – the line of saturation can be seen as a wavy black line. Figure 4-27 (c) shows the tail of the flow, where particles are noticeably finer than earlier. It is clear that the head and tail morphology of the experimental flows obtained using the glass-oil mixture mimic characteristics of those of soil-water mixture (Major, 1999)

Figure 4-26 shows the typical experimental flow deposit at the base of the slope for the well-graded particle distribution employed. The material deposited on the runout area exhibits morphologic features common to many natural and laboratory debris flow fans (Major and Iverson, 1999) with coarse particles concentrated at the front and at the outermost margins, while the finer material is emplaced at the rear of the fan.

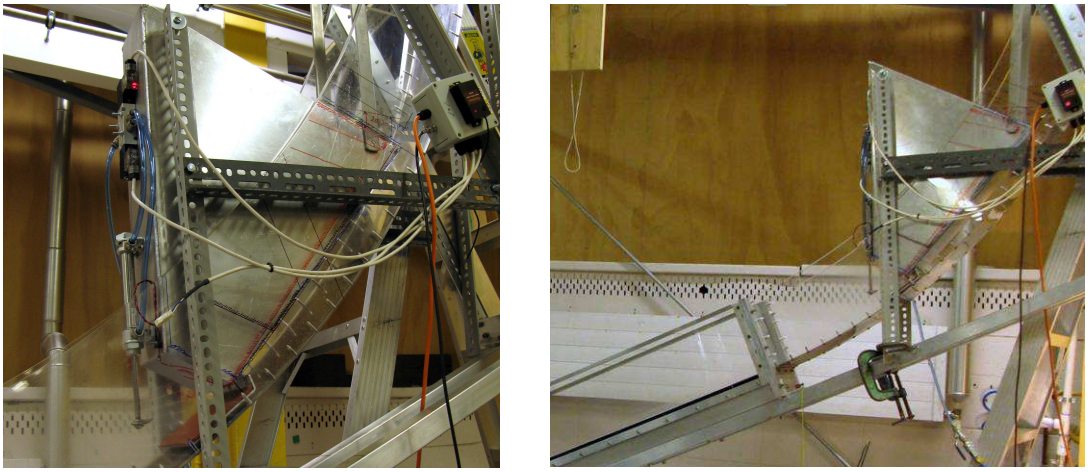

Figure 4-25 Tank at the head of the flume

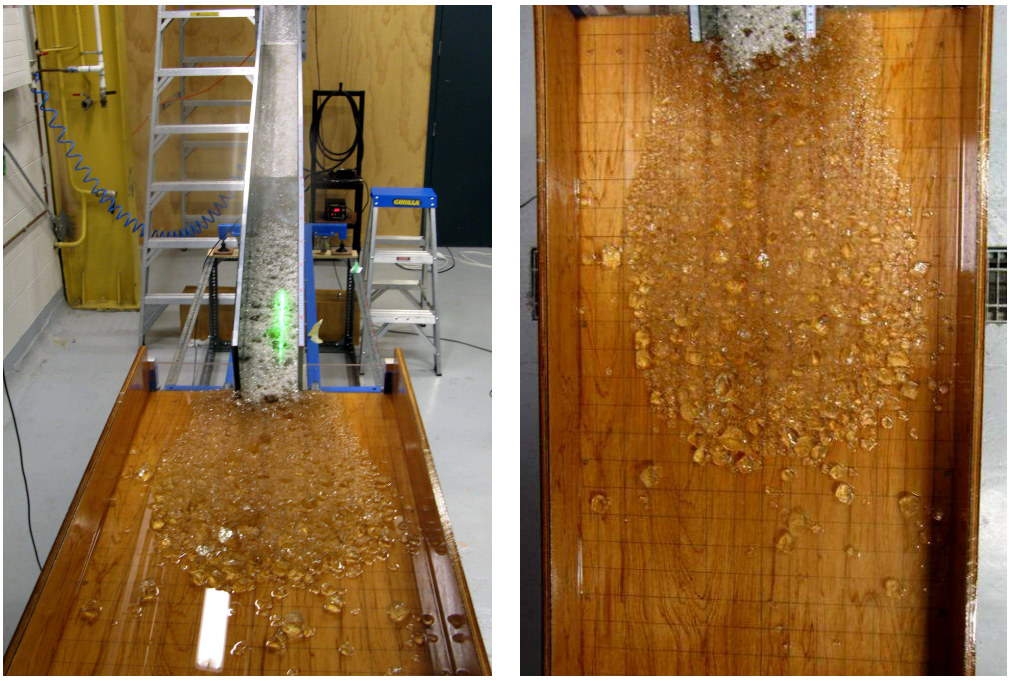

Figure 4-26 Typical deposit at the base of the slope

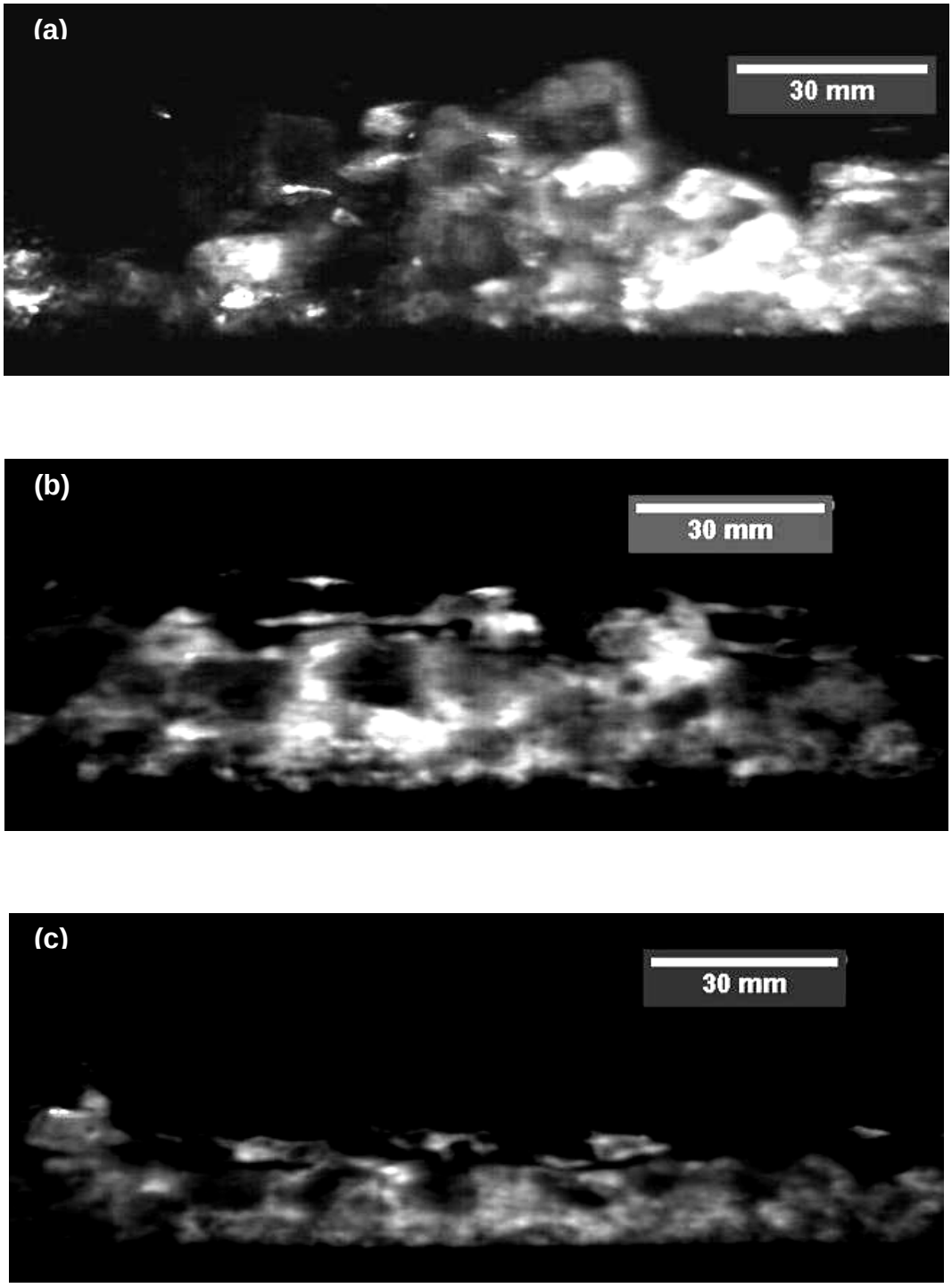

Figure 4-27 Digital images of the flow captured at the control section 45 mm within the medium: (a) During arrival of the flow front; (b) In the core of the flow; (c) In the tail of the flow.

4.7 Test procedure

Once the construction of the flume, its adjustments and the static, dynamic and permeability tests on the glass-oil mixture were completed, three characteristic particle size distributions, PSDs, were selected for detailed debris flow model testing (the details are reported in Chapter 6). The procedure followed during these tests is similar to that used with the original flume as reported in Section 2.4.3.

For each run, a mixture prepared with 12kg of glass particles saturated with 3.94 litres of oil was used. The overall sediment volume concentration of the mixture was 0.57, the same as the soil-water mixtures used in the experimental research conducted in the original flume. The concentration of the Nile Red in the oil was 2.5 mg/l, the laser power set around 600 mW and the frame rate of the camera at 1100 fps. The slope angle was kept constant at 24.5°.

The tests were performed in a dark room without control of the temperature. Since the refractive index of the fluid is very sensitive to the temperature, the prepared mixture was kept in a separate room at a temperature of around 22 °C until the beginning of the test (the temperature of the mixture was recorded prior the running of the experiments and it generally ranged around 20-22 °C).

Before each test, some images of a calibration target sheet, necessary for the post-processing image analysis, were taken. The calibration sheet depicts a grid of points whose locations are precisely known. This sheet was attached to a Perspex board that was positioned inside a transparent box made of borosilicate glass and filled with oil. The oil inside the box enabled images of the targets points to be captured with the same distortion as the flow images during the test and consequently to lead to a precise calibration. Before the test, the box was inserted inside the flume in correspondence to the section focused upon by the high speed camera. It was positioned so as its side touched the outside borosilicate wall of the flume (i.e. those facing the high-speed camera). Then, the position of the board inside the box was adjusted to put the calibration target within the plane illuminated by the laser sheet during the test, as shown in Figure 4-28. Finally, images of the target points in this configuration were recorded for future image post-processing.

After this preliminary phase, the test material was poured into the hopper and continuously stirred to prevent settling, release any entrained air and ensure a homogeneous mixture until the experiment was ready to be run. The release of the trapdoor was linked by a micro switch to

the camera to allow a delay between the release of the material and the beginning of the image recording, thus capturing the flow during its motion.

After each test, measurements of the runout and collection of samples from the deposit were carried out according to the procedure described in Section 2.4.4.

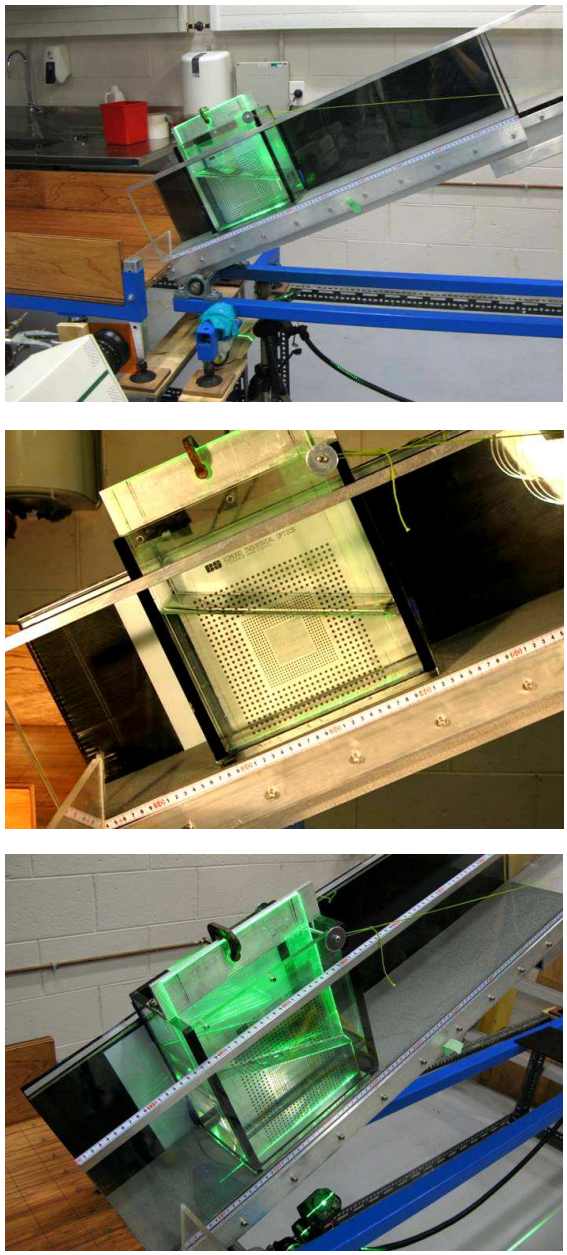

Figure 4-28 Position of the calibration target inside the flume

Chapter 5

Permeability of the mixtures

5.1 Introduction

It is not possible to exactly match the physical properties of a real granular soil and water mixture with those of Duran glass particles and hydrocarbon oil. The viscosity of the fluid strongly affects the hydraulic behaviour of the mixture during the motion and the consolidation of the deposit. The hydrocarbon oil employed in the experiments described in Chapters 4 and 6, has a viscosity higher than that of water. To obtain compatible hydraulic behaviour between the natural and artificial mixtures, the glass particles size was scaled up. In order to measure the hydraulic conductivity of the resulting mixture and compare it to the natural one, a specific analysis is required. In this chapter we describe the tests accomplished for this purpose. In Section 5.2 a short overview about permeability and indirect methods for its estimation are reported. In Section 5.3 the assumptions regarding the scaling of the particles are described. In Section 5.4, the test conditions of the permeability tests performed are reported, while in Section 5.5 the adopted test procedure is illustrated. At the end of the chapter, in Section 5.6, the results are discussed

5.2 Background

Permeability (more properly referred to as hydraulic conductivity) is the parameter that describes how easy it is for water to flow through soil. According to fundamental hydraulics, flowing water may assume either of two characteristic states of motion: laminar or turbulent. In

laminar flow, each fluid particle travels along a definite path, which never crosses that of any other particle. In turbulent flow, the paths are irregular and twisting, crossing and recrossing randomly (Taylor, 1948). Reynolds (1883), from his experiments on flow through pipes, found that the flow is laminar, as long as its velocity is less than a lower critical velocity, expressed in terms of Reynolds number, Re, as follows:

$$\mathrm{Re} = \frac{v_c D \gamma_w}{\mu g} \tag{5.1}$$

where v_c=critical velocity; D=diameter of pipe/pore; μ=dynamic viscosity of water; g=acceleration due to gravity; γ_w= unit weight of water. The critical value of Reynolds number at which the flow in soils changes from laminar to turbulent has been determined experimentally by various investigators to range from 1 to 12 (Harr, 1962; Chugaev, 1971). According to Scheidegger (1957), the probable reason that porous media do not exhibit a definite critical Reynolds number is because soil cannot be accurately represented as a bundle of straight tubes. Since the pores of most soils are small, flow through them is generally laminar, however in the case of soil coarser than coarse sand the flow may be turbulent. The law describing the flow of water through soil was first studied by Darcy (1856), who demonstrated experimentally that for laminar flow conditions in a saturated soil, the rate of flow or discharge per unit time is directly proportional to the hydraulic gradient (see Figure 5-1). Darcy's law can be written as follows:

$$q = k \cdot i \cdot A \tag{5.2}$$

$$v = k \cdot i \tag{5.3}$$

where A is the cross-section area normal to the direction of flow; k is the coefficient of permeability and i is the hydraulic gradient.

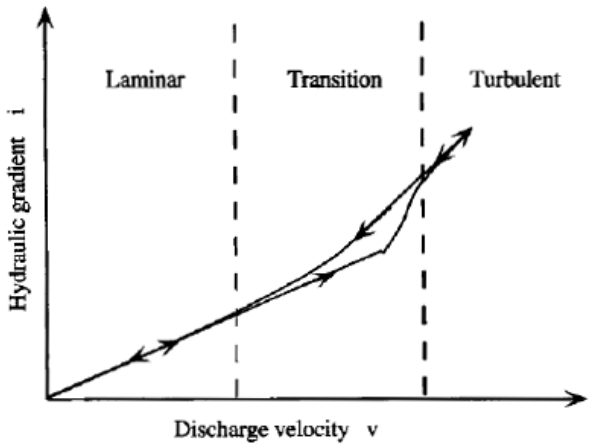

Figure 5-1 - Zones of laminar and turbulent flows (Taylor, 1948)

Equations have been derived that relate hydraulic conductivity to properties of the soil and permeating fluid. About a century ago, Hazen (1892, 1911) proposed the following empirical formula for predicting the hydraulic conductivity of saturated sand:

$$k = C_H \cdot D_{10}^2 \tag{5.4}$$

where k=permeability (cm/s); C_H=Hazen empirical coefficient and D_{10}=particle size for which 10% of the soil is finer (cm). Although Hazen developed his formula for the design of sand filters for water purifications (loose clean sands with a coefficient of uniformity C_U<2), it is frequently used to estimate the permeability of soil as well. The value of C_H is usually assumed to be equal to 100, but ranges of 40-80 for fine sands, 80-120 for medium sands and 120-150 for coarse sands have been proposed (Carrier, 2003).

Permeability depends on the characteristic of the permeant as well as on those of the soil. Taylor (1948) derived an equation that relates hydraulic conductivity of a soil with the properties of the soil itself and of the permeating fluid. The equation, based on Poiseulle's law for flow through a round capillary tube, considers the flow through a porous medium to be similar to flow through a bundle of straight capillary tubes. The equation is:

$$k = D_{eff}^2 \frac{\gamma_P}{\mu} \frac{e^3}{(1+e)} C \tag{5.5}$$

in which k=coefficient of permeability; D_{eff}=effective particle size; γ_P=unit weight of the permeant; e=void ratio; μ=viscosity of the permeant; C=shape factor.

Thus, permeability is affected by the characteristics of the pore fluid, the grain size, the voids ratio of the soil, the fabric or structural arrangement of particles, the degree of saturation and the presence of entrapped air. The influence of the permeant properties are accounted for by the term μ/γ_P indicating that permeability is directly proportional to the unit weight of the fluid and inversely proportional to its viscosity. The permeability grows with the square of the particle diameter, since the smaller the grain-size the smaller the voids and thus the lower the permeability. Equation (5.5) indicates that k is expected to vary linearly with $e^3/(1+e)$. This holds especially for coarse grained soils, since their shape factor, C, does not change appreciably with the void ratio. The structural arrangement of the particles may vary, at the same void ratio, depending on the method of deposition or compacting of the soil mass. The effect of fabric on permeability is much more pronounced in fine-grained soils. At the same void ratio, a soil in the most flocculated state is expected to have the highest permeability, while one in the most dispersed state has the lowest permeability. The permeability is also strongly reduced if air is entrapped in the voids, leading to a reduction in the degree of saturation. The higher the degree

of saturation, the higher the permeability. In the case of certain sands the permeability may increase three-fold when the degree of saturation increases from 80% to 100% (Chapuis and Aubertin, 2003)

About half-century ago, Kozeny (1927) and Carman (1938, 1956) developed the following semi-empirical, semi-theoretical formula that correlates the permeability of porous media with the specific surface of the particles:

$$k = (\gamma/\mu)\cdot(1/C_{K-C})\cdot(1/S_o^2)\left[e^3/(1+e)\right] \tag{5.6}$$

where γ=unit weight of permeant; $C_{K\text{-}C}$=Kozeny-Carman empirical coefficient; S_o=specific surface area per unit volume of particles (1/cm); e=void ratio.

$C_{K\text{-}C}$ is a coefficient taking into account the shape and the tortuosity of the pores. It is equal to 4.8±0.3 for uniform spheres (Carman, 1956), and it is usually taken to be equal to 5 for soils. The specific surface S_o, for equal spheres of diameter D, is 6/D (=surface area/ volume of a sphere). If the soil consists of non-uniform spheres, an effective diameter D_{eff} can be computed from the particle size distribution (Carrier, 2003) according to

$$D_{eff} = \frac{100\%}{\sum\left(f_i/D_{ave_i}\right)}$$

where f_i is the fraction of particles between two sizes (D_{li} and D_{si}) and $D_{ave,i}$ is the average particles size between two sizes ($=D_{li}^{0.5}\bullet D_{si}^{0.5}$). So the specific surface is found as $S_o=6/D_{eff}$. A modification for S_o which allows to take into account for the angularity of the individual soil particles, has been proposed by Loudon (1952) and Fair and Hatch (1933) introducing the following shape factor, SF:

$$S_o = SF/D_{eff} \tag{5.7}$$

Fair and Hatch suggested the following values for the shape factor, SF: spherical 6.0; rounded 6.1; worn 6.4; sharp 7.4; and angular 7.7. Loudon suggested the following values: rounded 6.6; medium angularity 7.5; and angular 8.4.

The Kozeny-Carman equation describes the behaviour of cohesionless soil reasonably well, but it is inadequate for clays, although it is suitable for non plastic silts. The formula assumes Darcian conditions, that is, laminar flow and a low pore velocity. These conditions apply in silts, sands and even in gravely sands but as pore size increases and the velocity increases, turbulent flow and the inertia term must be taken into account in the estimate of the hydraulic conductivity (Barr, 2001).

5.3 Scaling particles

According to the Kozeny-Carman equation, the permeability is expected to be inversely proportional to the viscosity of the permeant. As reported in paragraph 4.4.1, the kinematic viscosity of the hydrocarbon oil used as fluid phase in the “artificial soil” (glass particles and oil) experiments is sixteen times greater than that of water. The use of this pore fluid with high viscosity significantly reduces the permeability of a mixture composed of glass and oil, in comparison to that made of soil and water, i.e. the typical material used in debris flow laboratory experiments. Provided the fabric of the artificial soil made of glass particles is the same as the soil prototype, the permeability is expected to be only a function of μ/γ_p . Using the unit weight and the dynamic viscosity of the oil in the factor μ/γ_p , the permeability of the mixture would result approximately 17.8 times more than that obtained using water. Hence, assuming laminar flow, in order to obtain realistic modelling of the hydraulic behaviour of debris flow material during the motion and consolidation of the deposit, the solid particles are up-scaled four times in comparison to the prototype soil particle size distribution. Scaling up the particle size enables an increase in the permeability due to increase of the pore size through which the fluid can flow. It is well understood that this assumption holds as long as the fabric of the medium made of glass particles is comparable with that of the prototype soil. However, due the way the material is produced and its intrinsic properties, the glass particles will never be precisely the same as those of a real soil. For instance, the shape of the glass particles, as described in Section 4.4.3, is more angular than that of the soil prototype and the roughness of the particles is expected to be quite different from that of the soil particles. The coarse glass particles have typically smooth and polished surface, while the finer particles, obtained by crushing, may be rougher. Consequently, permeability tests have been conducted in order to verify the value of the achieved permeability in the up-scaled particle size distribution

5.4 Test conditions

The hydraulic conductivity of two different particle size distributions was measured by means of head-constant permeability tests. The first, PSD11, is a specimen of the same particle size distribution already employed for the small-scale flume tests, presented in Chapter 3, whose characteristics are described in Chapter 2. The second is a sample of Duran glass particles, produced as described in Chapter 4, with particle size distribution PSD11-up obtained by scaling up four times that of the soil for PSD11. Constant head permeability tests were

performed following the standard procedure ASTM D-2434. The fluid employed in the tests was the hydrocarbon oil for the glass sample and water for the soil sample.

The standard code requires the permeameter, which is basically a transparent acrylic cylinder that encases the sample to be tested, to have a diameter from 8 to 12 times the maximum particle size of the specimen. In addition, any particle larger than 19 mm must be separated out from the sample by sieving. According to these guidelines, given the different maximum size of the two particle size distributions under investigation, a large permeameter, with diameter of 22.8 cm, was employed for the glass material, whereas a smaller one, with diameter of 7.6 cm, was used for the soil. The act of removing particles larger than 19mm from the glass sample, causes the “effective” particle size distribution of the glass sample considered for the test to be different from the material from which the oversize particles have been removed, as shown in Figure 5-2. Since the comparative test with the soil specimen was intended to verify the effectiveness of the particle scaling in controlling the permeability of the sample, the gradation of the soil sample was modified according to that of the glass material (i.e. the equivalent particle sizes larger than 19/4 = 4.75mm were removed). This allowed a direct comparison of the values of the permeability coefficient measured with the two different materials, i.e. glass versus soil. The theoretical particle distribution to be tested and the “real” gradation employed are shown in Figure 5-2

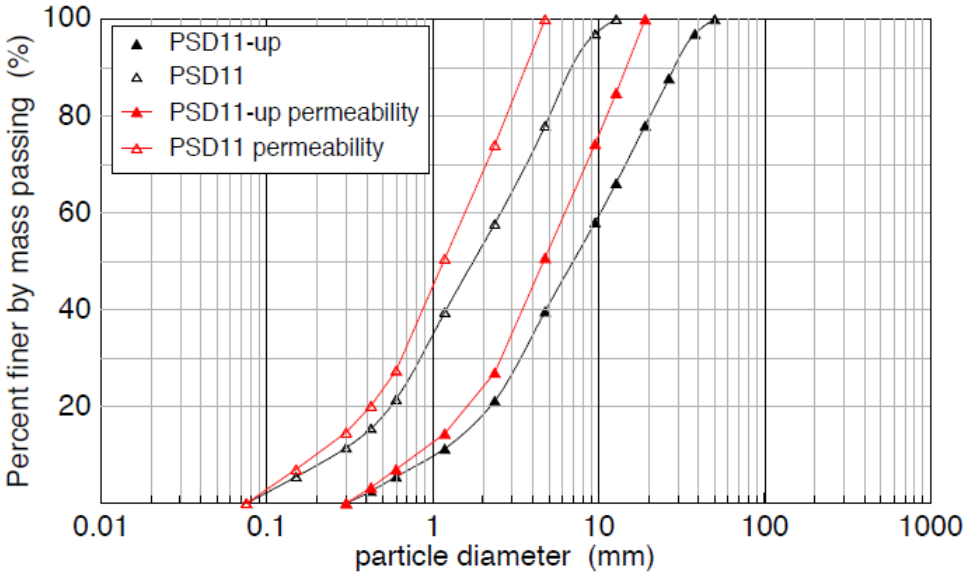

Figure 5-2 Particle sizes distributions employed in the permeability test (red plots) and reference gradations (black plots)

5.5 Test procedure

5.5.1 Permeability test using glass particles

Figure 5-3 shows a sketch of the employed devices. The set up of the test is configured in order to circulate the fluid employed (i.e. the oil) during the test. The main apparatus is a large permeameter of 22.8 cm diameter, with the distance between manometer ports on the sides equal to the diameter. The manometer ports are grooved and screened on the inside with a 150μm mesh brass. Chamber is made of clear acrylic. A spring is incorporated in the top cap to prevent soil density changes during the test. Hydraulic gradient across the specimen is applied using an inlet tank, which has an overflow to return the excess flow to the reservoir tank and hence to maintain a constant water head on the base of the specimen. A palette pump is used to supply the inlet tank with the fluid from the reservoir. The outward flow from the permeameter is returned to the reservoir tank by means of a pipe

The specimen inside the cell was reconstituted in a series of layers each about 20mm thick. Each layer was prepared using subsamples of dry glass according to the target grain size distribution (approximately 2500g particles per subsample). Before placing the material inside the cell, the glass particles were moistened with small quantity of oil in order to prevent segregation of the grains and separation of the finer particles from the coarser. Each layer was prepared by spreading the glass from a scoop. Uniform spreading was obtained by sliding a scoop of glass in a nearly horizontal position down along the inside surface of the device to the bottom or to the formed layer, then tilting the scoop and drawing it toward the center with a single slow motion. This allowed the soil to run smoothly from the scoop in a row without segregation. Thus, repeating this procedure around the inside diameter of the cell, it was possible to form a uniform layer of loose material. The top surface of the last layer was then levelled and covered with a 150μm mesh brass. Upon it, a rigid porous plate was placed. Finally the top plate of the permeameter with the incorporated spring was pressed down on the top of the acrylic cell and attached, making an air-tight seal. After the preparation, the sample was evacuated under 50cm of Hg (mercury) for 15 min to remove the air adhering to the soil particles and slowly saturated with oil from the bottom upward under full vacuum in order to free any remaining air in the specimen.

The saturation of the specimen was continued by running oil through the sample for some time until no air bubbles were observed to flow through the pipe. After saturation was completed, a number of measurements of the flow discharge through the sample for different hydraulic gradients (different heights of the inlet tank) were performed. For each value of hydraulic gradient, after a stable head condition without appreciable drift in water manometer levels was

attained, at least three measurements were collected. The flow direction during the tests was upward.

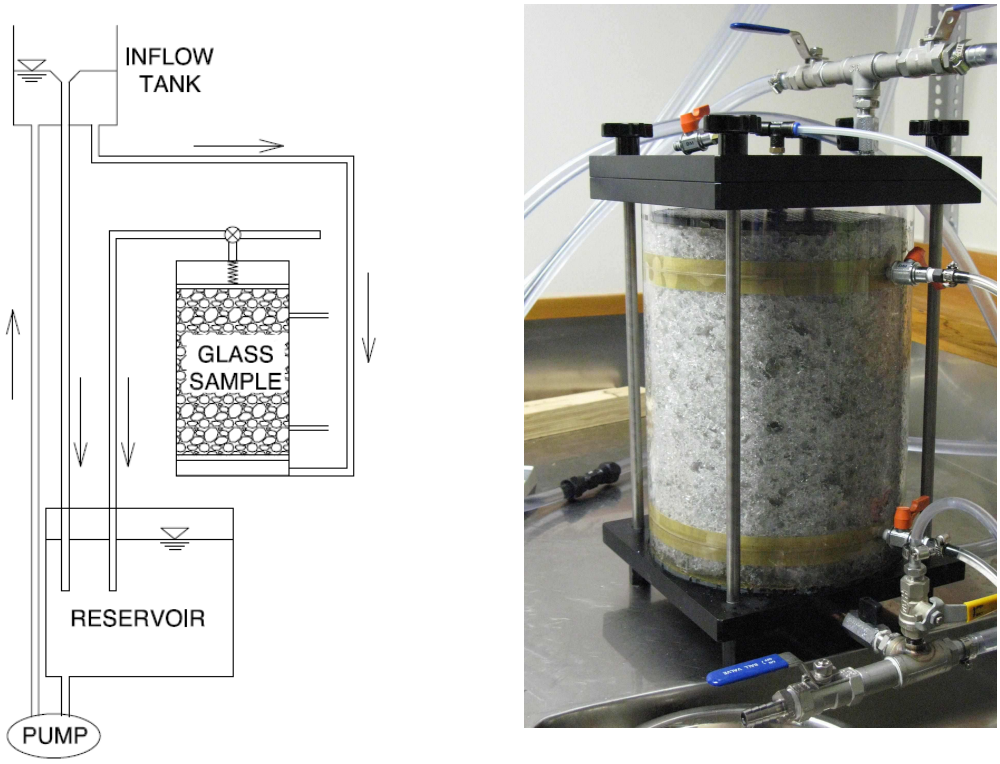

Figure 5-3 Sketch of the set up of the test with glass particles (on the left) and photo of the reconstituted sample (on the right)

5.5.2 Permeability test using soil particles

For the test using soil particles, the set up is similar to that described above except that the reservoir tank and the pump for circulating the fluid during the test were not needed. The permeameter is smaller, with a diameter of 7.6 cm and the distance between manometer ports on the sides is equal to 10 cm. The manometer ports are grooved and screened on the inside and the chamber is clear acrylic. A spring similar to that used in the large permeameter is incorporated on the top plate, to prevent soil density changes during the test. The inlet tank is the same of the previous set up previous, but in this case, the overflow is just discharged. The water supplied to the tank was de-aired water during the saturation of the sample and tap water during the test.

The specimen was reconstituted inside the cell using dry funnel deposition method. The material for the specimen was initially prepared in three different subsamples (approximately

600g each). Initially, the soil was mixed with a sufficient quantity of water to prevent the segregation of particle sizes during the placement into the permeameter. Then the funnel, placed with the spout in contact with the lower porous plate or a previously formed layer, was filled with enough quantity of material to form at least a layer of 15mm. The spread of the soil was achieved by lifting up the funnel with a slow spiral motion, working from the perimeter of the device toward the centre, so that a uniform layer was formed.

The top surface of the last layer was levelled and covered with a 75μm mesh brass. A porous disk was placed above the sample and finally, the top plate of the permeameter with the incorporated spring was pressed down on the acrylic cell and attached. The specimen was slowly saturated from the bottom upward by running de-aired water through the sample for some time, till no air bubbles were observed flowing through the pipe. After the saturation was completed, a number of flow discharges for different hydraulic gradient were measured. The measurements were repeated three times at each value of hydraulic gradient.

Figure 5-4 Set up of the permeability test using the soil sample

5.6 Results

Two tests were carried out. The first was conducted on gradation PSD11-up using glass particles and the hydrocarbon oil. The second, on gradation PSD11 using soil particles. The test conditions are reported in Table 5-1. Figure 5-5 shows the outcomes of the tests together with the plots representing the predicted values estimated with the semi-empirical Kozeny-Carman equation (see Equation 5.6). In the calculation, the factors γ, μ, e are known, whereas the terms S_o and $C_{K\text{-}C}$ have to be estimated. The parameters assumed in the calculation for both the particles size distributions investigated are reported in Table 5-2.

Table 5-1 Characteristics of the test specimen

Gradations	Material	A (cm^2)	H (cm)	e	W (g)
PDSD11-up	glass	410.43	30.60	0.62	17253.9
PDSD11-up	soil	45.36	23.43	0.57	1797.1

A, cross sectional area of the specimen; H, height of the specimen; e, void ratio; W, dry weight of the sample

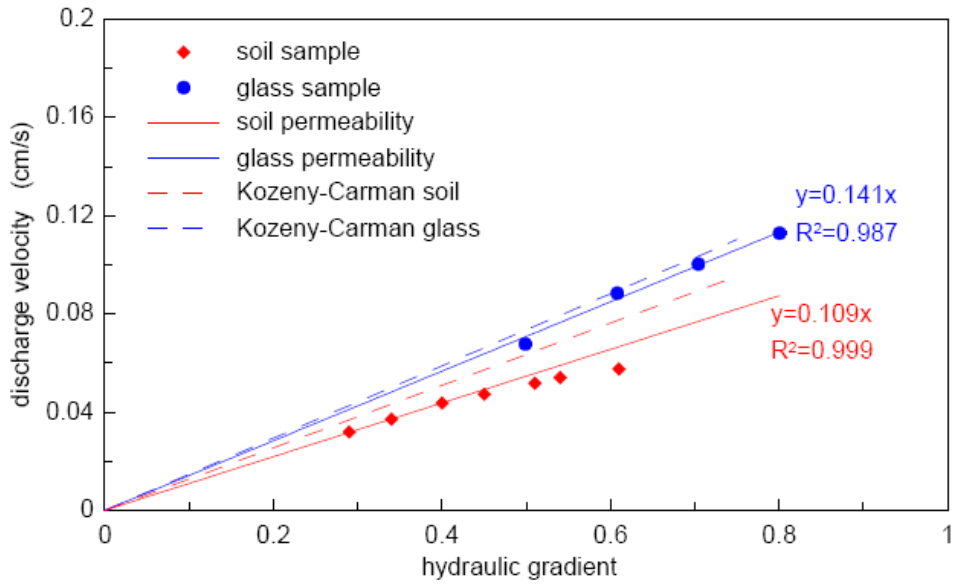

Figure 5-5 results of the head constant permeability test and plots of the predicted values from Kozeny-Carman equation

The results from the constant-head tests give a hydraulic conductivity equal to 1.41×10^{-1} cm/s for the glass sample, while for the soil sample, the hydraulic conductivity is found to be 1.09×10^{-1}cm/s. The permeability of the soil is calculated considering only the first three points of the test, since for value of the hydraulic gradient larger than 0.4, the flow enters the transitional regime as emphasized by the departure from linearity of the flow velocity-hydraulic gradient relation. The temperature of the fluids during the tests was T=23°C for the oil and T=18°C for the water. For comparison purpose, the permeability is converted to a standard temperature (k_2), by the expression:

$$k_2 = \frac{\mu_1}{\mu_2} k_1 \tag{5.8}$$

The conversion of the hydraulic conductivity of the soil sample to a T=23°C, gives a value equal to 1.23×10^{-1} cm/s. Both values of permeability are of the order of 10^{-1} cm/s, which is a reasonable estimate for a well-graded sand. The soil exhibits a slightly lower value, but it has to be noted that the initial void ratio of the tested specimen was smaller than that of the glass sample. Equation (5.6) indicates that k should vary linearly with $e^3/(1+e)$. Using this correction the calculated permeability for the soil sample should be 1.46×10^{-1} cm/s that is a little higher than that of the glass sample (about 3% higher).

The Kozeny-Carman equation gives a good estimate of the permeability for both samples. The predicted values are higher than those observed, but of the same order of magnitude. However, the results of the head-constant tests may underestimate the effective value of the permeability since the degree of saturation of the samples could be slightly less than 100%. Before the tests, the specimens were evacuated of air and saturated under vacuum. In addition, the saturation of the soil sample was achieved using de-aired water. However, during the test the fluid employed was tap-water for the soil, and oil for the glass. Some air bubbles may have been present in these fluids, decreasing the degree of saturation of the samples.

Despite these possible effects, the good agreement between the observed and predicted values, show that the scaling used is applicable.

Table 5-2 Adopted parameter values in Kozeny-Carman equation and predicted permeability value

	Material	D_{eff} (cm)	SF	γ_p/μ $(cms)^{-1}$	$C_{K\text{-}C}$	e	k (cm/s)
PDSD11-up	glass	0.219	7.7	6.13×10^3 (at 25°C)	5	0.62	0.146
PDSD11-up	soil	0.0551	7.4	9.29×10^4 (at 18°C)	5	0.58	0.127

D_{eff}, effective diameter; SF, shape factor; γ_p, unit weight of the permeant; μ, dynamic viscosity of the permeant; e, void ratio; k, predicted permeability value

Chapter 6

Optical investigations through a flowing granular material

6.1 Introduction

The goal of this chapter is to describe the results and to highlight the most relevant features of a first series of experiments carried out using the artificial granular mixture (i.e glass particles and hydrocarbon oil) and the optical technique described in chapter 4. The collected data has been analysed and compared to those obtained in similar tests accomplished using natural materials (i.e. soil and water), presented in chapter 2.

Section 6.1 illustrates the test conditions adopted for the experiments whose results are reported in Section 6.3, focusing on the deposit morphology and velocities of the front. In Section 6.4 the preliminary results of an ongoing image processing using the GeoPIV software are presented.

6.2 Test conditions

Three particle size distributions, based on the gradation curves adopted in the work described in Section 3.2, were prepared. In particular, taking as the prototype reference PSD11, a gradation curve named PSD11-up, was obtained by scaling up the size of the particles four times. In order to investigate the influence of the coefficient of uniformity, C_U, on the mobility of the artificial mixture, other two particles gradations, a uniform one, PSD16-up, and a well graded one, PSD9-mod, were created at the same D_{50}, as shown in Figure 6-1. The reference particle size distribution for the uniform gradation is PSD16, while for the well graded gradation, PSD9-mod, there is not an exact prototype already tested using natural soil. In principle, the prototype

should be PSD9, but this would lead to a mixture comprising an approximately 5% of particles with size from 50mm to 75mm. Due to the physical dimensions of the rectangular exit section of the release tank (139mm in width and 100mm in length), and the width of the flume, i.e. 180mm, even few grains of such size could create jamming during the experiment. Hence, it was decided to use a particle size distribution matching the scaled up PSD9, except for the upper part of the gradation curve, where the size of the solid grains was limited to 50mm. In Table 6-1, the experimental conditions are reported while Figure 6-1 shows the particle size distributions used in the tests compared to the corresponding prototype curves.

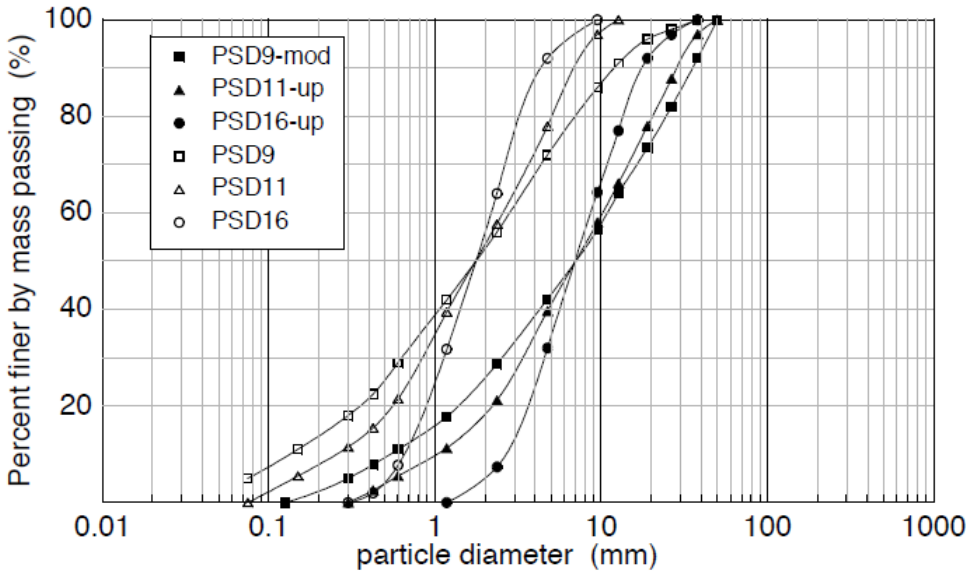

Figure 6-1 Particle size distributions used in the test and the corresponding prototype curves

Table 6-1 Experimental conditions

Particle Size Distribution	C_U	C_Z	D_{90} (mm)	D_{50} (mm)	D_{10} (mm)	Number of tests	volumetric sediment concentration
PSD9-mod	20.2	1.1	35.5	7.1	0.54	2	0.57
PSD11-up	9.8	1.1	28.7	7.1	1.1	2	0.57
PSD16-up	3.3	0.9	17.6	7.1	2.7	2	0.57

6.3 Experimental results

All the tests were performed following the procedure described in Section 4.7. The high-speed camera recorded the images of the flows along a laser illuminated longitudinal plane located at a distance of 3.5cm from the sidewall and passing through a slit in the bottom of the flume cut between 11cm and 41 cm from the exit point to the deposition area. The frame rate of the movie was set at 1100 fps. For all three particle distributions tested, a brief description of the observed behaviour is reported below.

- PSD9-mod

  These are the most well graded particle distributions tested. The flow behaviour in both the runs behaved in a similar manner, although the runouts were not identical (see Figure 6-6). The flows were thin and elongated. A few bouncing grains preceded the arrival of the front. The snout, comprising coarse particles, had a velocity at the control section larger than 2m/s. Both the front and the body had approximately the same height, i.e. around 2.5÷3cm. The depth at the tail was around 1 cm. Figure 6-2 shows images of the different parts of the flow. The flow segregated during the motion along the length, with most of the coarsest particles concentrated at the front. Through the depth, the segregation was not so evident, due the small thickness of the flow in comparison to the average size of the grains. Nevertheless, the tendency of the coarse particles to assume a position closer to the free surface is visible, many of them (mostly the biggest) appearing to “float” on it. During the flow, frequent collisions between the particles and the bed could be observed. The upward movements after these impacts sometimes made the particles bounce even outside the free surface.

- PSD11-up

  These tests are characterized by a well-graded solid material. Similarly to PSD9-mod, the experiments led to similar flow behaviours. Again, a coarse front following a few bouncing particles was recognizable. The average velocity of the snout was lower than that of the most well-graded material (i.e. slightly less than 2m/s), whereas the thickness of the flow was larger. The front and the following body of the mixture were 4÷5 cm thick, while the tail was around 2cm. The segregation of the particles was evident in both directions, along the length of the flow and its depth. During the motion, the particles exhibited fewer collisions with the bed and between each other in comparison to the PSD9-mod. Some images of the test are shown in Figure 6-3.

- PSD16-up

  These experiments employed a uniform particle size distribution. The flow behaviour resulted in behaviour that was quite different from those obtained with the well-graded mixtures. The front was very thick, larger than the height of the image frame as recorded by the high-speed camera (nearly 6cm). Given the shape of the flow, a thickness of the front of around 7cm can be estimated. The front was unsaturated, highly concentrated and with a significant number of air bubbles. Therefore, it was impossible to obtain clear images from this part of the flow. Also, the penetration of the laser within the flow close to the front was partially prevented by the high concentration of the particles and the large thickness of the medium, so that the resulting images were blurred and not clear. However, the quality of the images improved significantly towards the tail, where the solids concentration progressively decreased. Images of the flow are shown in Figure 6-4. The average velocity of the snout was the lowest among the tests at approximately 1.5 m/s. The whole flow moved as a bulk surge with a short length. The thickness of the tail was around 2 cm. The degree of segregation appeared to be lower, with coarse particles being present also in the body of the surge, dispersed almost uniformly over the height of the flow.

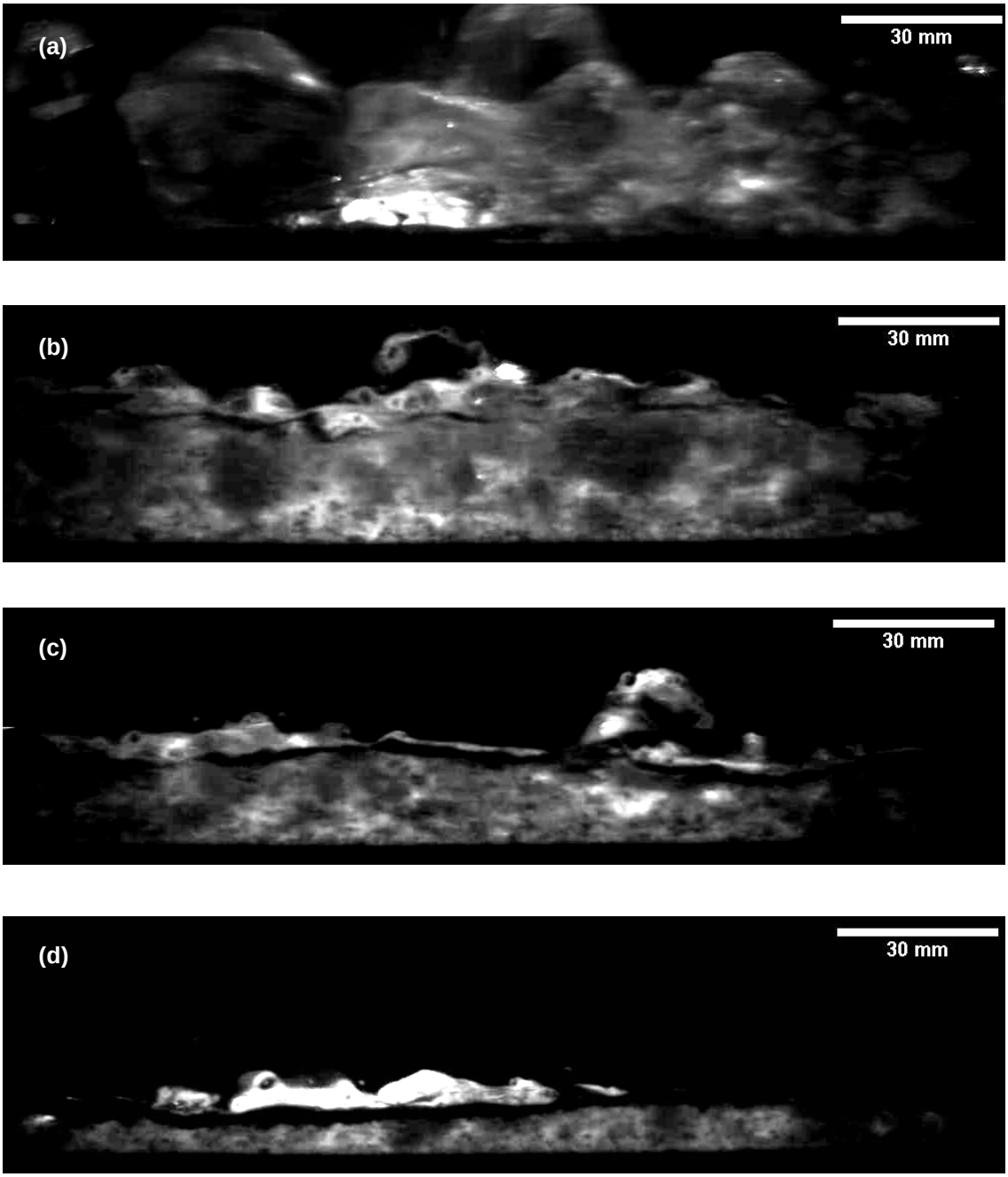

Figure 6-2 Digital images of the test using PSD9-mod. The flow is proceeding from left to right
(a) During arrival of the flow front;
(b) In the core of the flow;
(c) In the tail of the flow;
(d) At the end of the flow

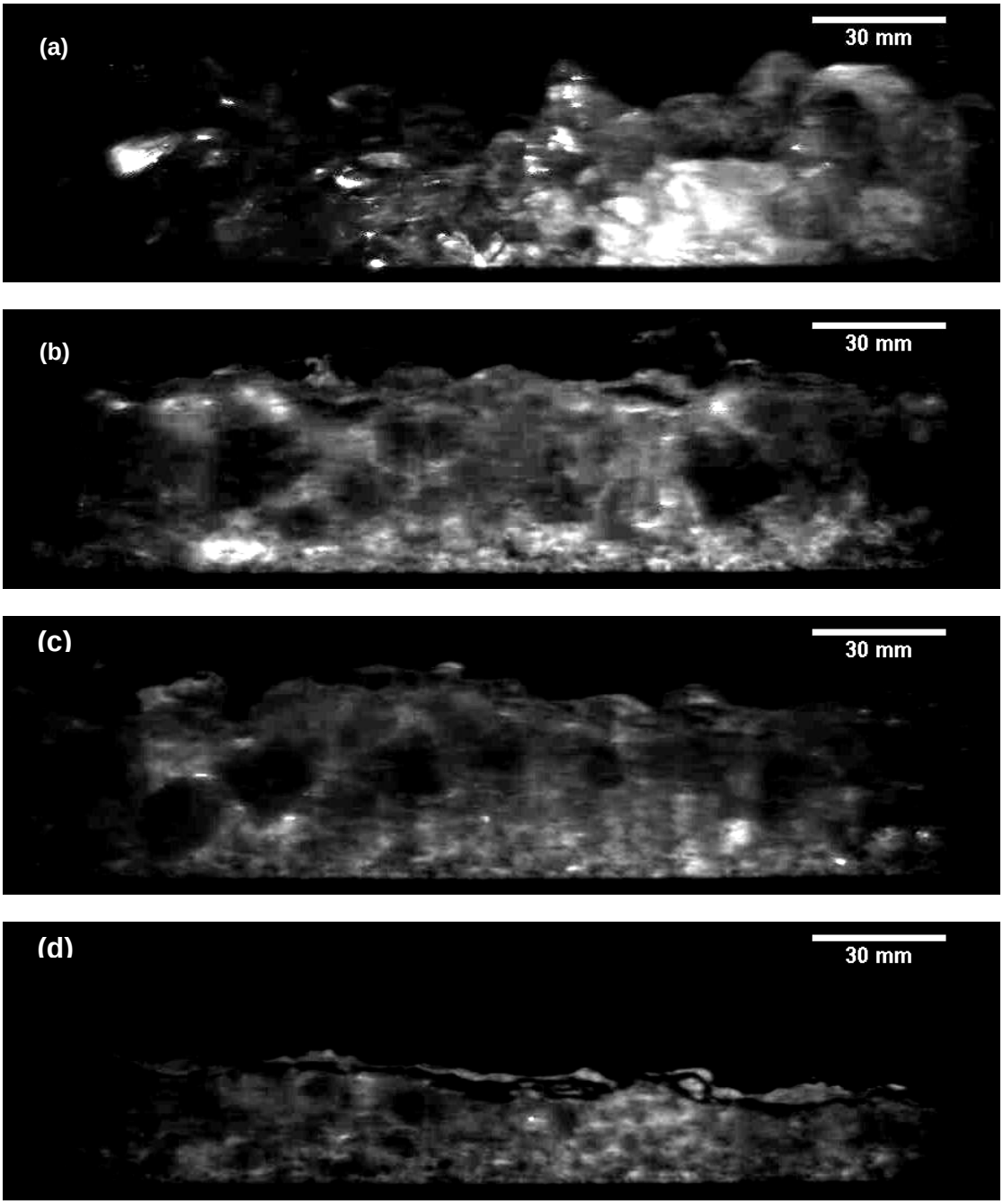

Figure 6-3 Digital images of the test using PSD11-upscaled. The flow is proceeding from left to right
(a) During arrival of the flow front;
(b) In the body immediately after the front;
(c) In the core of the flow;
(d) In the tail

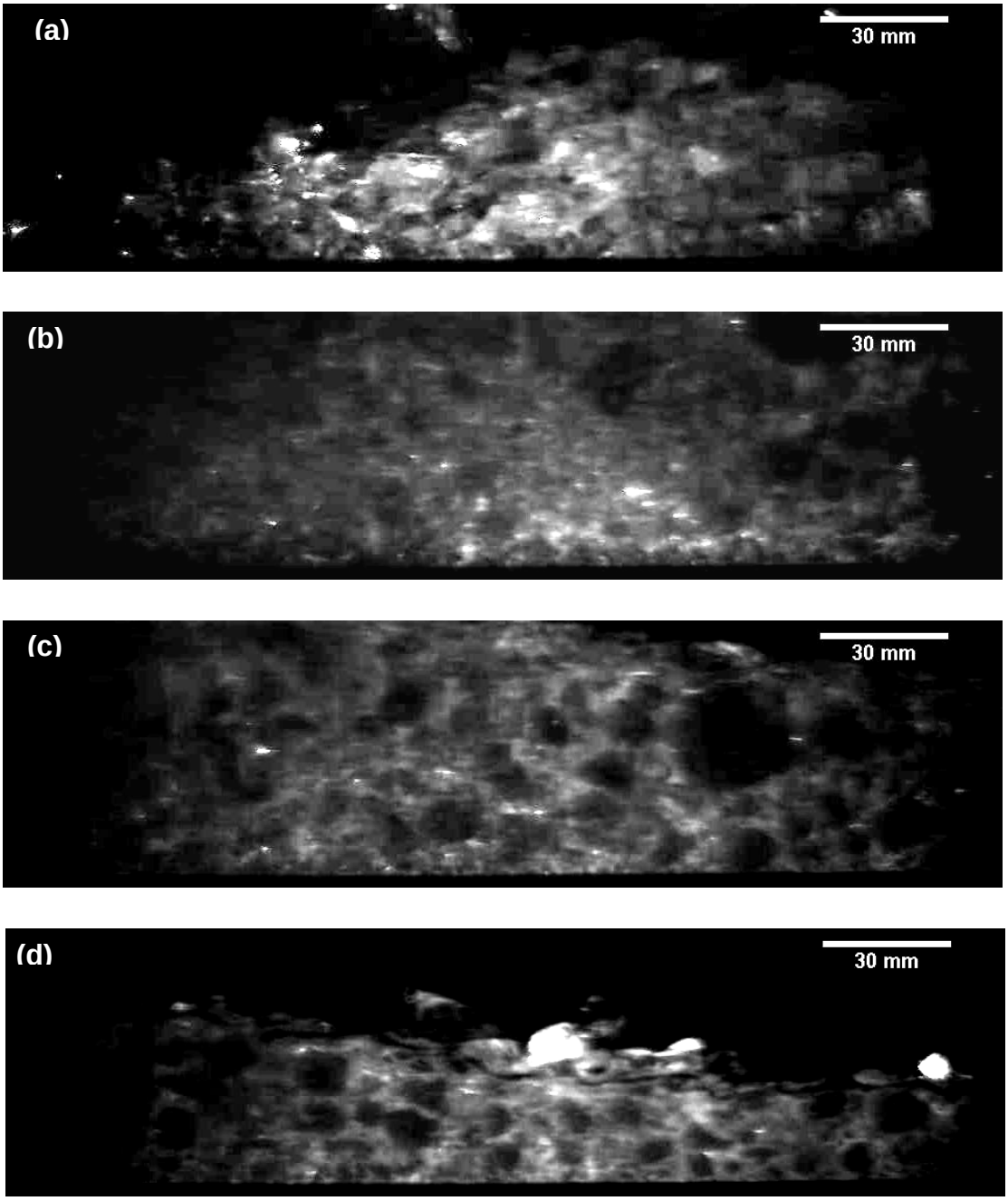

Figure 6-4 Digital images of the test using PSD16-upscaled. The flow is proceeding from left to right
(a) During arrival of the flow front;
(b) In the body immediately after the front;
(c) In the core of the flow;
(d) In the tail

6.3.1 Deposit morphology

Experimental flows deposited their sediments rapidly beyond the flume mouth on the horizontal (0°) varnished wooden surface of the deposition are a.

Analysis of experimental deposits included measuring their shape and depth distribution, and collection of sediment samples at the front and at the centre of the deposit, to examine the gradation of the material. Figure 6-5 shows the typical shapes of the runout fans for the tests with different C_U. Figure 6-6 depicts the deposit fans of all the tests performed. The runout length shows the same tendency observed in the experiments performed with the mixture of soil and water, i.e. the runout increases as C_U increases. The deposits produced by the tests using the most well graded particle size distributions have the largest runout and the smallest width. The thickness of these deposits was usually less than 20mm, except where the biggest particles deposited. The large difference in the slope of the flume and the flat runout area led to an accumulation of the sediments close to the to the exit point of the flume, where the height of the deposit increases. Some material was found also along the final part of the flume in correspondence to the roughened bed, i.e approximately 1.0 m before the mouth of the channel. The shape of the runout for the tests with PSD11-up was shorter and slightly wider. Again, some material deposited in the flume but the deposition started further down, around half meter before the exit point to the flat surface. The deposit was thicker: in general less than 30mm, but with a depth around 40-45mm close to the mouth of the flume. The deposits of the PSD16-up tests were the shortest and they had a circular shape. The thicknesses of the deposits were commonly greater than those of the PSD11-up test, approximately 35mm thick. The deposition of the material started 30cm before the end of the flume, but, in contrast to the previous tests, the layers of sediments found in the channel were thinner than 25mm. In this case, an accumulation of the material close to the end of the channel, observed in the previous tests, was not found. Instead, the thickness was larger in the centre of the fan and decreased progressively towards the margins.

The segregation features observed in the flows moving down the channel were reflected by the deposits, with the leading front, consisting of relatively well-sorted coarse particles, being shunted to the deposit margins. Figure 6-8 shows the typical particle size distributions obtained from the samples collected at the front and at the centre of the deposits, together with the gradation curve of the material sampled from the flume. The well-graded materials, PSD11-up and PSD9-mod, led to the largest overall segregation during flow and deposition, as it can be inferred from the particle size distributions of their lobate samples. The materials at the deposit

fronts have a uniform coarse distribution with a significant increase in the size of the mean diameter, in comparison to the source material. This characteristic is not displayed from the test with PSD16-up where the lobate sample is relatively less segregated in comparison to the source particle distribution. On the contrary, in all the tests, the gradations of the centre sediments were not substantially different from the composition of the material before testing. In addition, the particle size distributions of the sample collected in the flume confirmed the tendency of the well-graded mixture to segregate during the flow, while a low degree of segregation occurred during the uniform material tests.

Figure 6-7 presents the length of the runouts, normalized to the longest observed, as a function of the coefficient of uniformity. Data corresponding to the test performed with both the artificial mixture and the natural material are shown.

Figure 6-5 Test depositions for PSDs with different C_U: a) PSD9-mod (C_U=20.2); b) PSD11-up (C_U=9.8); c) PSD16-up (C_U=3.3)

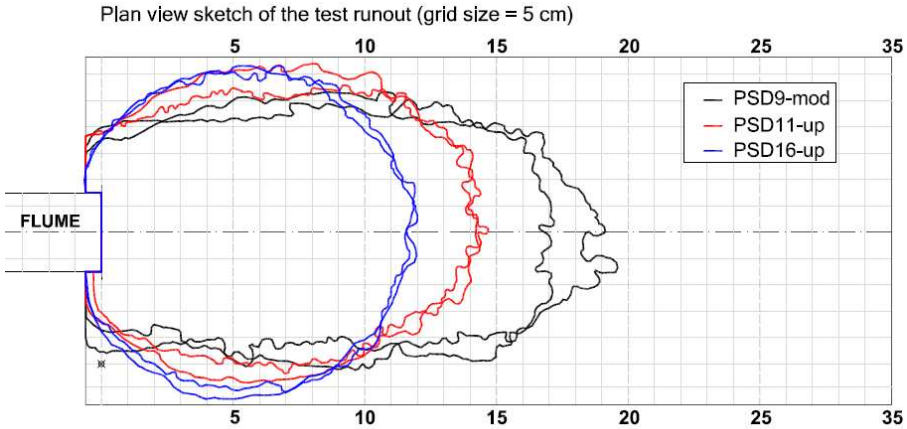

Figure 6-6 Shape and spreading of the deposition fans for the tests with oil-glass mixtures

The normalized runout shows the same tendency both for glass and soil mixture. The length increasing with increasing coefficient of uniformity, C_U. Consistent results are obtained for well graded materials. Uniform gradations exhibit a clear difference on the extent of the runout, which resulted to be relatively longer for the glass. This may be due to the influence of the suction developing in the soil mixture comprising of soild particles four times smaller than those of glass. As described in Section 3.3.3 the suction in PSD16 is not so relevant in comparison to the net effective stress, but its presence may affect the final length of the runout leading to the observed results.

In the mixture comprised of glass particles suction cannot develop due to the large size of the grains and the lower value of the surface tension with respect to the water (for the water $T=7.2x10^{-5}$ kN/m and for the oil $T= 2.9x10^{-5}$ kN/m, at 25°C)

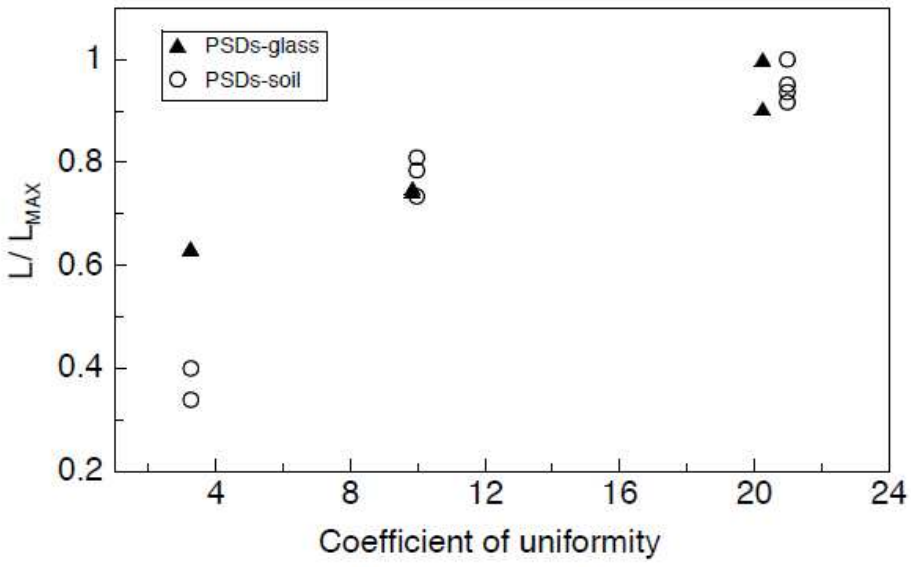

Figure 6-7 Normalized runout versus coefficient of uniformity

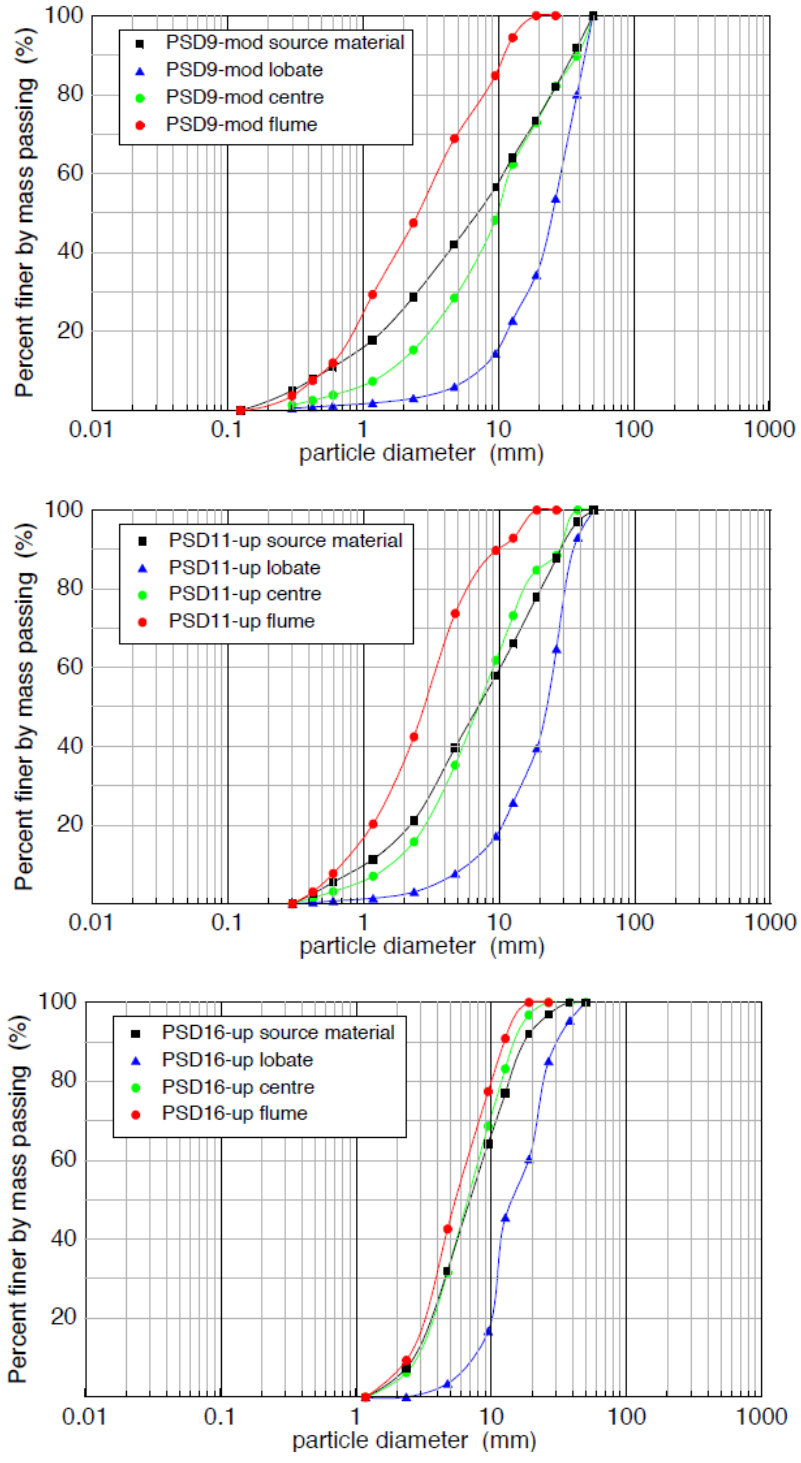

Figure 6-8 Typical particle size distributions for the lobate, centre and flume samples collected from the test deposits

6.3.2 Front velocity

Figure 6-9 shows the normalized runout against the square velocity of the front for both soil and glass tests. The normalized runout of the glass material appears to depend linearly from the square velocity value at a given D_{50}. The points corresponding to the uniform gradations (PSD16-up) diverge slightly from this trend. However due to the limited number of experiments performed, this observation needs to be verified. As obtained for the runout-C_U relation (see Section 6.3.1) the well graded mixtures of the two different materials display similar results. For the uniform gradations, comparable square velocity values are measured, but with a corresponding normalized runout for the glass mixture significantly larger than that of the soil. Further investigation is required to understand this behaviour.

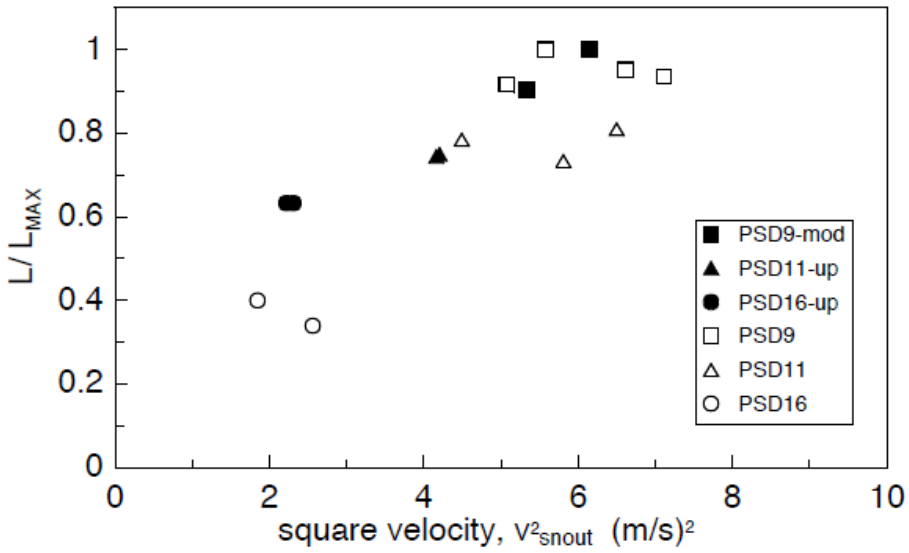

Figure 6-9 Normalized runout against square velocity of the front

6.4 Image analysis

In this section, we describe the methodology adopted for the image post-processing analysis, based on the adoption of the GeoPIV software and the results obtained on some of the performed tests.

6.4.1 The Particle Image Velocimetry technique

In order to measure the flow field characteristics, e.g. the velocity of the recorded flow sections, quantitative imaging (QI) techniques have been adopted. QI techniques are a general class of

optically based laboratory measurement techniques originally developed in the field of fluid mechanics.

QI can be categorized in several fundamentally different types of technique: flows seeded with discrete particles, flows seeded with continuous tracers (fluorescent dye) and unseeded flows. The former are usually employed for the determination of velocity while the other two are more often used to determine a scalar field quantity, such as density differences or concentration.

In the case of particle based QI technique, the most popular techniques are:

- Particle Streak Velocimetry (PSV): the image exposure time is long compared to the time a particle occupies a point in space. The result is images showing the particle streaks.
- Laser Speckle Velocimetry (LSV): the seeding density is so high that the image captures mainly overlapping and interfering particle images, which represent a sort of texture or speckle field. The velocity is obtained by correlating the speckle pattern.
- Particle Image Velocimetry (PIV): this term indicates a broad class of discrete particle based techniques, which will be described in more detail later in this section.
- Particle Tracking Velocimetry (PTV): a class of techniques where the seeding density is sufficiently low that an image captures mainly non-overlapping or interfering particles, which are used to track the motion over known times.

The common principle for all particle-based approaches is that the instantaneous flow velocities can be estimated by measuring the position of the tracer particles, suspended in the fluid, at successive times. The velocity field is generally determined against a reference grid, averaging the velocity of the tracers falling in each mesh cell (patch).

The Particle Image Velocimetry (PIV) approach was chosen for the analysis of the flow characteristic of the performed laboratory tests. PIV is a velocity-measuring technique that was originally developed in the field of experimental fluid mechanics (Adrian, 1991). The technique consists of analyzing the images of the flow and dividing each image into a mesh of test patches. The displacement vector of each patch during a given time interval is found by locating the peak of the autocorrelation function of each patch. This indicates that the two images of each seeding particle are overlying each other. A modified approach has been used to implement PIV in geotechnical testing, for which natural particles have their own texture in the form of different-coloured grains.

The PIV principles have been implemented as a MatLab (http://www.mathworks.com/) module by D.J. White & W.A. Take (2002), in a manner suited to geotechnical testing. The module is known as GeoPIV and the resulting software is used for the image analysis work presented in the coming sections. According to the GeoPIV approach, the displacement between a pair of

digital images is measured as sketched in Figure 6.10. The first image is divided into a grid of test patches. Each test patch consists of a sample of the image matrix of size L x L pixels. The displacement of the test patch between images 1 and 2 is calculated selecting a proper search patch from the second image. This search patch extends beyond the test patch by a pre-set distance, in both coordinate directions, defining the zone in which the test patch is to be searched for. The cross-correlation of the test and the search patches is evaluated and properly normalized. In order to reduce the computational requirement, the correlation operations are conducted in the frequency domain by taking the fast Fourier transform (FFT) of each patch and following the convolution theorem. The highest peak in the resulting normalised correlation plane indicates the displacement vector of the test patch.

The basic GeoPIV algorithm has been adapted by W.A. Take (private collaboration) to the needs the present work, by supporting a static mesh, whose position and geometry is fixed in the image and through which particles flow. The displacements are calculated at subsequent (close) time steps, providing an estimate of the instantaneous velocity field at the mesh location. Furthermore, specific MatLab code has been written in order to perform the necessary statistical analysis.

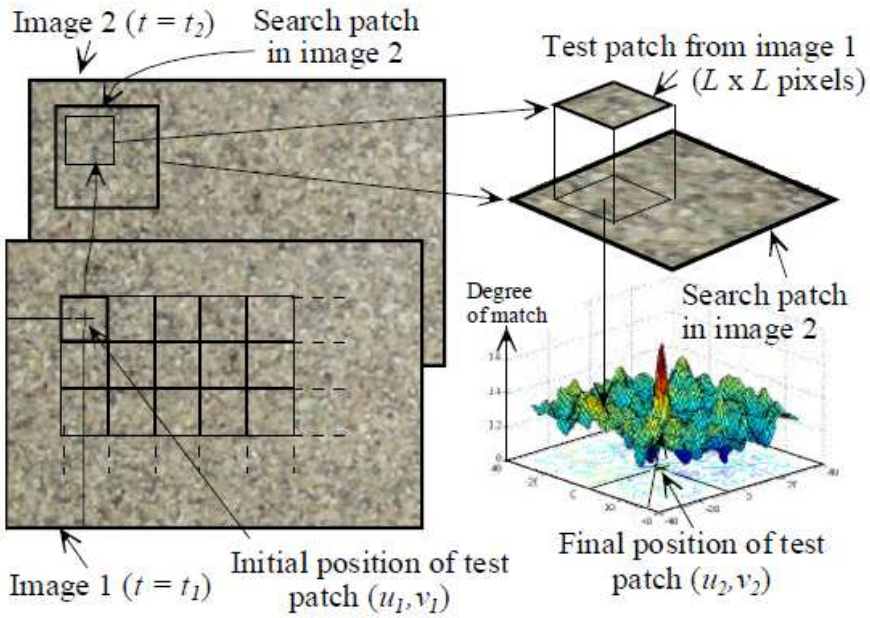

Figure 6-10 Principle of PIV analysis

6.4.2 Velocity field inside the flow

Three experiments, PSD11-up-b, PSD16-up-b and PSD9-mod-b, one for each of the different particle size distributions, are analyzed using the GeoPIV software. The analysis starts from the part of the flow immediately following the front, where fully saturated conditions make the PLF technique effective, emphasizing the solid particles as black spots against a bright background.
Velocity fields are estimated at regular time intervals (60/90 frames, corresponding to 0.054/0.081 seconds), by defining static meshes covering the whole height of the flow and calculating the displacements of the mesh patches between two successive frames, following the PIV procedure described above. The first mesh is placed for all the tests immediately after the unsaturated coarse front. Square patches with two different sizes, 16 or 32 pixels (1/16 or 1/8 of the image height), were used. The former allows a higher spatial resolution to be obtained, and hence more detailed, although more noisy, results. The latter leads to more precise results at the expense of resolution. The patches overlap in the vertical direction at spacing of half the patch size (see Figure 6-11). Each mesh consists of a single column of patches. For each mesh, the velocity is calculated as the mean of the instantaneous velocities estimated over 30 successive frames (this corresponds to a time step of 0.027 seconds). Figure 6-12 shows an example of the distribution of the 30 velocity estimates produced at each patch of a mesh both for the x and the y components of the velocity. The standard deviation (*std* - see equation 6.2) is calculated for each velocity estimate and values which fall outside a proper confidence interval are neglected and the mean recalculated accordingly. For 32 pixels patches (hereafter called 32pix), the confidence interval is set to 3*s*, while for 16 pixels patches (16pix) it is set to *s*, in order to cope with the large scattering associated to the corresponding data.
The y component of the velocity results to be typically at least one order of magnitude smaller than the x component. Therefore, its contribute is neglected in the analysis presented in the next sections

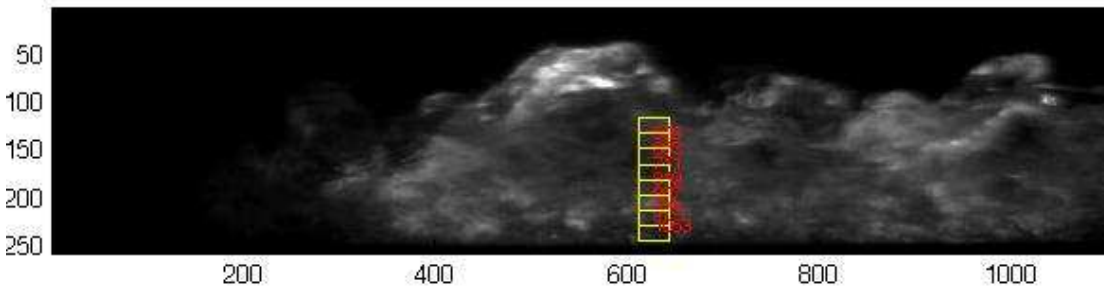

Figure 6-11 Example of static GeoPIV mesh

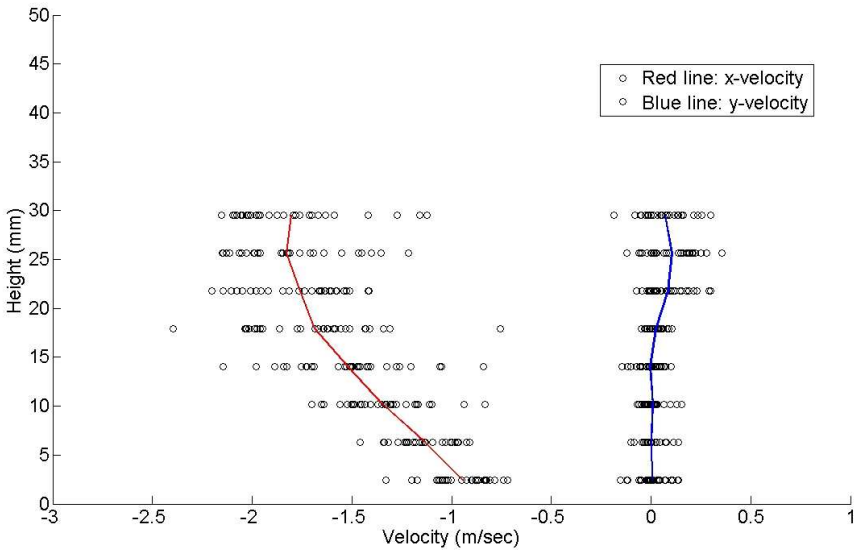

Figure 6-12 Example of velocity estimate resulting from GeoPIV mesh

6.4.3 Mean velocities

In order to analyze the overall behaviour of the velocity field in the three tests, the mean velocity u_j at mesh *j*, is calculated as:

$$u_i = \frac{1}{N_j}\sum_{i=1}^{N_j} v_{i,j} \tag{6.1}$$

where N_j is the number of patches of the j-th mesh and $v_{i,j}$ is the velocity estimate at patch *i* of mesh *j*. For each u_j the corresponding standard deviation (std_j) is calculated:

$$std^2{}_j = \frac{1}{N_j - 1}\sum_{i=1}^{i=N_j} \left(v_{i,j} - u_j\right)^2 \tag{6.1}$$

The standard deviation expresses the dispersion of the velocities of the j-th mesh around the average. The resulting mean velocities are shown in Figure 6-13 as functions of time. The initial time corresponds to the frame of the first mesh (just after the front)

In Figure 6-14 the estimates of the height of the flows are shown, obtained by plotting the position of the highest patch of each 16pix mesh. Notice that this is just an approximation of the real height, since the meshes do not cover the entire depth of the flow. This is due to the restrictions posed by the software, which fails above the free surface. Therefore, the top patch of the mesh must be set just below the free surface.

It is useful for the discussion that follows, to distinguish between two main regions for each flow. Here such regions are defined as the “body” and the “tail”. For PSD16-up-b, the body is defined as the region that shows both the highest thickness and the largest mean velocity. It can be identified within the interval between 0 and 0.36 seconds. The remaining part of the flow, with decreasing height and velocity, represents the tail. For PSD9-mod-b, the body is the part of the flow which exhibits a high (except for the first two mesh positions) and rather constant thickness. The velocity is high and, although fluctuating, slowly decreases. It can be located between 0 and 0.45 seconds. The tail is initially characterized by a fast decrease of the velocity and of the height of the flow, which progressively becomes gentler. PSD11-up-b is the most difficult to classify. Its thickness and velocity profiles do not show specific behaviours, constantly decreasing with ripples from the beginning. Therefore, it is impossible to identify a clear feature separating the body from the tail. Hence, the transition is assumed to be after 0.45 seconds, when the height of the flow starts decreasing clearly.

Comparing the tests, the most uniform material, PSD16-up-b, moves with the lowest velocity at any time, while the well graded materials PSD11-up-b and PSD9-mod-b exhibit comparable higher velocities in the body. At the end of the body, the velocity of PSD9-mod-b appears to be slightly higher. However, the tail velocity of PSD11-up-b decreases less rapidly, leading to highest values of the velocity in the last part of the flow. It is interesting to note that PSD16-up-b, which has the lowest velocity, displays also the shortest runout (see Section 6.3.1). However, the well graded distribution PSD11-up-b, despite its high velocity in both at the body, where it is comparable to PSD9-mod-b, and in the tail, where it is the highest, leads to a shorter runout compared to the most well graded material (PSD9).

The height profiles show that PSD16-up-b moves as a bulky surge, with a thickness significantly larger than the other two particle size distributions. The heights of the flow drops suddenly at the beginning of the tail decreasing from about 5mm to less than 10 mm. The well graded materials display a much lower depth and similar profiles, PSD11-up-b being a little thicker. The decrease of the height from the body to the tail occurs smoothly, reaching comparable heights at the end.

A particular feature of the PSD9-mod-b velocity curve is represented by the large ripple present in its body. Such ripples are not the result of numerical noise. Indeed, they are related to the high concentration of big particles. These particles move faster than the surrounding matrix, but preferentially at the surface of the flow, without perturbing its motion. However, the largest particles, whose size are comparable with that of the flow height (see Figure 6-15), occupy a significant part of the available space, pushing and accelerating the material immediately in

front of them. This is highlighted by measuring the velocity profiles with meshes placed just before the big particles.

The faster motion of the big particles on the flow surface is in agreement with the mechanism suggested by Iverson (2005) for the development of grain segregation in debris flows (see Figure 6-16

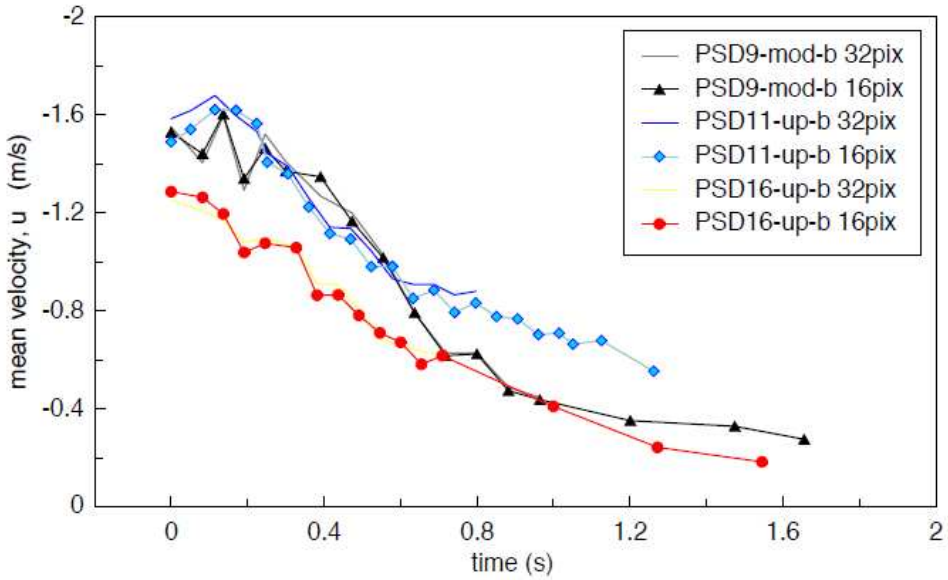

Figure 6-13 Mean velocity versus time

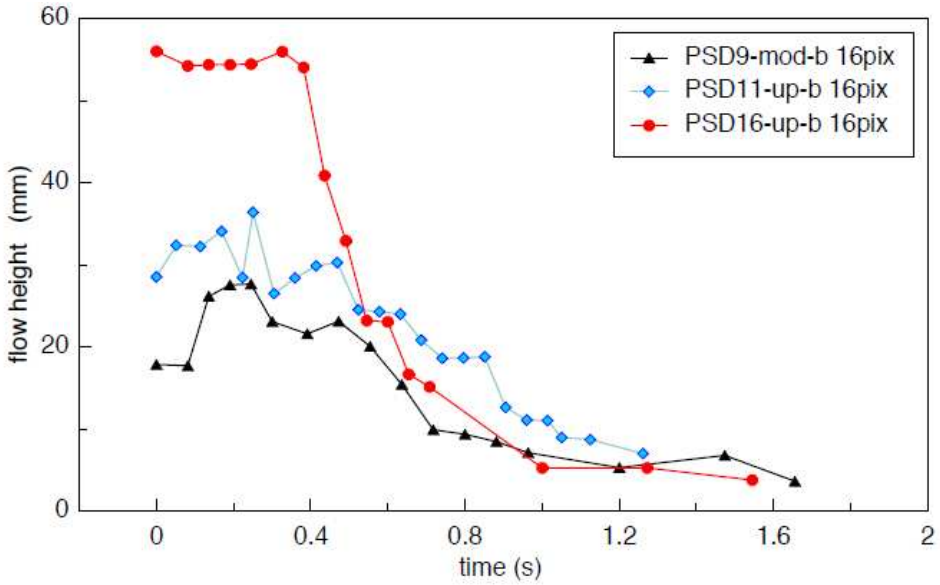

Figure 6-14 Position of the highest patch of each mesh versus time

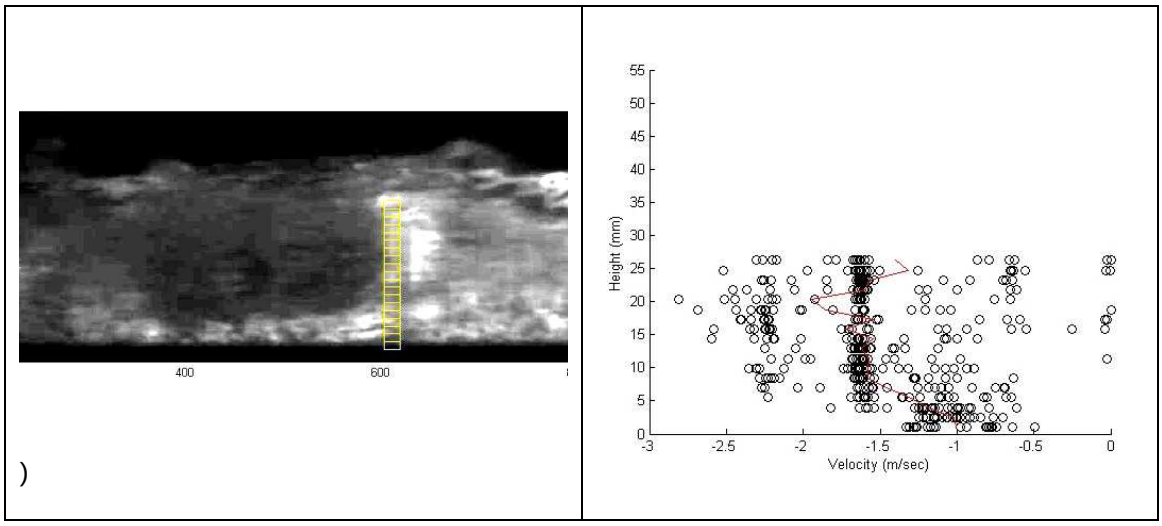

Figure 6-15 Example of big particle moving in the flow (on the left) and velocity estimated during the motion of the particle through the static mesh

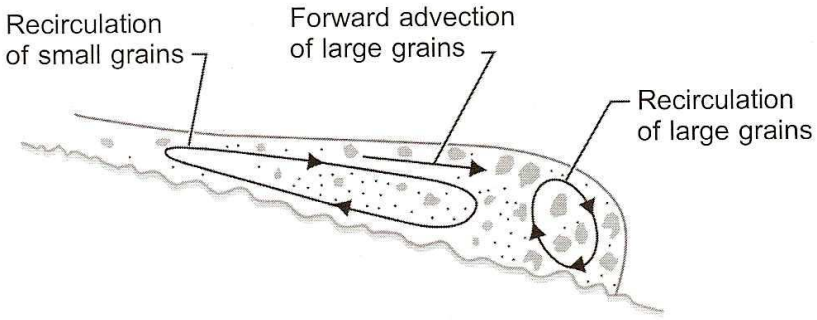

Figure 6-16 Sketch of grain trajectories and resulting grain-size segregation in a debris-flow surge (from Iverson, 2005)

6.4.4 Velocity profiles

A few examples of the calculated velocity profiles are presented in Figure 6-17, Figure 6-18 and Figure 6-19. For each particle size distribution, three profiles from the body and three from the tail are shown. The mean values and the corresponding standard errors are plotted for 16pix (blue lines) meshes, while the red lines represent the results for the 32pix meshes. The two different meshes always lead to compatible results, the 16pix giving more details and describing larger ranges and the 32pix providing smoother and more precise results.

All the results present a slip velocity at the base, in most cases of about 0.5 m/s, probably due to the relatively low friction provided by the rough material which covers the bed of the flume. The two well-graded materials exhibit similar profiles, with the same velocities at the body. Consequently, since the height of the PSD9-mod-b flow is lower than that of PSD11-up-b, the shear rate, defined as

$$\dot{\gamma} = \frac{v}{h} \tag{6.1}$$

where v is the velocity and h is the height of the flow, is larger for the PSD9-mod-b.

The body of the PSD16-up-b gradation, appears to move with less shearing, since the velocity is lower, while the height is larger.

In all cases, the flows appear to have large shearing toward the base, while they tend to move with a more constant velocity toward the surface. This tendency is more pronounced for PSD16-up-b, which seems to move as a plug in the upper part of the flow.

The vertical component of the velocity has been calculated as well for all flows. However, its values are found to be negligible always with respect to the main horizontal component, which drives the motion of the flow.

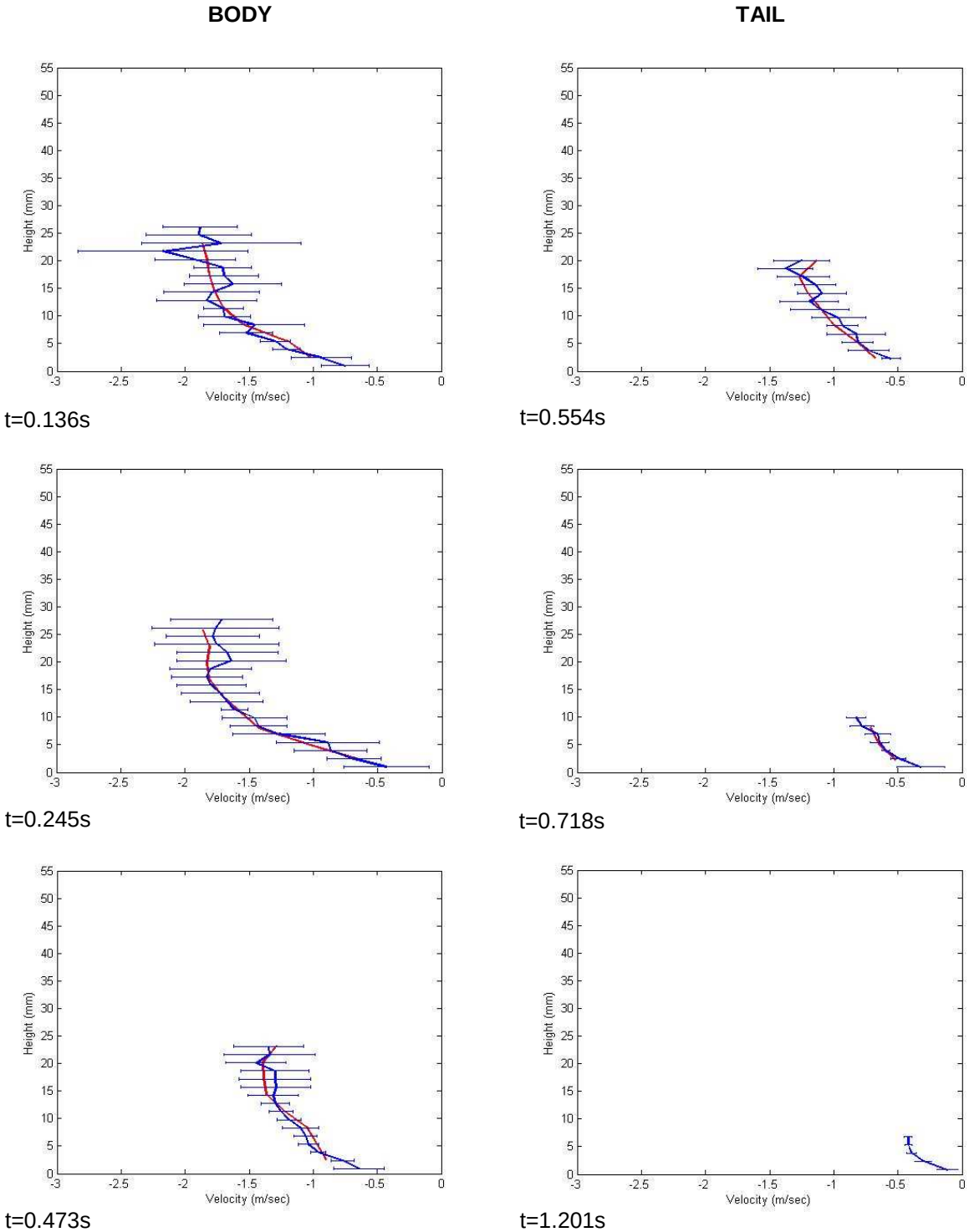

Figure 6-17 Velocity profile for PSD9mod-b at different times for 16pix meshes (blue line) with the corresponding error bars. The 32pix velocity is overlapped for comparison. On the left results for the body, on the right for the tail

BODY **TAIL**

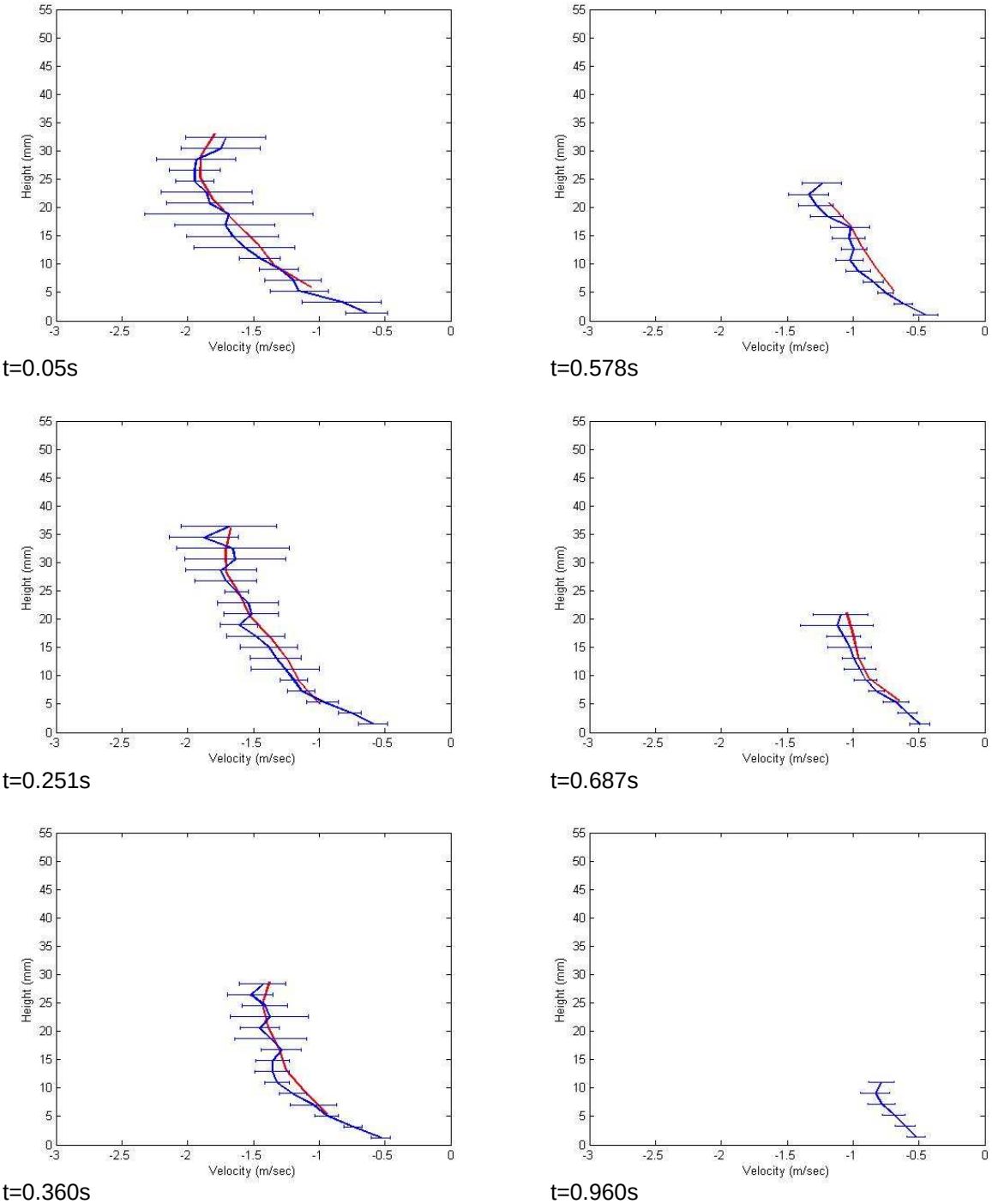

Figure 6-18 Velocity profile for PSD11-up-b at different times for 16pix meshes (blue line) with the corresponding error bars. The 32pix velocity is overlapped for comparison. On the left results for the body, on the right for the tail

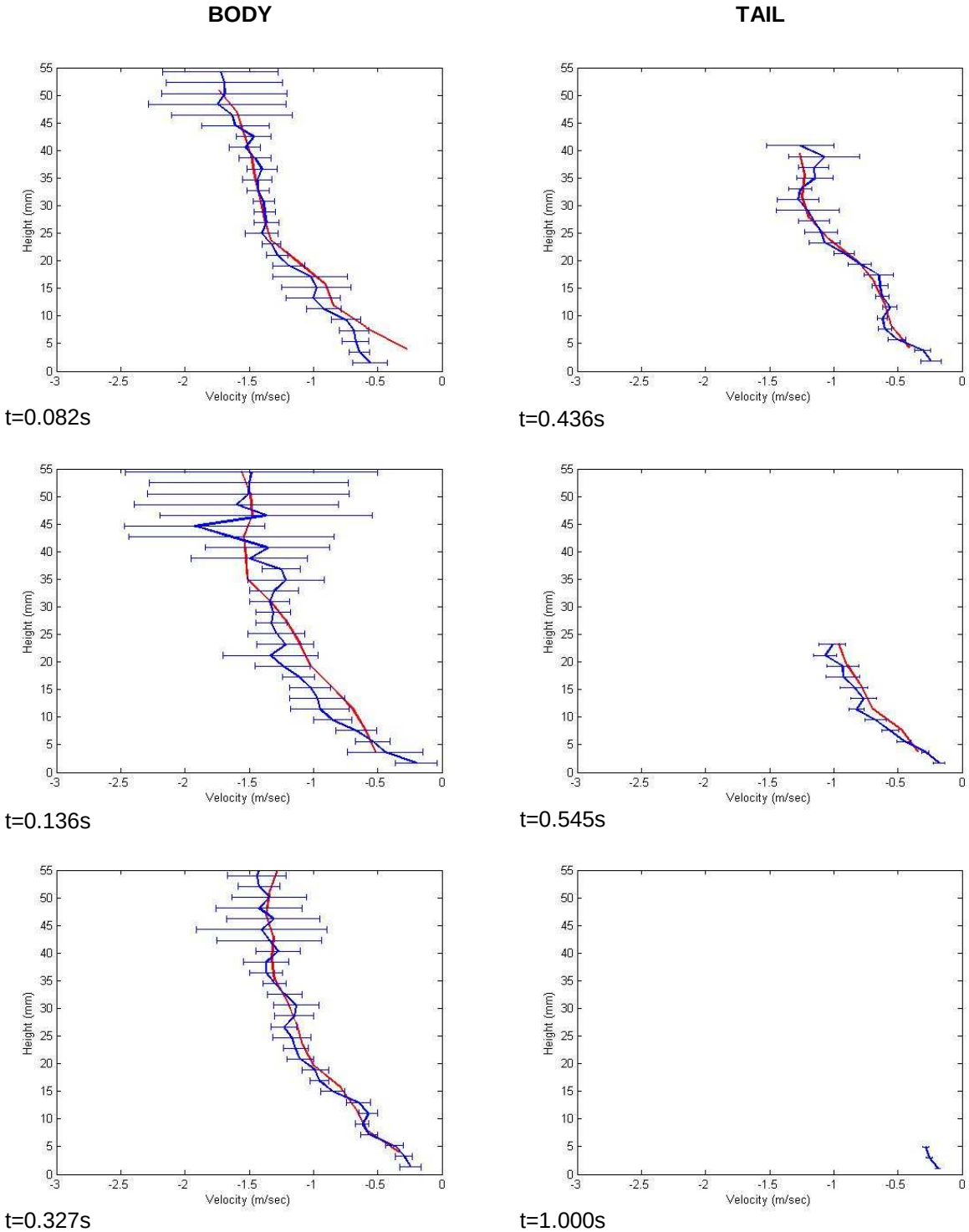

Figure 6-19 Velocity profile for PSD16-up-b at different times for 16pix meshes (blue line) with the corresponding error bars. The 32pix velocity is overlapped for comparison. On the left results for the body, on the right for the tail

6.5 Discussion

The results of a series of preliminary small scale flume tests using the novel method based on Planar Laser Induced Fluorescence and refractive index matching (see Chapter 4), have been presented in this chapter.

The high speed images of the internal illuminated section of the flow (taken at a distance of 3.5cm from the channel sidewall) show a good quality and high resolution. Most of the coarser particles within the flow can be distinguished and their motion and interparticle interactions can be easily observed. It is not possible to use PLIF at the unsaturated coarse front developing at the head of the experimental flows, since there the fluid phase is partially absent. However, individual larger particles can be discerned as illuminated blocks moving down the chute.

The artificial mixture (Duran glass and hydrocarbon oil) exhibits behaviour similar to that displayed by a mixture of soil and water in analogous tests. That is, the runout length increases for higher values of the coefficient of uniformity. The greater speed and larger average runouts are obtained for well-graded mixtures in comparison to uniform graded material. Most important, the well-graded mixtures exhibit morphologic features common to many natural and laboratory debris flow fans, with coarse particles concentrated at the front and at the outermost margins, while the finer material is emplaced at the rear of the fan. The segregation of the particles is clearly visible from the movie where it is possible to observe the accumulation of the coarsest particles at the head of the surge and the big particles at the top of the flow, moving faster than other toward the front.

The quality of the flow images captured by the high speed camera is sufficient for quantitative imaging techniques to be applied. A preliminary analysis has been accomplished using GeoPIV, software based on the Particle Image Velocimetry, approach. Velocity profiles have been calculated for different parts of the flow, from the body, immediately after the unsaturated front, to the tail. The results show that for the uniform materials the flow moves down the flume as a bulk surge, with low velocity, resulting in the shortest runout. The velocity profiles show the presence of a plug toward the free surface. The well graded materials exhibit higher shear rates, due to higher surface velocities and lower thickness. The analysis of the time series of the average velocities shows that well graded distributions have higher velocities than the uniform ones, during all the duration of the events. Furthermore, the two well graded distribution have velocities similar at the body but different for the fronts, higher for the most well graded mixture. Further investigation is required to shed light on this aspect. More generally, the whole data processing procedure must be improved in order to find the best solutions to analyze this novel kind of data.

Conclusions

The present study has focused on the experimental study of saturated granular flows with a specific attention to the implications related to the physical modelling of debris flows. The work dealt with two main activities. The first, aimed at investigating the role of particle size in the flow behaviour of granular materials. The second intended to develop a novel methodology for the analysis of experimental saturated granular flows based on the Planar Laser Induced Fluorescence technique, in a context of high speed movement and in free surface conditions.
An overview of the accomplished research work and a brief summary of the major findings are given below.

The role of particle size in the flow behaviour of saturated granular materials

The first part of the PhD research was instigated by considering that, irrespectively of the peculiar features of the sediments (grain shape and size, texture, density etc.), field evidences show that virtually all debris flows contain a wide particle size distribution (PSD) with sizes ranging from boulders or gravel to silt and clay. Debris flows material generally comprises mostly gravel and sand with a percentage of fines, i.e. silt and clay particles that are less than 10% of the total mass. The typical mean particle size, D_{50}, ranges between 2mm and 200mm and characteristic reported uniformity coefficient values, $C_U = D_{60}/D_{10}$, are of the order of 100-1000. Few previous experimental studies have explicitly considered the influence of the PSD on debris flows behaviour. Typically, experimental flows are characterized by a mean particle size which is necessarily smaller than that found in the field with a relatively uniform PSD (C_U<5). Unsurprisingly, important aspects of their behaviour, such as the effects of flow segregation, cannot be replicated in such tests.

We have therefore undertaken an experimental research to determine if the well-graded nature of debris flow materials is key to their mobility (high speed and long runout). A number of tests using soil with different gradation, i.e. with different C_U, C_Z and D_{50} values, were performed at given moisture content. The particle size distributions used in the tests ranged from uniform to well graded materials, with C_U from 3.3 to 21, and D_{50} varying from 0.52mm to 3.78mm.The apparatus adopted for the tests was a small scale flume with rectangular section kept at a constant slope (24 degrees) for all the run.

The results show that the particle size distribution has a significant effect on the mobility of flowing granular materials. Segregation of particle sizes occurring during the flow motion of well-graded PSDs, results in flows with greater speed and larger average runout in comparison with uniform graded soils. The mean particle size is also found to have an influence on mobility of well-graded materials with flows comprising larger particles producing less mobile flows due to increasing permeability and particle friction. However, D_{50} appears have no influence on the runout of uniform materials.

In addition, for flows comprised of particles smaller than medium-fine sand, viscous effects in well-graded mixtures lead to a reduction of flow mobility with decreasing particle size, whereas effect of suction at the unsaturated front surge in uniform material, can be the reason of their observed shortest runout.

The velocities of the flow fronts have been analyzed. The results show that the runout lengths generally increase with the square velocity of the front but a well defined relationship is difficult to establish. This may be explained by the large scattering of the measured data.

The main conclusion is that careful laboratory testing can inform the mechanisms behind debris flow behaviour observed in the field (high mobility). However, the materials have to be carefully selected in terms of gradation and particles size.

Optical investigation through a flowing saturated granular material

The second part of the doctoral research work, consisted in the development of a novel method for the measurement of micro-behaviour of a transparent highly concentrated particle-fluid system in a ‘free surface’ condition and in the context of relatively high-speed movements of well-graded particle mixtures. Such method allows to overcome the limitations imposed by standard approaches which permit to observe the behaviour of the phenomena under investigation only at the flow margins (usually the top and the sides) since the investigation of the internal behaviour of concentrated two-phase flows is prevented by their high opacity. The two dimensional nature of the sidewall measurements probably reflect only partially the three-dimensional conditions near the sidewall and they cannot exhibit the three-dimensional features of the flow inside the bulk

The employment of particular transparent solids, liquids and fluorescent dyes and the application of the Planar Laser–Induced Fluorescence (PLIF) technique in combination with refractive index matching of the adopted materials makes the direct optical probing of internal points of the medium under investigation possible.

A large part of the PhD research work has been devoted to the design of the experimental apparatus (the flume, the laser and the optical devices), its realization and tuning. Furthermore, the most suitable materials to be used have been selected and the glass particles produced. A number of different tests have been performed for the set-up of the entire procedure. Part of these tests aimed at verifying the suitability of the selected materials to the PLIF technique. Others were performed to understand if the adopted material could mimic some aspects of the flow of natural granular mixtures (i.e. soil and water). Finally a series of preliminary small scale flume tests have been accomplished adopting the implemented methodology. The results proved that the method can be successfully applied to the study of flowing saturated granular materials. The images of the inner part of the flow display good quality and high resolution, making the particles arrangement within the flow and their interactions observable.

The Particle Image Velocimetry (PIV) approach has been used for the quantitative analysis of the flow images. In particular, we used the GeoPIV software to calculate the velocity profiles from the results of some of the available tests. This work is still ongoing in order to improve the data processing procedure finding the most exhaustive solutions to analyze this novel kind of data It is intended that the knowledge gained of the movement of the solids and fluid within the model transparent debris flows and their substrates can be used to validate, improve and calibrate semi-empirical and mechanistic numerical models of debris flows.

Bibliography

Adrian, R.J. 1991. Particle-Imaging Techniques for Experimental Fluid Mechanics, *Annual Review of Fluid Mechanics* 23, 261-304

Arattano, M., Deganutti, A.M., and Marchi, L. 1997. Debris flow monitoring activities in an instrumented watershed on the Italian Alps. Proceedings of the First International ASCE Conference on Debris-Flow Hazard Mitigation: Mechanics, Prediction and Assessment, San Francisco: 506-515.

Arattano, M. 2000. On debris flow front evolution along a torrent*. Physics and Chemistry of the Earth Part B* 25(9): 733–740

Armanini A., Capart H., Fraccarollo, L., & Larcher, M. 2005. Rheological stratification in experimental free-surface flows of granular–liquid mixtures. *Journal of Fluid Mechanics*. 532: 269–319

Bagnold, R. A., 1954. Experiments on a gravity-free dispersion of large solid spheres in a Newtonian fluid under shear. *Proceedings of the Royal Society* , Ser. A 225: 49–63.

Barr, D.W. 2001. Turbulent flow through pourous media. *Ground Water* 39(5): 646-650

Berti M., Genevois R., LaHusen R., Simoni A., Tecca P.R. 2000. Debris flow monitoring in the Acquabona watershed (Dolomites, Italian Alps). *Physics And Chemistry Of The Earth, Part B: Hydrology, Oceans & Atmosphere* 25(9): 707-715

Bowman, E.T., Laue, J., Imre, B., Zweidler, A., and Springman, S.M 2006. Debris flows in a geotechnical centrifuge. *In Proceedings of the 6th International Conference on Physical*

Modelling in Geotechnics. Edited by C.W.W. Ng, L.M. Zhang, and Y.H. Wang. Taylor & Francis, London. 1: 311–316

Bowman, E.T. and Sanvitale, N. 2009 The Role of Particle Size in the Flow Behaviour of Saturated Granular Materials. Alexandria, Egypt: *In Proceedings of the 17th International Conference on Soil Mechanics & Geotechnical Engineering (2009 ICSMGE*)

Bowman, E.T, Laue, J., Imre, B., Springman, S. 2010. Experimental modeling of debris flow behaviour using a geotechnical centrifuge. *Canadian Geotechnical Journal* 47(7): 742-762

Budwig R . (1994). Refractive index matching methods for liquid flow investigations. *Experiments in Fluids* 17: 350–355

Carman, P. C. 1938. The determination of the specific surface of powders. *J. Soc. Chem. Ind. Trans.* 57: 225

Carman, P. C. 1956. Flow of gases through porous media. *Butterworths Scientific Publications*, London.

Carrier, D.W. 2003. Goodbye, Hazen; Hello, Kozeny-Carman. *Journal of Geotechnical and Geoenvironmental engineering* 129(11): 1054-1056

Carrol, M., Edwards, V. & Jackson, P. 2007. Investigating the influence of debris flow parameters when scaling physical models. Final Report, ENNR429 Natural Resources Engineering Project, University of Canterbury, Christchurch

Chapuis R.P, and Aubertin, M. 2003. On the use of the Kozeny-Carman equation to predict the hydraulic conductivity of soils. *Canadian Geotechnical Journal* 40(3): 616-628

Chau, K.T., Chan, L.C.P., Luk, S.T. & Wai, W.H. 2000. Shape of deposition fan and runout distance of debris-flow: Effects of granular and water contents. In Wieczorek & Nasser (eds.) *Debris-flow Hazards Mitigation: Mechanics Pre-diction and Assessment*: 387-395, A.A. Balkema

Chen, C. 1988a. Generalized viscoplastic modeling of debris flow. *Journal of Hydraulic Engineering* 114(3): 237–258

Chen, C. 1988b. General solutions for viscoplastic debris flow. *Journal of Hydraulic Engineering* 114(3): 259–282.

Costa, J. E., & Williams G.P. 1984. Debris-flow dynamics (videotape). *United States Geological Survey. Open File Rep*.:84-606

Coussot, P., Meunier, M. 1996. Recognition, classification and mechanical description of debris flows. *Earth-Science Reviews* 40: 209-227

Coussot, P., and Ancey, C. 1999. Rheophysical classification of concentrated suspensions and granular pastes. *Physical Review* 59 (4): 4445-4457

Cui, M.M., and Adrian, R.J. 1997. Refractive index matching and marking methods for highly concentrated solid-liquid flows. *Experiments in Fluids* 22: 261-264

Darcy, H. 1856. Les fontaines publiques de la ville de Dijon. Vietor Dalmont, Paris

Davies, T.R.H. 1988. Debris-flow surges - A laboratory investigation. *Versuchsanst. fu¨r Wasserbau, Hydrologie und Glaziologie*: 96, 122

Davies, T.R.H.1990. Debris-flow surges - Experimental simulation, *Journal of Hydrology (NZ)* 29: 18–46

Davies, M.C.R., Bowman, E.T., White, D.J. 2010. Physical modeling of natural hazards, In Springman&Seward (eds), *Physical Modelling in Geotechnics*, Taylor & Francis Group

Denlinger, R. P., and R. M. Iverson 2001. Flow of variably fluidized granular masses across three-dimensional terrain: 2. Numerical predictions and experimental tests, *Journal of Geophysical Research* 106: 553–566

Denlinger, R.P., & Iverson, R.M. 2001. Flow of variably fluidized granular masses across three-dimensional terrain, 2. Numerical predictions and experimental tests. *Journal of Geophysical Research* 106(B1): 553–566

Fair, G. M., and Hatch, L. P. 1933. Fundamental factors governing the stream-line flow of water through sand. *Journal of the American Water Works Association* 25: 1551–1565

Fontenot, M.M., and Vigil, R.D. 2002. Pore-Scale Study of Nonaqueous Phase Liquid Dissolution in Porous Media Using Laser-Induced Fluorescence, *Journal of Colloidal and Interface Science* 47(2): 481-489

Harr, H.E. 1962 Ground Water and Seepage, McGraw-Hill, New York, 1962.

Hazen, A. 1892. Some physical properties of sands and gravels, with special reference to their use in filtration. 24th Annual Rep., Massachusetts State Board of Health, Pub. Doc. No. 34: 539–556

Hazen, A. ~1911. Discussion of 'Dams on sand foundations' by A. C. Koenig. *Transactions of the American Society of Civil Engineers* 73: 199–203

Hirano, M., Iwamoto I. 1981. Measurement of debris flow and sediment-laden flow using a conveyor-belt flume in a laboratory. Erosion and Sediment Transport Measurement *Proceedings of the Florence Symposium*, IAHS Publ. no. 133.

Horii, N., Toyosawa, Y., Hashizume, H. 2002. Influence of particle size and structure rigidity on impact stress in simulated debris flow. *Proceedings of the Fifth International Conference on Physical Modelling in Geotechnics:* 399-404

Hotta, N., & Ohta, T. 2000. Pore-Water Pressure of Debris Flows. *Physics and Chemistry of the Earth (B)* 25(4): 381-385

Hsu, L., Dietrich W.E., Sklar, L.S. 2008 Experimental study of bedrock erosion by granular flows. *Journal of Geophysical Research.* 113, F02001

Hungr, O. 1981. Dynamics of Rock Avalanches and other Types of Slope Movements. *Unpublished Phd Thesis* University of Alberta

Hungr, O., and Morgenstern N. R. 1984. High velocity ring shear tests on sand. *Geotechnique*, 34(3): 415–421

Hungr, O., Evans, S.G., Bovis, M.J., Hutchinson, J.N., 2001. A review of the classification of landlides of the flow type. *Environmental & Engineering Geosciences* VII (3): 221-238

Hungr, O. 2005. Classification and terminology. In Jakob, M., & Hungr, O. (eds). *Debris-flow hazards and related phenomena*: 9–23

Hurlimann, M., Rickenmann, D., and Graf, C. 2003. Field and monitoring data of debris-flow events in the Swiss Alps. *Canadian Geotechnical Journal* 40(1): 161–175

Hutter, K., B. Svendsen, & Rickenmann D. 1996. Debris-flow modeling: A review. *Continuum Mechanics and Thermodynamics.* 8: 1–35

Itoh, T., Egashira, S. & Miyamoto, K. 2000. Influence of interparticle friction angle on debris-flows, In *Debris-flow Hazards Mitigation: Mechanics Prediction and Assessment*, Wieczorek and Nasser editors: 219-228

Iverson, R.M., and Denlinger R.P. 1987. The physics of debris flows - A conceptual assessment. *In Erosion and Sedimentation in the Pacific Rim*, edited by R. L. Beschta et al., IAHS Publ., 165: 155–165

Iverson, R.M. 1997. The Physics of Debris Flows. *Reviews of Geophysics* 35(3): 245-296

Iverson, R. M., & Denlinger R.P. 2001. Flow of variably fluidized granular masses across three-dimensional terrain: 1. Coulomb mixture theory*, Journal of Geophysical Research* 106: 537–552

Iverson, R.M., 2005, Debris-flow mechanics, in *Debris Flow Hazards and Related Phenomena*, M. Jakob and O. Hungr, eds, Springer-Praxis: 105-134

Iverson, R.M., Logan, M., LaHusen, R.G., Berti, M. 2010. The perfect debris flow? Aggregated results from 28 large-scale experiments. *Journal of Geophysical Research* 115

Jakob M. & Hungr O. 2005, *Debris-flow hazards and related phenomena*, Springer and Praxis editorials

Jan, C.-D. and Shen, H. 1997. Review Dynamic Modeling of Debris Flows, In *Recent developments on debris flows* edited by Armanini, A. and Michiue, M., Springer: 93–113

Johnson, A. M. 1965. A model for debris flow. Ph.D. dissertation, Pa. State Univ., State College.

Johnson, A. M. 1970. Physical Processes in Geology, 1970, 557, W. H. Freeman, New York.

Johnson, A. M. 1984. Debris flow. In *Slope Instability*. Edited by D. Brunsden and D. B. Prior, 257–361, John Wiley, New York.

Julien, P.Y. & lan, Y. 1991. Rheology of hyperconcentrations. *Journal of Hydraulic Engineering* 117(3): 346-353

Julien, P. Y. & O'Brien, J. S. 1997. On the importance of mud and debris flow rheology in structural design. *In Debris-Flow Hazards Mitigation: Mechanics, prediction, and Assessment*. Edited by:Chen, C.-l., ASCE, New York, N.Y., 350–359..

Kaitna, R, Rickenmann, D, Schneiderbauer, S. 2006. Comparative rheologic investigations in a vertically rotating flume and a 'moving bed' conveyor belt flume. In: Lorenzini G, Brebbia CA, Emmanouloudis DE (eds) Monitoring, simulation, prevention and remediation of dense and debris flows. WitPress, Southampton, pp 89–98

Kaitna, R. & Rickenmann D. 2005. Debris flow experiments in a vertically rotating drum. *General Assembly of the European Geosciences Union,* Wien: 24-29

Kozeny, J., 1927. Ueber kapillare Leitung des Wassers im Boden, Wien, Akad. Wiss.,136~2a, 271

Larcher A., Fraccarollo L., Armanini A., Capart H., 2007. Set of measurement data from flume experiments on steady uniform debris flows. *Journal of Hydraulic Research* 45: 59–71.

Logan, M., Iverson R.M. 2007 Video documentation of experiments at the USGS debris flow flume. 1992-2006, U.S. Geological Survey Open-file Report 2007-1315

Loudon, A. G. 1952. The computation of permeability from simple soil tests. *Geotechnique* 3(4): 165–183

Mainali, A., Rajaratnam, N. 1994. Experimental study of debris flows. *Journal of Hydraulic Engineering* 120(1): 104-123

Mahoney, D.P. 2006. The effects of moisture content and relative density on granular debris flow behaviour: and experimental investigation. Project Report, University of Canterbury, Christchurch

Major, J.J., Iverson, R. M., McTigue, D.F., Macias, S., and Fiedorowicz, B.K., 1997. Geotechnical properties of debris-flow sediments and slurries. in *Chen, C. L., ed., Debris flow hazards mitigation: Mechanics, prediction, and assessment: American Society of Civil Engineers, Proceedings of First International Conference, August 7–9, San Francisco:* 249–259

Major, J.J. &. Iverson, R.M 1999. Debris-flow deposition - effects of pore-fluid pressure and friction concentrated at flow margins. *Geological Society of America Bulletin* 111: 1424-1434

Myles, F., and Parkin, E., 2009. Debris Flows in the New Zealand Context, Final Report, ENNR429 Natural Resources Engineering Project, University of Canterbury, Christchurch

McArdell, B.W., Bartelt, P., and Kowalski, J. 2007. Field observations of basal forces and fluid pore pressures in a debris flow. *Geophysical Research Letters* 34

Hassanizadeh, S. M. & Gray, W.G. 1990 Mechanics and thermodynamics of multiphase flow in porous media including interface boundaries. *Advances in Water Resources*. 13 (4): 169-186

Neddermann, R.M. 1992. Statics and Kinematics of granular materials, Cambridge University Press

Pierson, T.C. 1980. Erosion and deposition by debris flows at Mt. Thomas, North Canterbury, New Zealand, *Earth Surface Processes*, 5: 227–247

Okuda, S., Suwa H., Okunishi K., Yokoyama K. & Nakano M., 1980. Observations on the motion of a debris flow and its geomorphological effects. *Z. Geomorphol., suppl.* 35: 142–163

Okuda, S., Suwa, H., Okunishi, K., and Yokoyama, K., 1981. Depositional processes of debris flow at Kamikamihori fan, Northern Japan Alps. *Japanese Geomorphological Union, Transactions* 2: 353–361

Okuda, S.,and Suwa, H., 1984. Some relationships between debris flow motion and microtopography for the Kamikamihori fan, North Japan Alps. In "Catchment Experiments in Fluvial Geomorphology". Burt & Walling (eds) GeoBooks, Norwich: 447-464

Orpe V.O., and Kudrolli, A., 2007, Velocity Correlations in Dense Granular Flows Observed with Internal Imaging. *Physical Review Letters*, 98(23): 238001

Pierson, T.C. 1980. Erosion and deposition by debris flows at Mt. Thomas, North Canterbury, New Zealand. *Earth Surface Processes* 5: 227–247

Pierson, T.C. 1986. Flow behavior of channelized debris flows, Mount St. Helens, Washington. in Hillslope Processes, edited by A. D. Abrahams: 269–296

Pitman, E.B. & Le, L. 2003. A two fluid model for avalanche and debris flows. *Philosophical Transactions of the Royal Society*, *Series A*, 363: 1573-1601

Powrie, W., 2004. Soil Mechanics – concepts &applications, Taylor & Francis

Pudasaini S.P., Wang Y. & Hutter K. 2005. Rapid motions of free-surface avalanches down curved and twisted channels and their numerical simulation. *Philosophical Transactions of the Royal Society*, *Series A* 363: 1551-1571

Reynolds, O., 1883. An experimental investigation of the circumstances which determine whether the motion of water shall be direct or sinuous, and of the law of resistance in parallel channels. *Philosophical Transactions of the Royal Society* 174: 935–982

Roesli, U., Schindler, C. 1990. Debris flows 1987 in Switzerland: geological and hydrogeological aspects. Hydrology in Mountainous Regions. II - Artificial Reservoirs; Water and Slopes, *Proceedings of two Lausanne Symposia,* IAHS Publ., 194

Rombi, J., Pooley, E.J. & Bowman, E.T. 2006. Factors influencing granular debris flow behaviour: an experimental investigation. In Ng, C.W.W., Zhang, L.M. & Wang, Y.H. (eds). *6th International Conference on Physical Modelling in Geotechnics*: 379–384.

Savage, S. B., and Hutter K. 1989. The motion of a finite mass of granular material down a rough incline. *Journal of fluid mechanics 199*: 177–215

Schatzmann M. 2005 Rheometry for large particle fluids and debris flows. Ph.D. Thesis, University of Zurich.

Scheidegger, A. 1957. The Physics of Flow Through Porous Media. University of Toronto Press and Oxford University Press, London Great Britain

Skermer, N.A. & VanDine, D.F. 2005. Debris flows in history. In *Debris-flow hazards and related phenomena*: 25-51. Chichester: Praxis

Stolz, A., and Huggel, C. ,2008. Debris flows in the Swiss National Park: The influence of different flow models and varying DEM grid size on modeling results. *Landslides* 5: 311-319

Stohr M., Roth M., Jahne K. 2003. Measurement of 3D pore-scale flow in index-matched porous media. *Experiments in Fluids* 35: 159–166

Suwa, H., 1989. Field observation of debris flow. *Proceedings of Japan-China (Taipei) Joint Seminar on Natural Hazard Mitigation*, Kyoto: 343–352.

Tajalli, H., Gilani, A., Zakerhamidi, M.S., Taralli, P. 2008. The photophysical properties of Nile red and Nile blue in ordered anisotropic media. *Dyes and Pigments* 78: 15-24

Takahashi, T. 1978. Mechanical characteristics of debris flow. *Journal of the Hydraulics Division* 104: 1153–1169

Takahashi, T., Yoshida, 1979. Study on the deposition of debris flow. Annual Report Disaster Prevention Research Incstitute, Kyoto, 22-B-2, 315-328

Takahashi, T. 1980. Debris flows on prismatic open channel. *Journal of the Hydraulics Division* 186: 381-395

Takahashi, T. 1981. Debris flow. *Annual* Review of *Fluid Mechanics* 13: 57–77

Takahashi, T. 1991. Debris Flow. A. A. Balkema, Brookfield, Vt.

Takahashi T. 2001a. Mechanics and simulation of snow avalanches, pyroclastic flows and debris flows. *Special Publications of International Association of Sedimentology* 31: 11–43

Takahashi, T. 2007. Debris Flow: Mechanics, Prediction and Countermeasures. Taylor and Francis.

Taylor, D.W., 1948. Fundamentals of Soil Mechanics, John Wiley & Sons, Inc., New York

Tsai, J-C., and Gollub, J.P., 2004. Slowly sheared dense granular flows: Crystallization and nonunique final states. *Physical Review Letters E* 70, 031303

Vallejo, L. E.,1995. Fractal analysis of granular materials. *Geotechnique* 45(1): 159-163

Vanoni, V. A., 1975, Sedimentation Engineering. Manual 54, American Society of Civil Engineers, New York, 745 pp.

Whipple, K.X., Mohrig, D., Parker, G., Hondzo, M., and Ellis, C., 1995. Experimental study of subaqueous debris flows. *Geological Society America, Abs. with Prog*. 27(6): 127-128

Whipple K.X. 1997. Open-Channel Flow of Bingham Fluids: Applications in Debris-Flow Research, *The Journal of Geology* 105: 243–262

White, D.J., Take, W.A. & Bolton, M.D. 2003. Soil deformation measurement using particle image velocimetry (PIV) and photogrammetry. *Géotechnique* 53(7): 619–631

White D.J. & Take W.A. 2002. GeoPIV: Particle Image Velocimetry (PIV) software for use in geotechnical testing. *Cambridge University Engineering Department Technical Report*, D-SOILS-TR322

Yano, K. & Daido A. 1965. Fundamental study on mud-flow. Bull. Disaster Prev. Res. Inst. Kyoto Univ. 14: 69–83